Adaptive Flutter Test Vane: Low Net Passive Stiffness (LNPS) Techniques for Deflection Amplification of Piezoelectric Actuators

By
Ryan Barnhart

Submitted to the graduate degree program in Aerospace Engineering and the Graduate Faculty of the University of Kansas in partial fulfillment of the requirements for the degree of Master of Science.

_____
Dr. Ronald Barrett-Gonzalez, Committee Chairman

_____
Dr. Mark Ewing, Committee Member

_____
Dr. Shahriar Keshmiri, Committee Member

Date Defended: August 24, 2012

The Thesis Committee for Ryan Barnhart
certifies that this is the approved version of the following thesis:

Adaptive Flutter Test Vane: Low Net Passive Stiffness (LNPS) Techniques for Deflection Amplification of Piezoelectric Actuators

_____

Chairperson Dr. Ronald Barrett-Gonzalez

Date approved: August 24, 2012

Abstract

This document outlines the design, development and testing of an adaptive flutter test surface utilizing low net passive stiffness (LNPS) actuator configurations for deflection amplification. The device uses a tapered piezoelectric bender actuator in an aerodynamic shell which pivots about the quarter-chord. Laminated plate theory is used to capture the unamplified deflection levels. A unique reverse-bias spring mechanism enables LNPS techniques, generating a 5:1 amplification ratio from baseline deflection levels with negligible weight penalty and no degradation in blocked moments. The adaptive flutter test vane and associated spar-mounting hardware have a combined weight of only 2 lb and consume less than 1W of peak power at maximum actuation voltage. The significance of the relatively low installed weight is apparent when considering the effect on the modal mass of the aircraft. It can be shown that a reduction in weight from the current state-of-the-art 18+ lb (installed) DEI vane to a 2 lb adaptive flutter test vane (installed) improves the normalized first natural frequency of flap in a wing from approximately 60% to 90% in light aircraft classes - all but eliminating the detrimental effect of additional mass on the accuracy of flutter prediction. Quasi-static and dynamic wind tunnel testing shows excellent correlation with bench tests and theory. Maximum deflection levels were recorded in excess of 8 deg. peak-to-peak, with a corner frequency in excess of 50 Hz. Wind tunnel tests were performed up to 110 ft/s with change in lift forces on the order of 1.45 lb_f. This paper focuses on the testing and evaluation of the aforementioned hardware for applications in certification of small aircraft in the general aviation (GA), light sport (LSA), homebuilt and ultralight classes.

This work is dedicated to my family for their endless support, to my friends for their endless understanding, and to my Mother – for her sprit that still lies within me.

The author would also like to thank his advisor, Dr. Ron Barrett, for his tremendous dedication and guidance throughout the duration of this investigation.

Table of Contents

Table of Contents (Cont'd)

Page #

List of Figures

Page #

List of Figures (Cont'd)

Page #

List of Tables

Page #

List of Symbols

Symbol	Description	Units
a	2D Lift Curve Slope	1/rad
A	Amplitude of Forcing Function	--
A	Aspect Ratio	--
A_{ij}	Extensional Stiffness	lb_f/in
b	Span	ft or in
B_{ij}	Extensional Stiffness	lb_f
c	Chord	ft
c	Damping Coefficient	ft-lb_f/(rad/s)
C	Tunnel Test Section Area	in^2
C_D	Drag Coefficient	--
C_L	Lift Coefficient	--
$C_{L,\alpha}$	3D Lift Curve Slope	1/deg
C_l	2D Lift Coefficient	--
C_{lp}	Rolling Moment Coefficient Due to Roll Rate	1/rad
C_{Mq}	Pitching Moment Coefficient Due to Pitch Rate	1/rad
D	Distance	in
D_{ij}	Extensional Stiffness	lb_f-in
E	Modulus of Elasticity	lb_f/in^2
f	Frequency	Hz
f_0	Mass Normalized Force (Magnitude)	lb_f/lb_m
f_c	Corner Frequency	Hz
f_n	Natural Frequency	Hz
F	Force	lb_f
G	Shear Modulus	lb_f/in^2
h	Height	in
I_o	Rotational Mass Moment of Inertia	ft^2-lb_m
I_Θ	Rotational Mass Moment of Inertia	ft^2-lb_m
k	Reduced Frequency	--
k	Stiffness	lb_f/in
k_w	Correction Constant for Wing Contribution to Pitch Damping	--
k_δ	Rotational Stiffness	in-lb_f/rad
k_Θ	Rotational Stiffness	in-lb_f/rad
K_1	Body Shape Factor	--
L	Length	in
L	Lift	lb_f
L	Load	N
L_P	Aerodynamic Damping	ft-lb_f/(rad/s)
m	Mass	lb_m
M	Moment	lb_f-in
N	Length	in
Q	Reduced Stiffness	lb_f/in^2
$\bar{Q}$	Transformed Reduced Stiffness	lb_f/in^2
r	Frequency Ratio	--
S	Area	in^2
t	Thickness	in

List of Symbols (Cont'd)

Symbol	Description	Units
t	Time	s
V	Velocity	ft/s
V	Voltage	volts
V	Volume	in^3
X	Magnitude of the Response	deg
Y_{cgw}	Y-Location Center of Gravity of the Wing	in

Greek Symbols

α	Angle of Attack	1/deg
α	Coefficient of Thermal Expansion	1/°C
γ	Shear Stress	l lb_f/in^2
Γ	Normalized Deflection	$1/(ft\text{-}lb_f)$
δ	Angular Deflection	deg
δ	Boundary Correction Factor	--
δ	Logarithmic Decrement	--
Δ	Change in	--
ε	Strain	in/in
ε	Velocity Correction Factor	--
ζ	Damping Ratio	--
θ	Angle of Rotation	deg
κ	Curvature	deg/in
Λ	Virgin Strain	--
ν	Poisson's Ratio	--
ρ	Density	$slugs/ft^3$
σ	Stress	lb_f/in^2
τ	Shear Stress	lb_f/in^2
τ_1	Tunnel Test Section Shape Factor	--
τ_2	Streamline Curvature Factor	--
φ	Body Rotation Angle	rad or deg
ω	Angular Frequency	rad/s or Hz
ω_c	Corner Frequency	rad/s or Hz
ω_n	First Natural Frequency	rad/s or Hz

Subscripts

ΔT	Change Due to Thermal Expansion	--
1	Principal Axis in 1-Direction	--
2	Principal Axis in 2-Direction	--
3	Principal Axis in 3-Direction	--
6	Direction of Shear	--
a	Actuator	--
A	Aerodynamic	--
actuation	Due to Actuation	--
aero	Aerodynamic	--
b	Body	--
b	Bond	--

List of Symbols (Cont'd)

Symbol	Description	Units
Subscripts (Cont'd)		
e	Effective	--
exp	Experimental	--
f	Fuselage	--
L	Laminate	--
lower	Lower	--
max	Maximum	--
mw	Wing-Mass	--
net	Net	--
p	Pivot	--
pzt	Of the Actuator	--
rod	Of the Rod	--
s	Spring	--
s	Structural	--
s	Substrate	--
s_L	Spring (Loaded)	--
s_{UL}	Spring (Unloaded)	--
sc	Streamline Curvature	--
sp	Spring	--
swb	Solid Blocking	--
test	Testing	--
tot	Total	--
u	Uncorrected	--
UL	Unloaded	--
upper	Upper	--
v	Vertical	--
vane	Vane	--
w	Wing	--
wb	Wake Blocking	--
wing	Wing Section	--
∞	Free-Stream	--
Acronyms		
AoA	Angle of Attack	1/deg
CF	Correction Factor	lb_f/N
CLPT	Classical Laminated Plate Theory	--
CR	Compression Ratio	--
CV	Command Voltage	volts
DEAS	Dynamic Elastic Axis Shifting	--
DEI	Dynamic Engineering Incorporated	--
EP	End Plate	in
FAR	Federal Aviation Regulation	--
FBR	Free Body Rotation	--
LNPS	Low Net Passive Stiffness	--

List of Symbols (Cont'd)

Symbol	Description	Units
Acronyms (Cont'd)		
LSA	Light Sport Aircraft	--
LWU	Left Wing Up	--
MAV	Micro Aerial Vehicle	--
NBR	No Body Rotation	--
P2P	Peak-to-Peak	--
PBP	Post-Buckled Precompressed	--
PZT	Lead-Zirconate-Titanate	--
RN	Reynolds Number	--
RWU	Right Wing Up	--
TF	Turbulence Factor	--
UAV	Unmanned Aerial Vehicle	--
ZNPS	Zero Net Passive Stiffness	--

1 Introduction

Recent regulatory changes governing the fabrication, training of fabricators, inspection and use of small aircraft has lead to new classes and types of airplanes. Many of these airframes, including Light Sport Aircraft (LSA's) employ structural artifacts, configurations and design techniques that are not compatible with traditional Federal Aviation Regulations - specifically FAR-23 regulations. Although they clearly save in manufacturing costs, an extremely high accident rate has brought them under scrutiny. Because many of these techniques can induce structures to change their dynamic behavior with increased flight hours, many accident investigators and professional aircraft designers suspect that various forms of structural instabilities including flutter are the root of the some of the accidents.[1] Flutter occurs in flight when the second-bending and first-torsion modes of a lifting surface coalesce, causing a dynamic instability both visible and measurable through amplified and unstable deflection profiles. This instability can often lead to catastrophic structural failure including but not limited to buckling and separation from the airframe. Once excited, flutter is often difficult to damp out and creates an extremely dangerous scenario for the pilots, passengers and community on the ground. Flutter most commonly occurs due to excessive flight velocity, atmospheric turbulence and/or maneuvers not recommended for the airframe. If the flutter characteristics of an airframe are not well-defined, this phenomenon can occur rapidly and unexpectedly.

The purpose of this investigation is to identify, develop, characterize and evaluate a novel device capable of reliably exciting flutter in small aircraft in the interest of reducing the accident rate and providing safer travel through improved flutter test certification. The constituents of the device outlined in this document can be classified into three focus areas: flight flutter testing,

piezoelectric actuators and low net passive stiffness (LNPS) configurations for deflection amplification. The use of composite materials adds to the simplicity of the design while allowing for a lightweight and structurally efficient mechanism for exciting flutter in small aircraft classes. Each constituent will be introduced in this chapter along with its significance to the success of this project.

1.1 Flight Flutter Testing[1]

Since flutter parameter prediction is extremely difficult for small aircraft, flight testing becomes increasingly important to the development of the operational envelope of a given airframe. Problems with flight testing these aircraft, however, arise during implementation of excitation mechanisms. Often testing procedures utilize atmospheric turbulence to target structural modes. Unfortunately, it is difficult to excite all of the modes of interest using only atmospheric turbulence.[2] Atmospheric turbulence is also, by definition, unpredictable in nature. Attempting to harness the power of atmospheric turbulence through precise control surface deflection and timing provides the capability for exciting flutter, albeit with little precision.[2] Another option is to use ground-based modal parameter extraction. This method, however, does not always accurately simulate in-flight loads.[3] Ground-based modal testing does not accurately simulate the boundary conditions on the airframe, particularly with respect to body z-axis translations. The body z-axis is defined by Figure 1.1. If the landing gear is in contact with another surface, the airframe is affected by the forces being applied in the direction of the body z-axis, creating the potential for premature onset of flutter. The effects of aerodynamic damping are also not accounted for using this method, eliminating a potential source for delaying the onset of flutter.

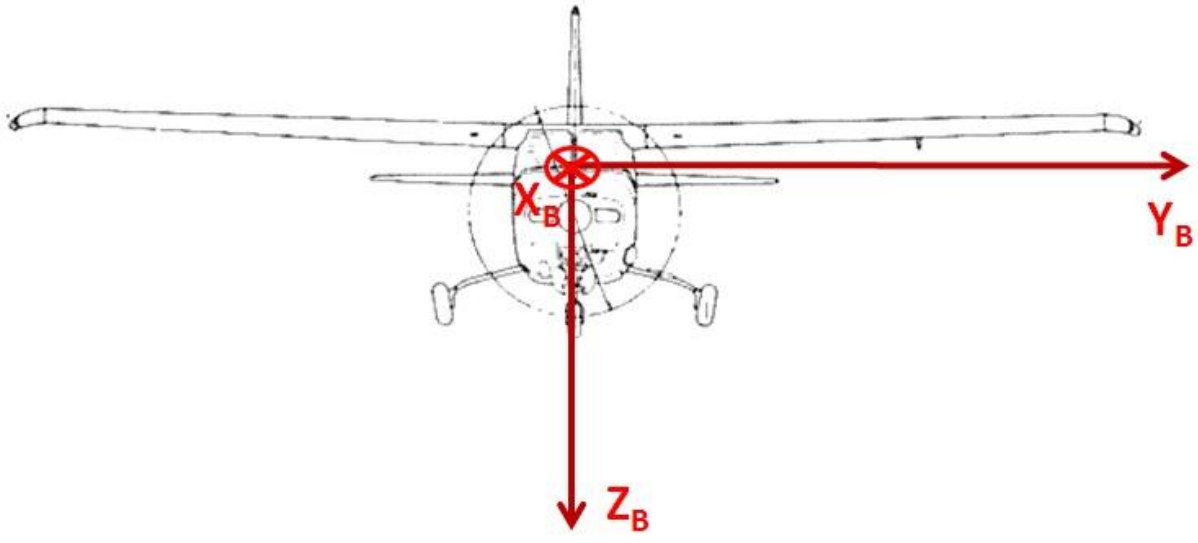

Figure 1.1 - Aircraft Body Coordinate System

Other methods of exciting flutter during flight testing include using explosive devices as excitation mechanisms. Explosive devices generate an impulse force on the lifting surface, potentially exciting one or both of the vibrational modes required for flutter. These are one-time use options which consequently prevent multiple tests in a single flight. Cost, time and complexity of using explosive devices (bonkers) often make them undesirable in many applications.[4]

It should be clear that because of the unreliability of the aforementioned methods it is advantageous to implement a tip-mounted adaptive excitation device that manipulates natural atmospheric loads to target structural vibration modes. Devices like this have been tested and shown to have extremely reliable results on aircraft such as the F-16XL.[4] This device uses a rotating slotted drum mounted to an aerodynamic surface to generate random vibrations at the tip of a lifting surface in attempt to excite flutter. There are, however, several significant

disadvantages of a device like this, including high weight, high power consumption, which results in high electrical line weight, and the inability to control the phase of force application with respect to other excitation vanes on the aircraft. A tip mounted device can change the natural frequencies of the wing/tail tremendously due to a change in mass and mass distribution. In the case of the flight tests performed by NASA Dryden Flight Research Facility on the F-16XL, the 10 lb excitation mechanism developed by Dynamic Engineering, Incorporated (DEI) was considered to be a negligible change in mass distribution of the wing.[4] It should be noted that this device can weigh up to 18 lb installed due to the enormous power requirement, hydraulic motor and associated wiring harnesses. This weight penalty might not be considered negligible in smaller, lighter classes such as LSAs, homebuilt aircraft, ultralights, UAVs, or gliders. The success of the DEI vane shown in Figure 1.2 sparked further research into making lighter, faster and more reliable flutter test vanes for use in the certification of new small aircraft.

Figure 1.2 - DEI Flutter Vane - Rotating Cylinder[5]

The aforementioned difficulties in flight flutter testing and the necessity for significant changes in methodology in the aerospace industry is the motivation for this investigation. It is clear that

extremely reliable means for determining the flutter characteristics of *all* aircraft is extraordinarily important to the safety of pilots, passengers, people and property. It is the opinion of this author that the most effective method for determining flutter characteristics is through extensive flight testing. While the methods of flutter excitation are arguable, there exists almost no substitute for the boundary conditions of free flight. It has been shown that flutter vanes are an effective means of flutter excitation for aircraft with wing semi-span weights that exceed those of the general aviation class.[4] These devices, however, are of little use to the in-flight flutter prediction of lightweight airframes due to the detrimental impact on the modal mass of the wing or tail to which they are mounted. These devices also lack the capability for full force and phase control, limiting the quantity of tests to those measurable using random vibrations, as well as the limiting the quality of those tests. It will be shown in Chapter 4 that the ability to control both force and phase is an invaluable benefit provided by the flutter test vane developed for this investigation.

1.2 Piezoelectric Actuators

The piezoelectric effect was discovered by Pierre Curie and his brother Jacques in the 1880s in Rochelle salt. This effect is present in other natural resources such as quartz crystals and diamonds. The Curie brothers discovered that, through the application of pressure to quartz crystals, an electric potential could be observed. The converse, however, was not observed until several years later. This discovery led to over 100 years of development of mechanisms taking advantage of piezoelectricity by the scientific and engineering communities. These technologies included force transducers, strain measurement devices, high speed electrical switches and countless other devices. Among these developments was also a hoard of actuation devices used

for the application of force, as well as translation and rotation. Chapter 2 outlines the application of piezoelectric actuators as it pertains to this investigation.

1.3 LNPS Configurations

The underlying theory behind LNPS structures is not a new one. It is well known that applying a force along the longitudinal axis of a beam is destabilizing, and can lead to dramatic changes in deformation magnitude between equilibrium states. This concept was introduced to the field of adaptive structures first by George Lesieutre et al in an attempt to force the apparent coupling coefficient of piezoelectric actuators to 1.[7,8] The technology was later adapted into a plethora of post-buckled precompressed piezoelectric devices, primarily for use in flight control actuators of micro-aerial vehicles (MAVs).[9-12] The theory behind LNPS structures as developed for applications in flight flutter testing is presented in Chapter 3.

2 Fundamental Piezoelectric Theory

Piezoelectric actuators operate in two ways – electrically-induced elemental strain or generation of electrical power from a change in pressure on the element. Application of extremely high electrical fields to piezoelectric sheets aligns the dipoles, resulting in in-plane strain which causes the element to contract or expand. This contraction/expansion can be used in unimorphs (symmetrically poled actuators) for translation or bimorphs (asymmetrically poled actuators) for bending. In this investigation the latter was incorporated into an aerodynamic flutter vane, allowing for rotation about the quarter-chord of the structure. The internal structure of the adaptive flutter test vane is discussed in more detail in Section 3.3.

2.1 Bimorph Actuators

Bimorph actuators have uses as actuation mechanisms where rotation is required. This is achieved by constructing a laminate consisting of two piezoelectric sheets bonded to a substrate at its neutral axis as shown in Figure 2.1. These sheets are arranged such that the direction of the dipoles in one sheet is in opposition to the dipoles of the other sheet (asymmetric poling). When one piezoelectric sheet expands, the sheet on the other side of the substrate contracts. This creates a bending moment about the neutral axis and the actuator deforms according to its constraints at the mounting points. This deformation can be symmetric bending, torsion, or both, depending on the constraint. Applications of this configuration are numerous, and only one scenario as it applies to this investigation will be presented. A bimorph was constructed and evaluated as discussed in Section 2.3.

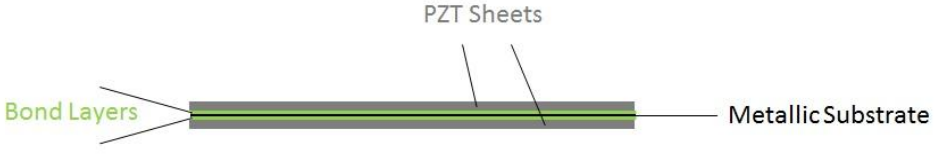

Figure 2.1 - Piezoelectric Bimorph

2.2 Mechanically and Thermally Induced Precompression

Precompression of piezoelectric actuators reduces the presence of tensile strain on the fragile piezoelectric sheets preventing premature fracture. Precompression is most often incorporated in one of two ways – mechanically or thermally – as outlined below.

Piezoelectric actuators are often constructed using piezoelectric sheets and metallic substrates bonded together in a laminate using a matrix material in between (Figure 2.1). As the laminate is assembled, the metallic substrate can be put in tension by an external axial force. Once the matrix has cured and the force is removed the substrate naturally attempts to return to its unstrained state. As the substrate relaxes, the piezoelectric sheets are compressed by means of shear transfer through the bond layers. Thermally induced precompression is achieved in a similar manner. During an elevated temperature cure cycle, the mismatch of coefficient of thermal expansion can be manipulated such that the metallic substrate expands more than the piezoelectric sheet. When the matrix is cured and the temperature is reduced the substrate compresses the piezoelectric elements. Both methods must be carefully performed as buckling within the laminate may occur. This is not necessarily an undesirable effect, as is shown by the results of investigations into post-buckled precompressed piezoelectric actuators.[9-15] Care must also be taken to avoid snap-through events that can be damaging both to the structural integrity of the laminate and its performance.[16-20] These issues are discussed as they apply to this investigation throughout this document.

2.3 Vane Actuator Theory

Of vital importance to this investigation is the design of the piezoelectric actuator itself. 10 mil (0.010") thick lead-zirconate-titanate (PZT) 5H elements were bonded to a tapered 5 mil stainless steel substrate as shown in Figure 2.2. The bond layers were also tapered to provide greater stiffness at the root of the actuator. This prevents possible fracture due to large bending moments at the root. Using Classical Laminated Plate Theory (CLPT) the in-plane curvature of the actuator, κ_{11}, can be determined. It should also be noted that this actuator design has an inherent level of thermally induced precompression due to the elevated temperature cure cycle. This level of thermally induced precompression is included in determining the baseline (free) angular deflection of the adaptive flutter test vane. The resulting analytical model can then be compared to experimental results of bench testing (Section 5.4).

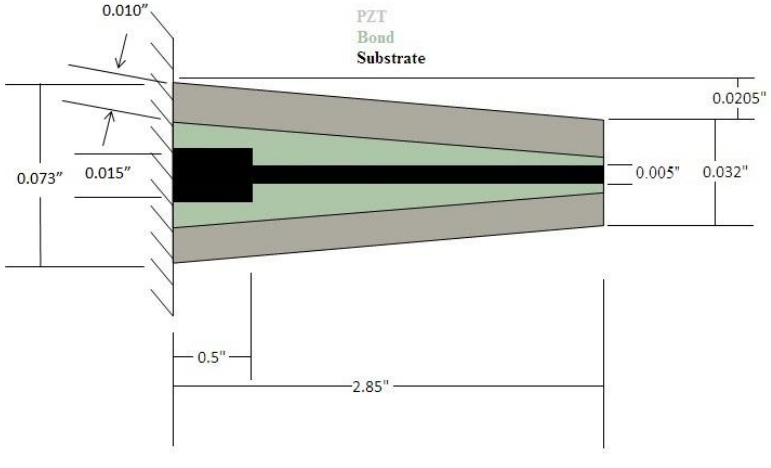

Figure 2.2 - Vane Actuator Design (Not to Scale)

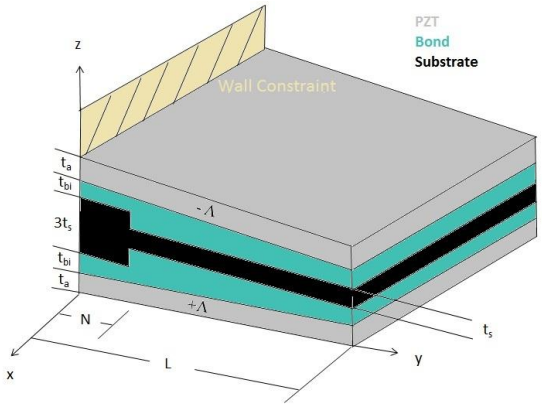

Figure 2.3 - Actuator Coordinate System Definition

The coordinate system is defined with origin at the root of the actuator, the x-axis along the span of the actuator (positive out of the page), y-axis positive root to tip, and z-axis positive up according to the right hand rule as shown in Figure 2.3, the derivation of the curvature of the laminate, κ_{11}, can be expressed by classical lamination theory according to Jones.[21]

$$[\sigma]_L \equiv [Q]_L\{\varepsilon\}_L \rightarrow \begin{bmatrix}\sigma_x\\ \sigma_y\\ \tau_{xy}\end{bmatrix} \equiv \begin{bmatrix}Q_{11} & Q_{12} & Q_{16}\\ Q_{12} & Q_{22} & Q_{26}\\ Q_{16} & Q_{26} & Q_{66}\end{bmatrix}\begin{bmatrix}\varepsilon_x\\ \varepsilon_y\\ \gamma_{xy}\end{bmatrix} \tag{1}$$

Where the subscript L indicates "laminate", and σ and ε are the stress and strain matrices, respectively, and $[Q]$ refers to the reduced stiffness matrix as defined by:

$$Q_{11} \equiv \frac{E_1}{1-\nu_{12}\nu_{21}}\ ;\ Q_{22} \equiv \frac{E_2}{1-\nu_{12}\nu_{21}};\ Q_{12} \equiv \frac{\nu_{12}E_2}{1-\nu_{12}\nu_{21}} = \frac{\nu_{21}E_1}{1-\nu_{12}\nu_{21}}\ ;\ Q_{66} \equiv\ G_{12} \tag{2}$$

Equation (1) is then transformed into the laminate coordinate system using:

$$\bar{Q}_{11} = Q_{11}cos^4(\theta) + 2(Q_{12} + 2Q_{66})sin^2(\theta)cos^2(\theta) + Q_{22}sin^4(\theta) \quad (3)$$

$$\bar{Q}_{12} = (Q_{11} + Q_{22} - 4Q_{66})sin^2(\theta)cos^2(\theta) + Q_{12}[sin^4(\theta) + cos^4(\theta)] \quad (4)$$

$$\bar{Q}_{22} = Q_{11}sin^4(\theta) + 2(Q_{12} + 2Q_{66})sin^2(\theta)cos^2(\theta) + Q_{22}cos^4(\theta) \quad (5)$$

$$\bar{Q}_{16} = (Q_{11} - Q_{12} - 2Q_{66})sin(\theta)cos^3(\theta) + (Q_{12} - Q_{22} + 2Q_{66})sin^3(\theta)\cos(\theta) \quad (6)$$

$$\bar{Q}_{26} = (Q_{11} - Q_{12} - 2Q_{66})sin^3(\theta)cos(\theta) + (Q_{12} - Q_{22} + 2Q_{66})\sin(\theta)cos^3(\theta) \quad (7)$$

$$\bar{Q}_{66} = (Q_{11} + Q_{22} - 2Q_{12} - 2Q_{66})sin^2(\theta)cos^2(\theta) + Q_{66}\sin^4(\theta)cos^4(\theta) \quad (8)$$

Note that for a symmetric laminate, $\bar{Q}_{16} = \bar{Q}_{26} = 0$. Another relationship is established by introducing the actuator virgin strain, Λ:

$$[\bar{Q}]_L\{\varepsilon\}_L = [\bar{Q}]_{a1}\{\Lambda\}_{a1} + [\bar{Q}]_{a2}\{\Lambda\}_{a2} \quad (9)$$

Where the subscripts a1 and a2 identify top and bottom PZT sheets, respectively.

Let E_a represent the modulus of the PZT, E_s the modulus of the substrate and ν_a the Poisson's ratio for the PZT. It should be noted that piezoelectric ceramics are isotropic in an unpolarized state but become anisotropic once poled. This anisotropy is considered negligible and will be ignored for the following derivation such that:

$$[E_1]_a = [E_2]_a = [E]_a \; ; \; \nu_{12} = \nu_{21} = \nu_a \quad (10)$$

The steel substrate is isotropic in nature, leaving only three moduli to track within the laminate: E_a, E_s and E_b - the modulus of the bond layer. The stresses can be redefined in terms of force, F, and moment, M by noting that:

$$F = \int_{-t/2}^{t/2} \sigma \, dz \tag{11}$$

$$M = \int_{-t/2}^{t/2} \sigma \, z dz \tag{12}$$

Where the z-axis is defined through the thickness of the laminate as shown in Figure 2.3. To equate these forces to the strains of Equation (1) the laminate curvature, κ, must also be incorporated. The result is an expanded form of Equation (1) using the extensional stiffness terms, A_{ij}, B_{ij}, and D_{ij}:

$$\begin{bmatrix} F_x \\ F_y \\ F_{xy} \end{bmatrix} = \begin{bmatrix} A_{11} & A_{12} & A_{16} \\ A_{12} & A_{22} & A_{26} \\ A_{16} & A_{26} & A_{66} \end{bmatrix} \begin{Bmatrix} \varepsilon_x \\ \varepsilon_y \\ \tau_{xy} \end{Bmatrix} + \begin{bmatrix} B_{11} & B_{12} & B_{16} \\ B_{12} & B_{22} & B_{26} \\ B_{16} & B_{26} & B_{66} \end{bmatrix} \begin{Bmatrix} \kappa_x \\ \kappa_y \\ \kappa_{xy} \end{Bmatrix} \tag{13}$$

$$\begin{bmatrix} M_x \\ M_y \\ M_{xy} \end{bmatrix} = \begin{bmatrix} B_{11} & B_{12} & B_{16} \\ B_{12} & B_{22} & B_{26} \\ B_{16} & B_{26} & B_{66} \end{bmatrix} \begin{Bmatrix} \varepsilon_x \\ \varepsilon_y \\ \tau_{xy} \end{Bmatrix} + \begin{bmatrix} D_{11} & D_{12} & D_{16} \\ D_{12} & D_{22} & D_{26} \\ D_{16} & D_{26} & D_{66} \end{bmatrix} \begin{Bmatrix} \kappa_x \\ \kappa_y \\ \kappa_{xy} \end{Bmatrix} \tag{14}$$

The extensional stiffness terms are defined by:

$$A_{ij} \equiv \sum_{k=1}^{N} \left(\bar{Q}_{ij}\right)_k (z_k - z_{k-1}) \tag{15}$$

$$B_{ij} \equiv \frac{1}{2}\sum_{k=1}^{N}\left(\bar{Q}_{ij}\right)_k (z_k^2 - z_{k-1}^2) \tag{16}$$

$$D_{ij} \equiv \frac{1}{3}\sum_{k=1}^{N}\left(\bar{Q}_{ij}\right)_k (z_k^3 - z_{k-1}^3) \tag{17}$$

The summation is with respect to each layer of the laminate and its position along the z-axis, z_k. The reader is asked to consult Jones[21] for further explanation of the development of laminated plate theory. Returning to the development of the model for the actuator of this investigation, Equations (13) and (14) can be reduced to the form:

$$\begin{bmatrix} F \\ M \end{bmatrix} = \begin{bmatrix} A & B \\ B & D \end{bmatrix} \begin{Bmatrix} \varepsilon \\ \kappa \end{Bmatrix} \tag{18}$$

At this point in the derivation, certain assumptions can be made. It is assumed that there is no bending about the y-axis and hence no mechanism for shear, resulting in:

$$\varepsilon_{22} \equiv 0 \; ; \; \varepsilon_{12} \equiv 0 \; ; \; \kappa_{22} \equiv 0 \; ; \; k_{12} \equiv 0 \tag{19}$$

It is also assumed that the modulus of the bond layer is much less than that of the actuator and substrate:

$$E_b \ll E_a \; ; \; E_b \ll E_s \tag{20}$$

Assuming mechanical isotropy ($A_{11}=A_{22}$, $B_{11}=B_{22}$, $D_{11}=D_{22}$) and recalling the expanded matrices of Equations (13) and (14), Equation (9) reduces even further to:

$$\begin{bmatrix} A_{11} & B_{11} \\ B_{11} & D_{11} \end{bmatrix}_L \begin{Bmatrix} \varepsilon_{11} \\ \kappa_{11} \end{Bmatrix}_L = \begin{bmatrix} 2A_{11} & 0 \\ 0 & 2D_{11} \end{bmatrix}_a \begin{Bmatrix} \Lambda_{a1} + \Lambda_{a2} \\ 0 \end{Bmatrix} \tag{21}$$

The curvature can then be expressed as:

$$\kappa_{11} = \frac{2A_{11_a}(\Lambda_{a1}+\Lambda_{a2}) - A_{11_L}\varepsilon_{11}}{B_{11_L}} \tag{22}$$

Let the dimension L represent the length of the actuator from root to tip and t_a the thickness of the PZT (single sheet, 10 mil) as defined in Figure 2.3. It should recalled that the subscript L refers to the laminate. The z-location is then defined as a function of y-location, assuming that the actuator tapers linearly from root to tip and that the actuator thickness, t_a, is twice that of the substrate thickness, t_s as shown in Figure 2.3:

$$Z_s(y) \equiv \begin{Bmatrix} \frac{5t_s}{2} + t_b(y) & 0 \le y \le N \\ \frac{3t_s}{2} + t_b(y) & N < y \le L \end{Bmatrix} \tag{23}$$

$$t_b(y) \equiv \frac{38}{1000} - \frac{31}{1000}\frac{y}{L} \tag{24}$$

By inspection of manufacturer's data, the following holds within a few percent:

$$\nu_a = \nu_L = \nu \tag{25}$$

This allows Equations (15) - (17) to be rewritten, assuming that the Poisson's ratios on the left- and right-hand sides of Equation (9) cancel out:

$$A_{ij} = \sum_{k=1}^{N} E_k(z_k - z_{k-1}) \tag{26}$$

$$B_{ij} = \frac{1}{2}\sum_{k=1}^{N} E_k(z_k^2 - z_{k-1}^2) \tag{27}$$

$$D_{ij} = \frac{1}{3}\sum_{k=1}^{N} E_k(z_k^3 - z_{k-1}^3) \tag{28}$$

Due to the symmetry of the laminate and the definition of z-location as a function of the constituent thicknesses:

$$A_{a_1} = A_{a_2} = A_a = E_a Z_s(y) \tag{29}$$

$$A_{L_{upper}} = (E_a + E_L)Z_s(y) = A_{L_{lower}} = A_L \tag{30}$$

$$B_{L_{upper}} = \frac{1}{2}(E_a + E_L)Z_s^2(y)\ ;\ B_{L_{lower}} = \frac{1}{2}(E_L - E_a)Z_s^2(y) \tag{31}$$

$$B_L = B_{L_{upper}} + B_{L_{lower}} = E_L Z_s^2(y) \tag{32}$$

The subscripts “upper” and “lower” refer to the half of the laminate above and below the elastic axis, respectively.

Having assembled the necessary components of the ABBD matrices for the laminate and its constituents, the curvature of the actuator is then expressed as an integral over its length using Equations (22) and (29) - (32) and the definition of Figure 2.3:

$$\kappa_{11} = \int_0^L \left[\frac{2E_a Z_s(y)(\Lambda_{a1}+\Lambda_{a2}-\varepsilon_{11})-(E_a+E_L)Z_s(y)\varepsilon_{11}}{E_L Z_s^2(y)}\right] dy \tag{33}$$

Where ε_{11} is the strain due to actuation and thermally induced precompression:

$$\varepsilon_{11} = \varepsilon_{11_{actuation}} + \varepsilon_{11_{\Delta T}} \tag{34}$$

The strain due to thermally induced precompression is derived as follows:

$$[\bar{Q}]_L\{\varepsilon_{\Delta T}\}_L = [\bar{Q}]_s\{\alpha_s \Delta T\}_{a1} + [\bar{Q}]_a\{\alpha_a \Delta T\} \tag{35}$$

Assuming the laminate is perfectly symmetric, no coupling mechanisms exist and only thermally induced loads are being applied the following relationships are established:

$$\kappa_{11} \equiv \kappa_{22} \equiv \kappa_{12} \equiv 0\ ;\ \varepsilon_{12} \equiv 0\ ;\ [B]_s \equiv [B]_a \equiv 0 \tag{36}$$

Equation (35) then reduces to:

$$\begin{bmatrix} A_{11} & A_{12} \\ A_{12} & A_{22} \end{bmatrix}_L \begin{Bmatrix} \varepsilon_{11_{\Delta T}} \\ \varepsilon_{22_{\Delta T}} \end{Bmatrix}_L = \begin{bmatrix} A_{11} & A_{12} \\ A_{12} & A_{22} \end{bmatrix}_s \begin{Bmatrix} \alpha_s \Delta T \\ \alpha_s \Delta T \end{Bmatrix} + 2 \begin{bmatrix} A_{11} & A_{12} \\ A_{12} & A_{22} \end{bmatrix}_a \begin{Bmatrix} \alpha_a \Delta T \\ \alpha_a \Delta T \end{Bmatrix} \tag{37}$$

Following the same procedures for the derivation of thermally induced strain as were used for curvature and the definition of Figure 2.3, the thermally induced strain is expressed as:

$$\varepsilon_{11_{\Delta T}} = (1+\nu)\Delta T \frac{A_{22_s}\alpha_s\left(1-\frac{1}{\nu}\right)+A_{22_a}\alpha_a\left(2-\frac{1}{\nu}\right)}{\nu A_{11_L}-\frac{1}{\nu}} \tag{38}$$

Having previously established A_{11_L} and A_{22_a}, only the substrate constituent need be determined:

$$A_{s_{upper}} = A_{s_{lower}} = A_s = E_s Z_s(y) \tag{39}$$

Finally, the contribution to strain from thermally induced precompression can be expressed as:

$$\varepsilon_{11_{\Delta T}} = (1+\nu)\Delta T \int_0^L \left\{\frac{E_s Z_s(y)\alpha_s\left(1-\frac{1}{\nu}\right)+E_a Z_s(y)\alpha_a\left(2-\frac{1}{\nu}\right)}{\nu(E_a+E_L)Z_s(y)-\frac{1}{\nu}}\right\} dy \tag{40}$$

3 Low Net Passive Stiffness Structures

This chapter outlines the development of the underlying theory behind LNPS structures as it applies to the flutter test vane developed for this investigation. It will be shown that the implementation of this technology results in amplification of the baseline deflection levels of the actuator derived in Chapter 2.

3.1 LNPS Theory

LNPS structures are derived from the theory of perfect column buckling. As an axial force of increasing magnitude is applied to the free end of a fixed-free or pinned-free beam, the beam will approach its buckling limit resulting in large out-of-plane deflections as shown in Figure 3.1. In this case, the author defines "post-buckled" as meaning mid-point deflections being in excess of three times the local thickness of the element.

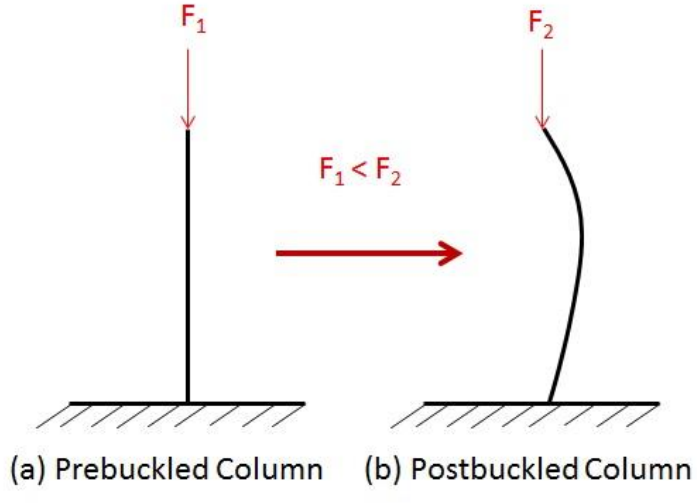

Figure 3.1 - Perfect Column Buckling

It is of extreme importance to note that this buckling limit can be breeched and still allow the structure to carry load – albeit at a much lower magnitude. It is apparent, then, that this structure has a nonlinear stress-strain curve that can be carefully manipulated to maintain load bearing capacity without structural failure, even beyond the buckling limit. Figure 3.2 displays the amplification of end rotation of a fixed-free piezoelectric bender actuator under axial load in a post-buckled precompressed (PBP) configuration.

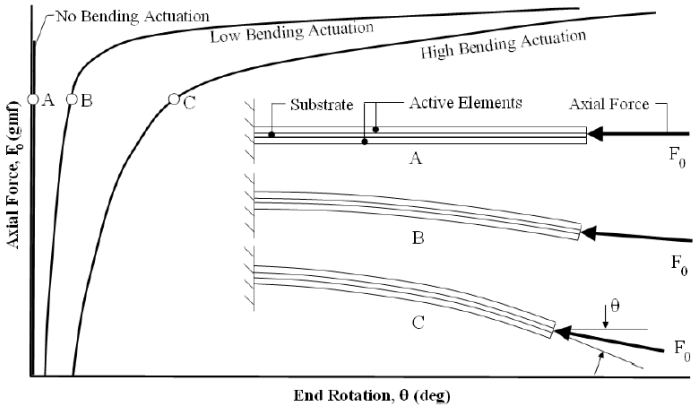

Figure 3.2 - Cantilevered Actuator Arrangement for the PBP Element[14]

Notice that the beam is passively stable (A) until actuated (B,C). With increasing activation voltage the PZT induces a structural imperfection in the form of a commanded steady-state curvature. This is perhaps best illustrated by a blocked moment diagram of a piezoelectric bender actuator as shown in Figure 3.3 - Figure 3.6.

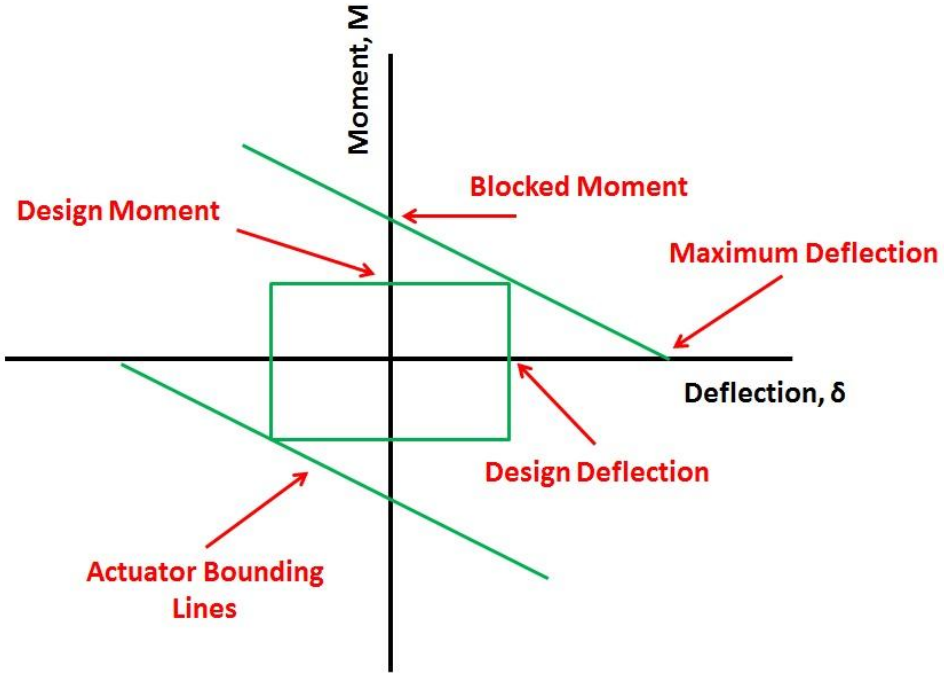

Figure 3.3 – Conventional Piezoelectric Bender Actuator Blocked Moment Diagram[9]

Figure 3.3 shows the design boundaries for conventional piezoelectric bender actuators. At zero deflection (constrained rotation), the actuator will generate the maximum moment available. At maximum deflection (free rotation), the moment generation is zero. These points create the lines shown in Figure 3.3. Since it is generally assumed that for most applications, both moment generation and tip deflection is required of piezoelectric actuators, the 50/50 point of the aforementioned curves can be chosen then to represent the operational envelope of a given actuator. When designing conventional piezoelectric bender actuators, a tradeoff then presents itself between blocked moment (force applied by the tip of the actuator) and tip rotation. By constraining the passive stiffness of the actuator through laminate design, two extreme options present themselves – low stiffness (low blocked moment, high deflection) and high stiffness (high blocked moment, low deflection), as shown in Figure 3.4 and Figure 3.5, respectively. These stiffnesses are referred to as "passive" because they refer to zero application of electrical fields to the piezoelectric sheets. As soon as an electric field is introduced to the sheets the

dipoles align, stiffening the structure and creating strain vectors as described in Chapter 2. This stiffening effect does not alter the slope of the moment-deflection curve, but instead shifts the curve with respect to the origin of the diagram. The equations of motion that describe this behavior and the effect of LNPS configurations are presented in Section 3.3. If the designer desires greater deflection a less-stiff actuator can be constructed. The tradeoff then becomes apparent by a reduction in blocked moment capability as shown in Figure 3.4.

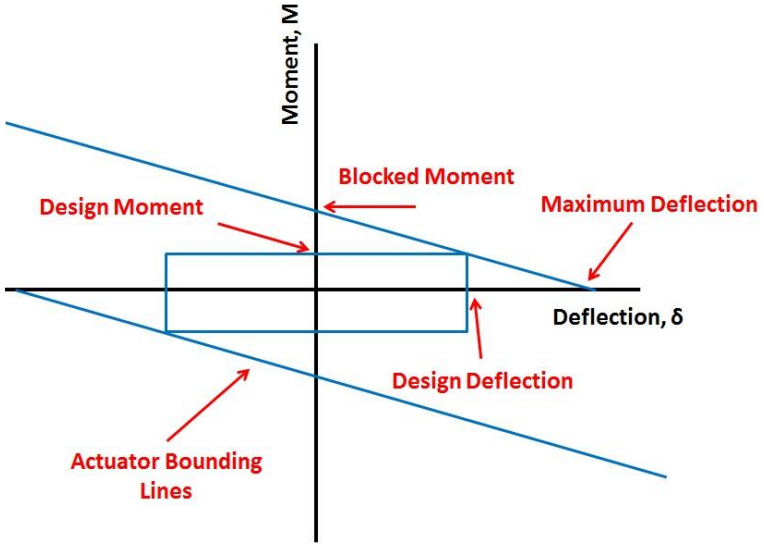

Figure 3.4 - Conventional Piezoelectric Bender Actuator Blocked Moment - High Deflection[9]

The converse is illustrated by an increase in blocked moment capability and a reduction in deflection as shown in Figure 3.5.

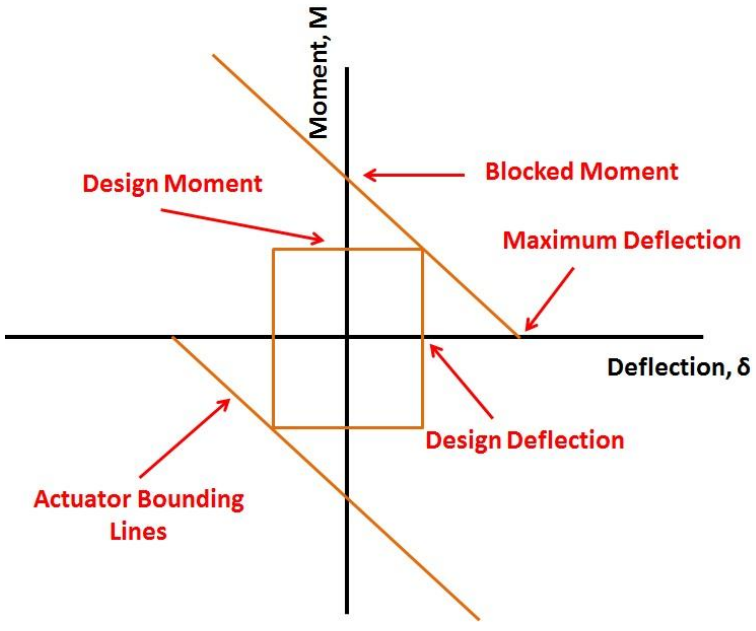

Figure 3.5 - Conventional Piezoelectric Bender Actuator Blocked Moment - Low Deflection[9]

The designer is then presented with an often very restrictive set of design boundaries, illustrated by the saddles in Figure 3.6. These saddles represent the design limits of conventional piezoelectric bender actuators. If no secondary mechanism is incorporated into the actuator design (meaning other than the laminate constituents) these design limits cannot be breached.

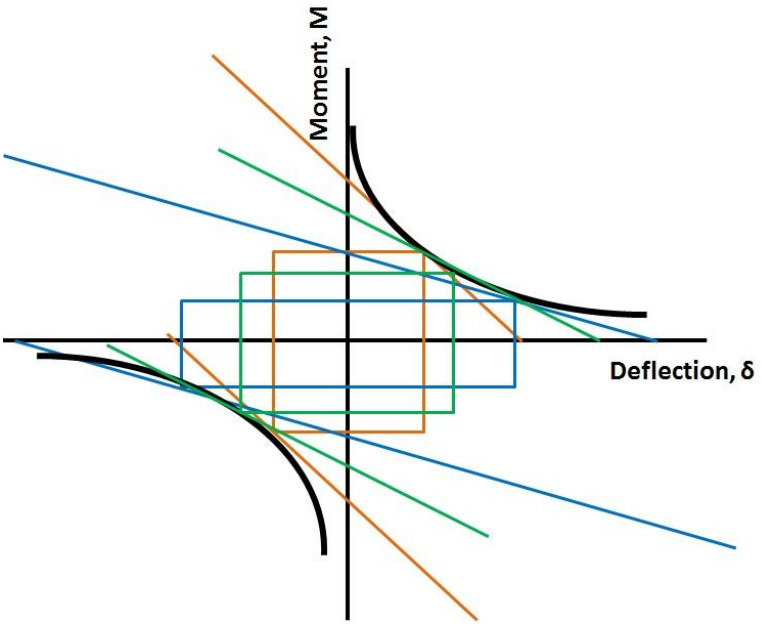

Figure 3.6 - Conventional Piezoelectric Bender Actuator Blocked Moment - Design Limits[22]

It quickly becomes apparent that these design boundaries are inhibitive, and many attempts have been made to boost deflection levels without degrading blocked moment capability. [23-26] This leads to the development of LNPS structures through the reduction of passive stiffness by means of axial force application. As described by perfect column buckling, a reduction in the structural stiffness defined by the laminate structure can be achieved by applying an axial force to the piezoelectric bender element. Figure 3.7 illustrates this concept using the blocked moment diagram of Figure 3.5. As the axial force is increased and the passive stiffness of the laminate is reduced, the slope of the moment-deflection curve changes in favor of greater deflection. In Figure 3.7, the increasing magnitude of axial force is represented by a variable, K_s. This variable refers to the increasing stiffness of a reverse-bias spring which, as the actuator deflects, rotates the force vector to "push" the tip of the actuator in the direction of deflection. This concept is explained in detail in Section 3.3.

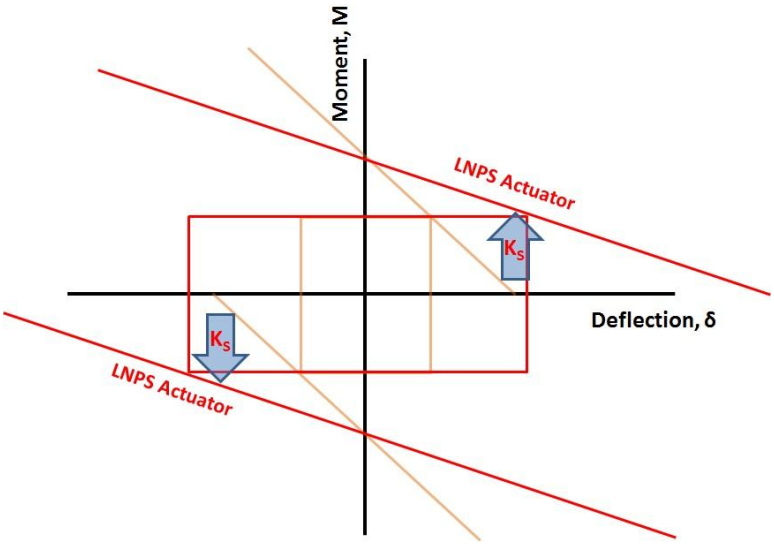

Figure 3.7 - LNPS Piezoelectric Bender Actuator Blocked Moment Diagram[9]

It is extremely important to note that this actuator has no greater blocked moment capability; however, perhaps more significantly, there is no *decrease* in blocked moment capability, either. If the stiffness is reduced even further, the laminate approaches the theoretical point of zero net passive stiffness (ZNPS), and the curves have a slope of 0. This is illustrated in Figure 3.8. If the design spaces illustrated by Figure 3.3 and Figure 3.4 are superimposed here as well, the effect on the overall saddle boundaries can be observed.

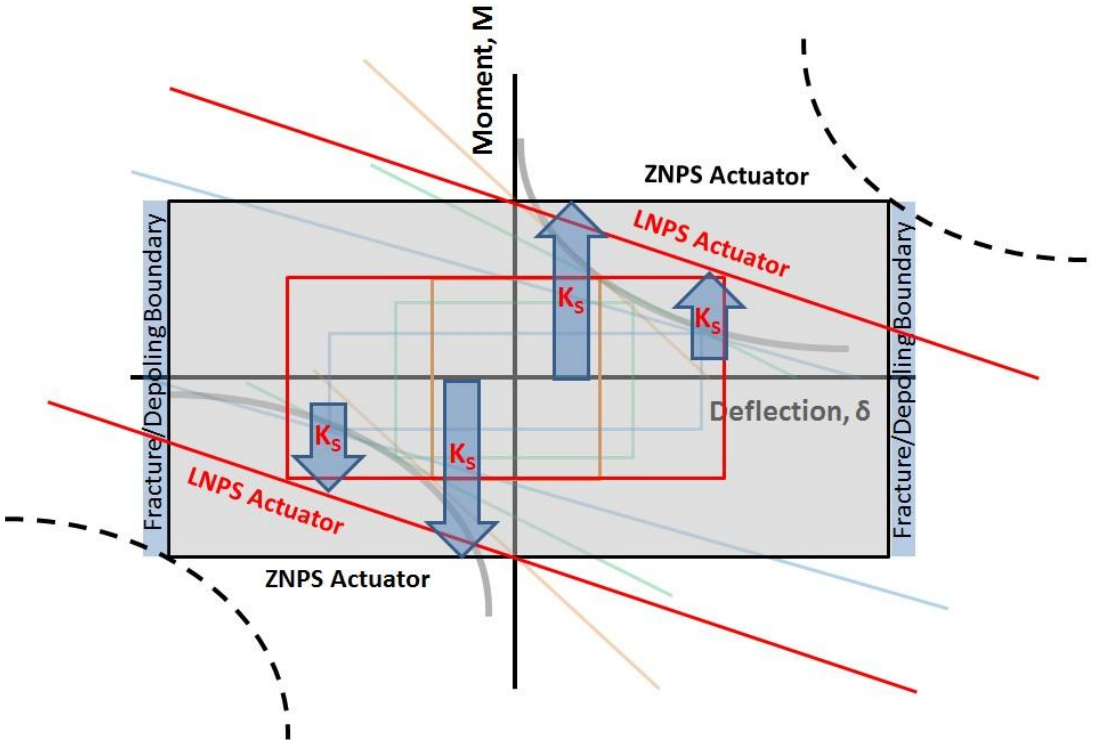

Figure 3.8 - LNPS/ZNPS Piezoelectric Bender Actuator Blocked Moment Diagram[22]

As can be seen, the saddle boundaries that define the design limits of the actuator are shifted as a function of decreasing passive stiffness (increasing K_s). When the actuator reaches the point of ZNPS, the deflection levels are infinite at a given blocked moment. As this point is approached, the actuator design is then only limited by the depoling and fracture boundaries of the actuator. For the purposes of piezoelectric actuation, these can be considered catastrophic failure mechanisms. The strains in the piezoelectric elements will become so large that they shatter, often very violently (fracture boundary). This fracture may be preceded, however, by the point at which the electrical field overwhelms the dipoles, resulting in a complete shift in the poling direction. Depoling boundaries refer to the voltage limit of the piezoelectric sheets at which point the dipoles can no longer remain aligned in the presence of an electrical field. This means that if a positive voltage of great enough magnitude (determined by the type and thickness of

piezoelectric element) is applied to a negatively poled element, the element will become positively poled. In the case of a piezoelectric bender element, this would result in two positively poled elements, turning the bender into a translation actuator. Section 5.1 discusses the depoling boundary of the piezoelectric actuators used in this investigation.

Fracture boundaries can be even further shifted with the implementation of dynamic elastic axis shifting (DEAS).[27,28] DEAS refers to the application of silicon spacers and facing sheets to a piezoelectric bender actuator as shown in Figure 3.9. This configuration allows for extreme curvatures in the actuator without fracturing the fragile piezoelectric sheets.

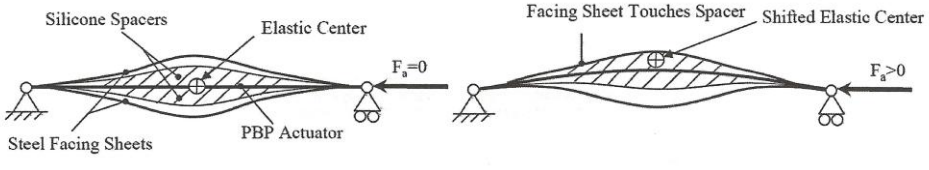

Figure 3.9 – Principle of Dynamic Elastic Axis Shifting (DEAS)[27]

The spacers in Figure 3.9 create contact between the piezoelectric elements and the facing sheets. This puts transfers some of the tensile load to facing sheet and leaves piezoelectric element in compression (due also to the nature of a *precompressed* actuator). As the tensile stress in the PZT is reduced, the fracture point is extended further than that of a conventional actuator. This concept is referred to as dynamic elastic axis shifting because, as contact is made, the elastic axis of the composite structure is shifted from the center of the laminate towards the convex surface. DEAS provides a sudden increase in bending stiffness of the laminate and is explained in great

detail in Reference 27. DEAS has been shown to successfully reduce the susceptibility of PZT fracture during actuation as a result of large curvature in the laminate.

3.2 Applications of LNPS Structures

The applications of LNPS structures become increasingly apparent when design constraints are dominated by volumetric and weight considerations. In very compact structures, such as UAVs, MAVs and weapons, volumetric and weight constraints prevent the use of conventional actuation mechanisms. The use of LNPS configurations and DEAS can reduce constraints and allow for innovative designs that push the technological limits of our time. For example, the XQ-138 platform utilizes post-buckled precompressed (PBP) actuators, a form of LNPS, to allow unparalleled control authority of a MAV in hazardous environments.[9] Similar technologies are employed in flight control mechanisms of guided munitions in the presence of tremendous launch and in-flight loads.[11] Countless additional PBP applications in UAV flight control are documented, such as those used in morphing wing structures and transonic missile fins.[14,29] This document focuses on the application of LNPS structures in the development of a flutter test vane for the certification of light aircraft. Section 3.3 outlines the theory behind this application.

3.3 Effect of LNPS Configuration on Flight Flutter Vane

The reference point for active moment generation, M_P, shown in Figure 3.10 is located at approximately the quarter chord of the symmetric airfoil which is intended to be coincident with the aerodynamic center. To determine the kinematics of the vane, this pivot point will be

referenced for all moment balance calculations. Figure 3.10 and Figure 3.11 illustrate how the following equations of motion are derived.

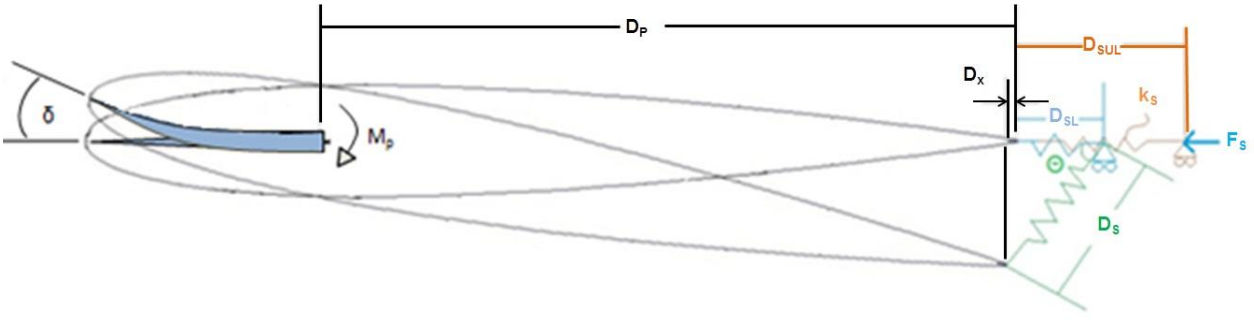

Figure 3.10 - Kinematic Definition

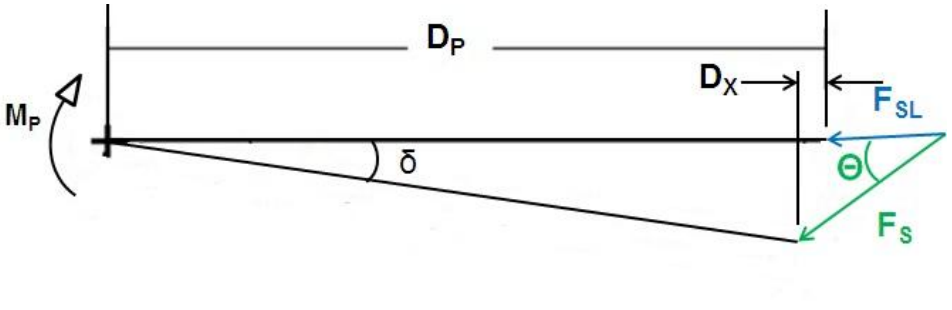

Figure 3.11 – Adaptive Flutter Test Vane Free Body Diagram (FBD)

3.3.1 Free Deflection (No Spring)

The moment about the point of rotation is defined assuming the vane is in its unamplified configuration (no LNPS) by the rotational stiffness of the piezoelectric actuator, $k_{\delta,PZT}$, the virgin strain, Λ_{PZT}, and the angular deflection, δ:

$$M_p = k_{\delta_{PZT}} \Lambda_{PZT} \tag{41}$$

$$M_p = k_\delta \cdot \delta \tag{42}$$

Combining Eq. (41) and Eq. (42):

$$\delta_{FREE} = \frac{k_{\delta_{PZT}}}{k_\delta} \Lambda_{PZT} \tag{43}$$

3.3.2 Full System Kinematics (With Spring)

Summing Moments about the pivot point:

$$\sum M_{pivot} = 0 = M_P + (F_s sin\Theta)(D_P - D_x) + (F_S cos\Theta)(D_P sin\delta) \tag{44}$$

$$M_p = -F_S[(D_P - D_x)sin\Theta + D_P cos\Theta sin\delta] \tag{45}$$

$$D_x = D_P sin\delta tan\delta = \frac{sin^2\delta}{cos\delta} \tag{46}$$

$$F_S = F_{S_L} - k_s \Delta x \tag{47}$$

$$F_{S_L} = k_S(D_{S_{UL}} - D_{S_L}) \tag{48}$$

$$\Delta x = (D_S - D_{S_L}) \tag{49}$$

$$D_S = \frac{D_P sin\delta}{sin\Theta} \tag{50}$$

Combining Eq. (45) through Eq. (50) and rearranging:

$$M_P = D_P k_S \left(\frac{sin\delta}{sin\Theta} D_P - D_{S_{UL}}\right)\left[\left(1 - \frac{sin^2\delta}{cos\delta}\right) sin\Theta + cos\Theta sin\delta\right] \tag{51}$$

Where

$$Tan\Theta = \left(\frac{D_P}{D_{S_L}}\right) sin\delta \tag{52}$$

It should be clear by Eqs. (41), (42), (51), and (52) that once the pitching moment due to the actuator (M_p) is determined, the rotational stiffness, k_δ, can be extracted. It is this value that must be manipulated to approach zero-net passive stiffness (ZNPS) by increasing the force applied by the reverse-bias spring, F_S.

4 Flutter Modeling

The fundamentals of this investigation operate on the theory that symmetric wing excitation can produce amplified deflection levels, requiring less force application from the vane. This is based on the notion that single wing (asymmetric) excitation results in aerodynamic damping caused by the tendency of the aircraft to roll to one side (body rock). The associated reduction in flapwise deflection requires greater force application at the wing tip to induce flutter. This damping

phenomenon during flight flutter testing can be quantified using the rolling moment coefficient due to roll rate, C_{lp}[30]. This section will outline the development of a two-case flutter model based on a simple spring-mass damper system as described by Inman[31].

4.1 Single Wing Excitation and Roll Damping

Governing equations for flap-dominated motions with end force being applied by the vane and allowing for dynamic body rotations:

$$I_{ow}\ddot{\Gamma} + (L_P + c_s)\dot{\Gamma} + (k_s + k_A)\Gamma - c_s\dot{\Phi} - k_s\Phi = ACos(\omega t) \tag{53}$$

$$I_{of}\ddot{\Phi} + c_s\dot{\Phi} - k_s\Phi - c_s\dot{\Gamma} - k_s\Gamma = 0 \tag{54}$$

The variables I_{of} and I_{ow} are the rotational mass moments of inertia of the fuselage and wing about the body x-axis, respectively. The variables, c_s, k_s and k_a represent the structural damping coeffiecient, wing spring stiffness, and aerodynamic spring stiffness, respectively. L_p accounts for the amount of aerodynamic damping ($C_{lp}\neq 0$); and the variables A and ω represent the amplitude of the forcing function and the frequency of oscillation, respectively. Figure 4.1 displays a pictorial representation of this nomenclature. Note the addition of m_w, m_b, b, and F_v. These variables represent the mass of the wing, mass of the body, wing span, and vertical wing force, respectively.

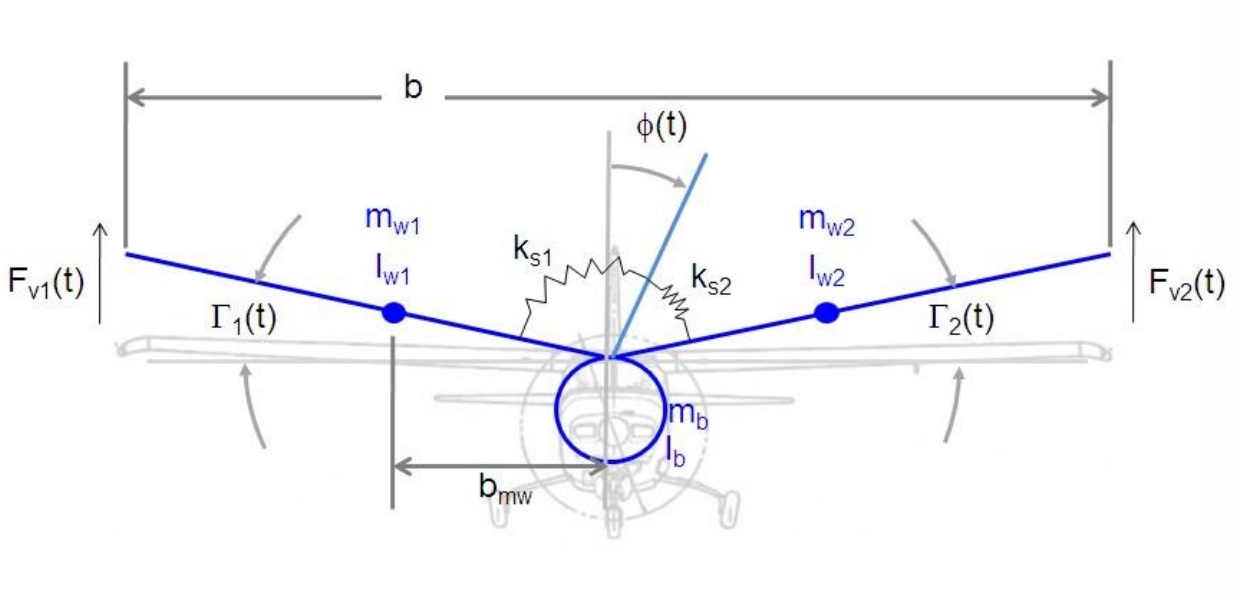

Figure 4.1 - Flutter Modeling Nomenclature

The solution to the partial differential equation defined by (53) and (54) can be shown to be:

$$\Gamma_{max}(\omega) = \sqrt{\frac{A^2\left(k_s - I_{of}\omega^2\right)^2 + c_s^2\omega^2}{\left(I_{ow}I_{of}\omega^4 - I_{ow}k_s\omega^2 - I_{of}(k_A+k_S)\omega^2 - L_P c_s\omega^2 + k_A k_S\right)^2 + \left(k_A c_s\omega + k_s L_P\omega - I_{ow}c_S\omega^3 - I_{of}L_p\omega^3 + I_{of}c_S\omega^3\right)^2}} \quad (55)$$

Solving for the natural frequency with $L_p = c_s = 0$:

$$\Gamma_{max}(t) = \frac{A\left(k_s - I_{of}\omega^2\right)}{I_{ow}I_{of}\omega^4 - I_{ow}k_s\omega^2 - I_{of}(k_A+k_S)\omega^2 + k_A k_S} \rightarrow I_{ow}I_{of}\omega^4 - \left(I_{ow}k_s - I_{of}(k_A+k_S)\right)\omega^2 + k_A k_S = 0 \quad (56)$$

$$\omega_n^2 = \frac{\left(I_{ow}k_S + I_{of}(k_A+k_S)\right) \pm \sqrt{\left(I_{ow}k_s + I_{of}(k_A+k_S)\right)^2 - 4I_{ow}I_{of}k_A k_S}}{2I_{ow}I_{of}} \quad (57)$$

$$\omega_n^2 = \frac{\left(\frac{I_{ow}}{I_{of}}k_S+(k_A+k_S)\right)\pm\sqrt{\left(\frac{I_{ow}}{I_{of}}k_s+(k_A+k_S)\right)^2-4\frac{I_{ow}}{I_{of}}k_Ak_S}}{2I_{ow}} \tag{58}$$

Since these equations for natural frequency are fairly complex, it must be ensured that that they are realistic. This is done by first assuming $I_{of} \rightarrow \infty$, as if the fuselage body represents a wall constraint:

$$\omega_n^2 = \frac{(k_A+k_S)\pm(k_A+k_S)}{2I_{ow}} = 0, \frac{k_A+k_S}{I_{ow}} \tag{59}$$

A similar constraint is applied to the wing ($I_{ow} \rightarrow \infty$), allowing the fuselage to rotate:

$$\omega_n^2 = \frac{\frac{I_{ow}}{I_{of}}k_S\pm\frac{I_{ow}}{I_{of}}k_S}{2I_{ow}} = 0, \frac{k_s}{I_{of}} \tag{60}$$

Although, realistically, these cannot truly be wall constraints (translational DOFs should not be constrained), the aircraft cannot be simply modeled in free space. These constraints are for simplicity in modeling and are considered sufficiently accurate within the confines of this derivation. Finally, the effects of aerodynamic damping are eliminated by assuming $k_A = 0$:

$$\omega_n^2 = \frac{k_S\left(1+\frac{I_{ow}}{I_{of}}\right)}{I_{ow}} = k_S\left(\frac{1}{I_{ow}}+\frac{1}{I_{of}}\right) \tag{61}$$

The results are consistent with standard spring-mass damping models[31] and it can be concluded that Eq. (55) is valid. Returning to the derivation for Case #1 and applying $k_A = 0$, the solution for maximum flap deflections with free-body rotation can be expressed by:

$$\Gamma_{maxFBR}(\omega) = \sqrt{\frac{A^2\left(k_s - I_{of}\omega^2\right)^2 + c_s^2\omega^2}{\left(I_{ow}I_{of}\omega^4 - k_S\omega^2\left(I_{ow}+I_{of}\right) - L_P c_S\omega^2\right)^2 + \left(k_s L_P\omega - I_{ow}c_S\omega^3 - I_{of}L_p\omega^3 + I_{of}c_S\omega^3\right)^2}} \quad (62)$$

Eq. (62) represents the fully-parameterized model for wing flap deflections most consistent with single-wing excitation.

4.2 Symmetric Excitation

Governing equations for flap-dominated motions with end force being applied by vane and not allowing for body rotations:

The derivation for Case #2 begins by assuming the body does not rotate:

$$I_{ow}\ddot{\Gamma} + (L_P + c_s)\dot{\Gamma} + (k_s + k_A)\Gamma = ACos(\omega t) \quad (63)$$

Solving for the relevant damping coefficients using the damping ratios, ζ:

$$\zeta_S = \frac{c_S}{2I_{ow}\omega_n} \quad (64)$$

$$\zeta_A = \frac{L_P}{2I_{ow}\omega_n} \tag{65}$$

$$\Gamma_{maxNBR}(\omega) = \frac{A}{\sqrt{\left(\omega_n^2 - \omega^2\right)^2 + (2(\zeta_A + \zeta_S)\omega_n\omega)^2}} \tag{66}$$

Eq. (66) represents the "simplified" version of Eq. (62), eliminating the effects of aerodynamic damping associated with fuselage body rock. Table 4.1 lists the necessary terms for evaluating Eq. (62) and Eq. (66) as reported by Roskam[30].

Table 4.1 - Aircraft Properties[30]

	$I_{xxtotal}$ (slug-ft^2)	$I_{xxtotal}$ (lb_m-ft^2)	Semispan Wing Weight (lb_f)	Wingspan (ft)	Estimated Y_{cgw} of Wing Location (ft)	Estimated I_{xxw} (lb_m-ft^2) (For a single wing)	Estimated I_{xxw} (lb_f-ft^2-s^2) (For a single wing)	Estimated I_{xxf} (lb_m-ft^2) (For the entire fuselage)	Estimated I_{xxf} (lb_f-ft^2-s$^{2)}$ (For the entire fuselage)	I_{xxw}/I_{xxf}	C_{lp} (/rad/s)
Cessna 172	948	30501	113	35.8	7.16	5793	180	18915	588	0.306	-0.47
Lear Model 25	28000	900872	1467	34	10.2	152627	4744	595619	18512	0.256	-0.45
McDonnell Douglas F-4	25000	804350	2172	38.7	7.74	130119	4044	544111	16912	0.239	-0.24

Letting $\zeta_s = 0.0152$ (experimentally determined - see Section 4.2.1) and A=1, values representing the natural frequency of first wing flap are plotted; however, since the data are not readily available for the aircraft presented in Table 4.1 a wide range is assumed to cover all bounds. It should also be recalled that C_{lp} of Table 4.1 is analogous to L_p of Equation (55). These parameters produce a series of plots for three very different aircraft as outlined in Section 4.3.

4.2.1 Experimental Determination of Structural Damping Ratio

The structural damping coefficient used for plotting the effect of symmetric wing excitation was determined from ground-based modal testing. A Cessna 172 wing with skin removed was mounted according to Figure 4.2. The wing was then excited in torsion at the trailing edge of the wingtip. The structure was allowed to damp out naturally and oscillations about a predetermined centerline were counted and timed.

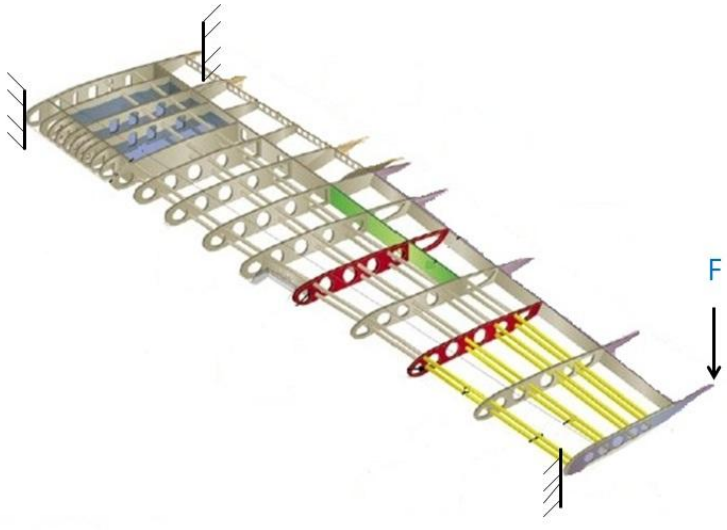

Figure 4.2 - C172 Wing Mount for Modal Testing[32]

The data was evaluated using the logarithmic decrement approach[31] and careful attention was paid to avoid capturing higher-order modes. The damping ratio was determined from:

$$\zeta_s = \frac{\delta}{\sqrt{4\pi^2+\delta^2}} \tag{67}$$

$$\delta = ln\left(\frac{x(t)}{x(t+T)}\right) \tag{68}$$

Where x(t) is the amplitude of oscillation and T is the period of oscillation.

It is assumed that the aircraft of Table 4.1 are all manufactured using similar techniques, such as connections between structural members constructed with rivets. The damping ratio can be then applied to each of them for the plots of Section 4.3. A representative range of the data collected in four separate tests is shown in the underdamped response of Figure 4.3. This data led to an average structural damping ratio of $\zeta_s = 0.0152$.

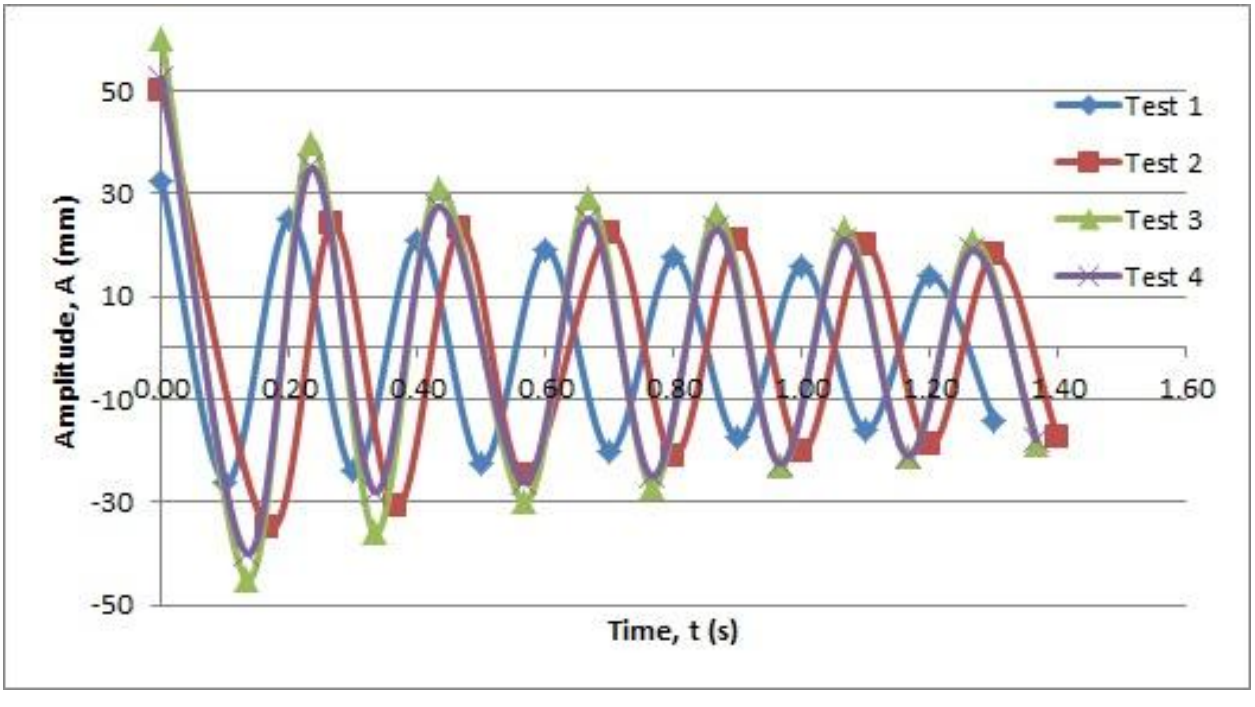

Figure 4.3 - C172 Wing Damping Results

4.3 Implications of Symmetric Wing Loading

Figure 4.4 illustrates the theory described in the previous sections. With asymmetric wing loading, $F_{v1}(t)$ is not equal in magnitude and/or phase to $F_{v2}(t)$, resulting in (often) very large nonzero fuselage rotation, $\varphi(t)$. When $F_{v1}(t)$ and $F_{v2}(t)$ are equal in both phase and magnitude, the body rotation is significantly reduced. Theoretically this value can be driven to zero resulting in much greater wingtip deflections.

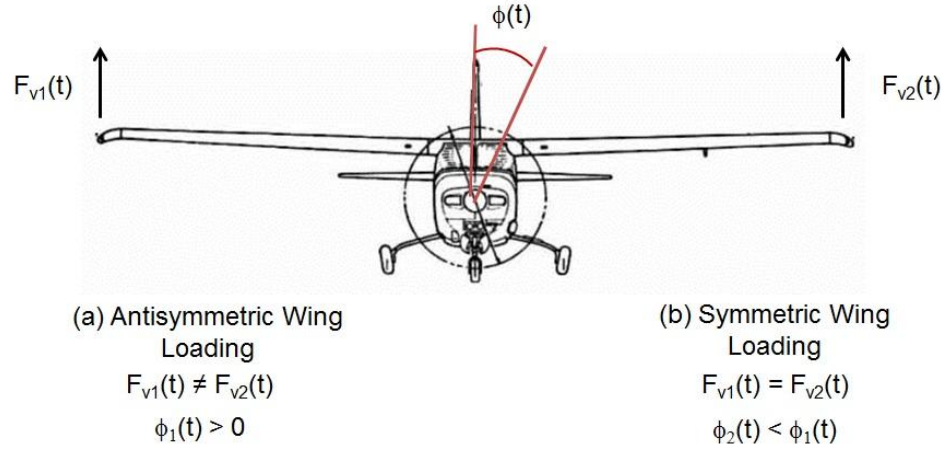

Figure 4.4 - Symmetric and Asymmetric Wing Loading

Figure 4.5 - Figure 4.13 illustrate the results from the theoretical model of Sections 4.1-4.2 in an attempt to validate the aforementioned deflection amplification.

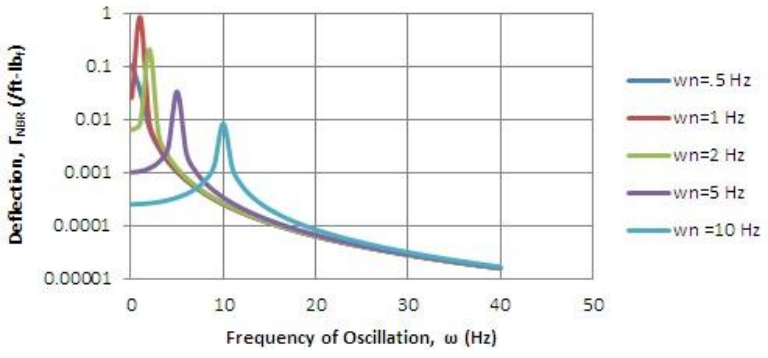

Figure 4.5 - Cessna 172 Deflections: No Body Rock

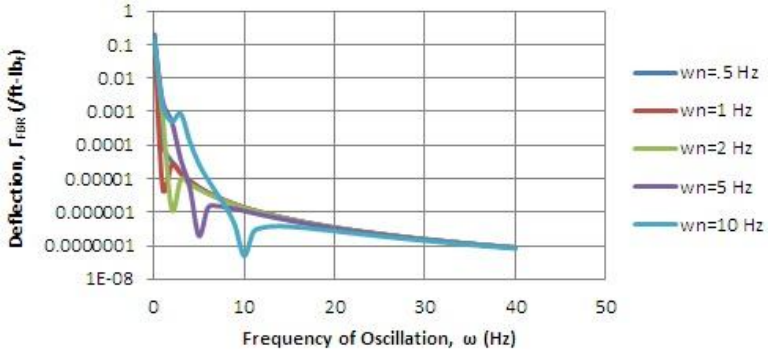

Figure 4.6- Cessna 172 Deflections: Free Body Rock

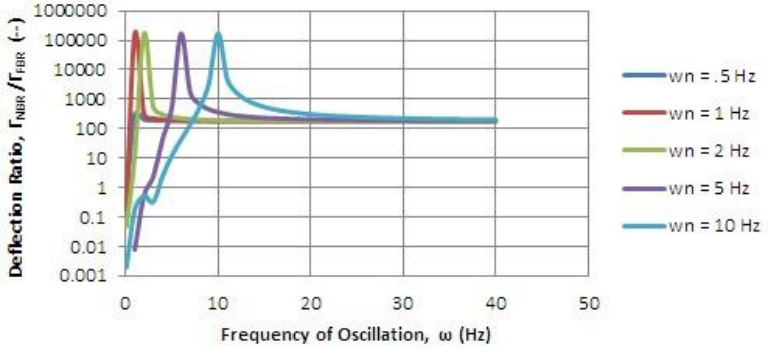

Figure 4.7- Cessna 172 Deflections: Amplification Ratio

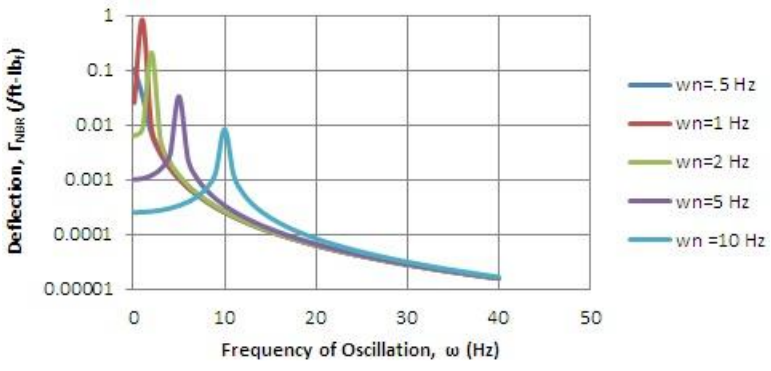

Figure 4.8 - Lear Model 25 Deflections: No Body Rock

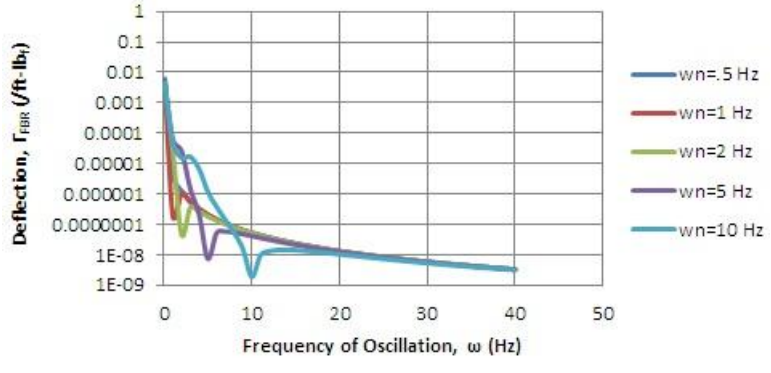

Figure 4.9 - Lear Model 25 Deflections: Free Body Rock

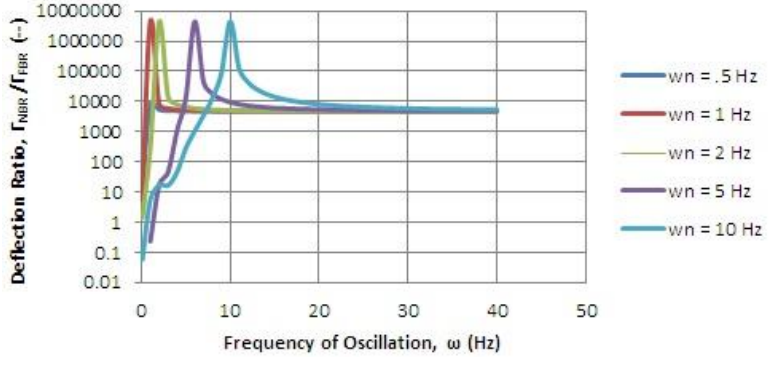

Figure 4.10 - Lear Model 25 Deflections: Amplification Ratio

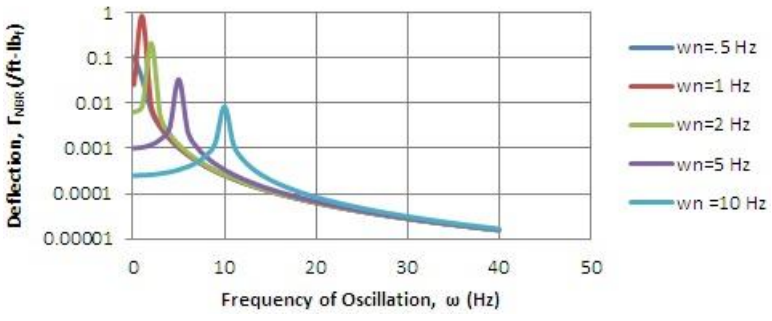

Figure 4.11 - McDonnell Douglas F-4 Deflections: No Body Rock

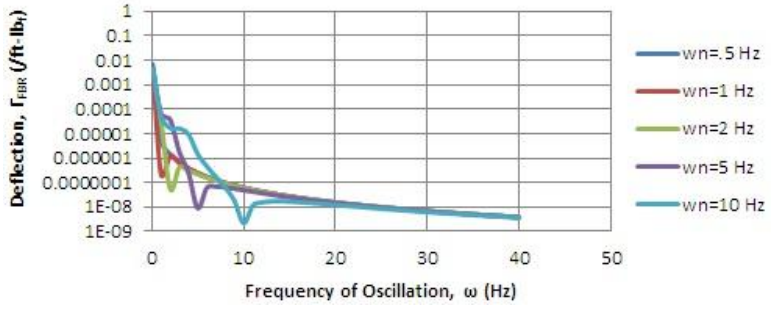

Figure 4.12 - McDonnell Douglas F-4 Deflections: Free Body Rock

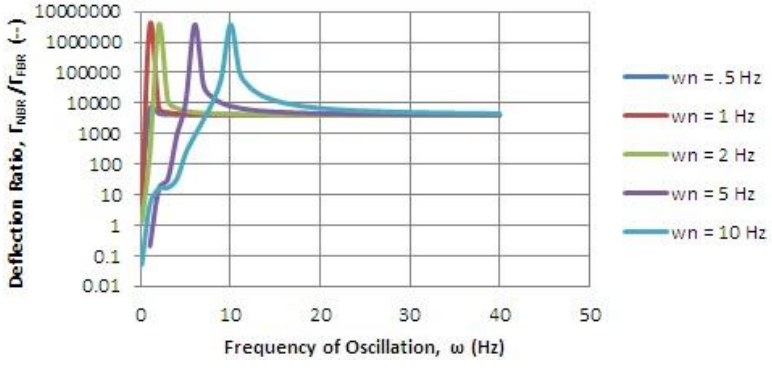

Figure 4.13 - McDonnell Douglas F-4 Deflections: Amplification Ratio

The results of Figure 4.5 - Figure 4.13 are quite remarkable. The low damping coefficient fidelity (i.e. no plunge aerodynamics modeled) results indicate that symmetric wing excitation could theoretically provide amplification ratios of approximately 180:1 for a Cessna 172 and 8000:1 for a Lear Model 25 or McDonnell Douglas F-4 when compared to single wing excitation. Preliminary results from experimental validation of this model are discussed in Section 4.3.1. It should be noted here that the wing/fuselage interaction is not modeled in its entirety in the derivations of Sections 4.1 and 4.2. By allowing the fuselage to rotate, the response of the wings can potentially see an increase in tip deflection through an increase in energy produced by the oscillations themselves. This phenomenon also has the potential to be amplified by the plunging motion of the aircraft in the body x-/z- plane. Due to the complexity of such a model and the need for additional aerodynamic damping terms in the derivation of Equations (62) and (66), such effects were not taken into account. The equations presented in this section are to be considered a proof of concept for the amplification of wingtip deflection through the manipulation of the symmetry or asymmetry conditions.

4.3.1 Experimental Results and Validation

To validate this model, acoustic puffers were positioned beneath a Froude-scaled[33] Cessna 210 model as shown in Figure 4.14 and Figure 4.15. These puffers allowed for oscillating aerodynamic forces to be applied directly to the wingtip of the model from slots in a baseplate mounted to a stereo subwoofer. This baseplate was constructed from ¼" hardwood to prevent deformations due to the increased pressure at the face of the speaker. This insured that only forces were being applied at the tip of the wings, simulating vane excitation loads as accurately

as possible. Both single-wing excitation and symmetric-wing excitation scenarios were investigated.

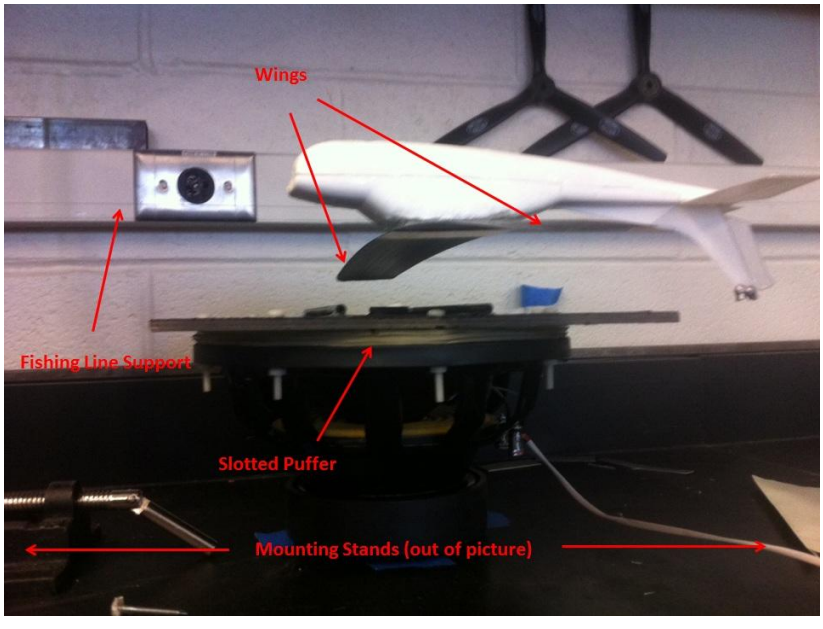

Figure 4.14 - Froude-Scaled Cessna 210 Mounted Above Acoustic Puffer (View 1, Scale 1:6)

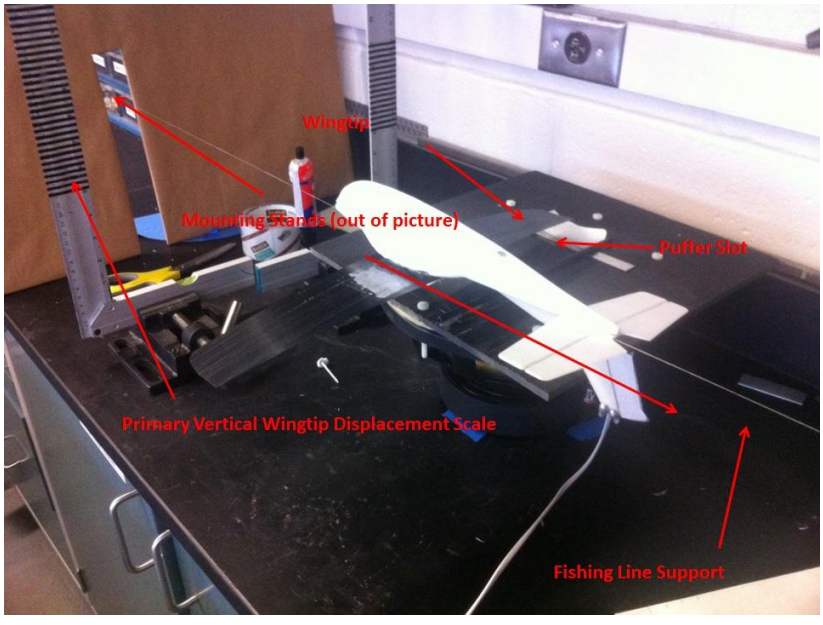

Figure 4.15 - Froude-Scaled Cessna 210 Mounted Above Acoustic Puffer (View 2, Scale 1:8)

The C210 model was suspended loosely about the body z-axis using fishing line to allow the aircraft to plunge vertically as would be seen in-flight. The mounting stands are positioned well beyond the borders of this image to allow virtually zero resistance to vertical translation. Although the theoretical model specifically eliminates plunge from the analysis, it is quite difficult to replicate this experimentally. It was therefore determined that allowing as much plunge as is reasonable (rather than restricting it) would produce more reliable and accurate results. The author highly recommends that plunge aerodynamics be incorporated into future models and compared to the results presented in this section. The model was mounted inverted (as shown) as well as level to reduce the potential corruption of data due to the effects of gravity on the natural curvature of the wing structure. Table 4.2 outlines the results of experimental validation of the flutter model derived previously.

Table 4.2 - Experimental Results of Flutter Modeling

Frequency (Hz)	Symmetric Wing Excitation			Single Wing Exitation			Amplification Ratio	
	Wing	Body		Wing	Body			
	Linear Deflection (in)	Linear Deflection (in)	Angular Deflection (deg)	Linear Deflection (in)	Linear Deflection (in)	Angular Deflection (deg)	Wing	Body
2.9	0.10	0.3	1.25	0.05	0.3	1.25	2.000	1.000
3	0.1	0.3	1.25	0.05	0.2	0.83	2.000	1.500
3.1	0.1	0.2	0.83	0.05	0.2	0.83	2.000	1.000
3.2	0.1	0.3	1.25	0.05	0.3	1.25	2.000	1.000
3.3	0.15	0.2	0.83	0.1	0.3	1.25	1.500	0.667
3.4	0.1	0.3	1.25	0.05	0.3	1.25	2.000	1.000
3.5	0.1	0.2	0.83	0.1	0.2	0.83	1.000	1.000
3.6	0.2	0.3	1.25	0.1	0.2	0.83	2.000	1.500
3.7	0.50	0.3	1.25	0.2	0.4	1.67	2.500	0.750
3.8	0.6	0.4	1.67	0.3	0.4	1.67	2.000	1.000
3.9	0.5	0.6	2.50	0.2	0.3	1.25	2.500	1.999
4	0.5	0.6	2.50	0.3	0.7	2.91	1.667	0.857
4.1	0.4	0.6	2.50	0.2	0.7	2.91	2.000	0.857
4.2	0.2	0.4	1.67	0.15	0.5	2.08	1.333	0.800
4.3	0.2	0.2	0.83	0.1	0.4	1.67	2.000	0.500

The results of Table 4.2 only illustrate a portion of the discoveries of these experiments. Most notably, a 250% increase in linear wingtip deflection levels with a 25% reduction in fuselage body rock is observed (highlighted in red). The wingtip deflection data was collected by visual inspection using the black and grey scale shown in Figure 4.15. Very careful attention was paid not to include the total body pitch/plunge amplitude in these measurements by viewing the deflections from the front (looking down the body z-axis) and the side (looking down the body y-axis). Fuselage body rock was determined using laser light reflection off of a very small mirror centered on the body z-axis. The details of data collection using laser light reflection are discussed in Section 5.2. Due to the very coarse resolution of the data extraction techniques, these results are the maximum amplifications that the author is comfortable presenting. Higher amplification ratios were observed; however, these results were inconsistent and difficult to reproduce. Also highlighted in Table 4.2 is an inconsistency amplification trends due to a secondary vibrational mode – tail wagging – that was excited by the puffers (highlighted in

orange). The implications of this finding suggest that the adaptive flutter test vane can be used for more than just exciting wing flutter.

5 Bench Testing

The first step in evaluating the performance of the adaptive flight flutter test vane is to perform a series of bench tests. These tests will be used to determine the net passive stiffness of the structure as well as its operational envelope. The following sections will outline the procedures for evaluation.

5.1 Vane Actuator Operations

Before delving into the "full system" bench tests, the physical and electrical limitations of the piezoelectric bimorph actuator must first be addressed. As was discussed in Section 2.3, the piezoelectric sheets used were 10 mil lead-zirconate-titanate (PZT) 5H. Arranged in a tapered bimorph configuration, these sheets were found to have an approximate depoling voltage of 20 V/mil. This implies that if a positive 200 V command is applied to the negatively poled PZT sheet the polarity will flip. This phenomenon puts an electrical limitation on the actuator, preventing the bimorph from bending as it was intended (depoling boundary). The way around this is to carefully tailor the sinusoidal DC waveform in an attempt to maximize the command voltage and simultaneously prevent depoling. In the interest of minimizing part count and weight, as well as reducing complexity of the entire flutter vane system, the following configuration was established:

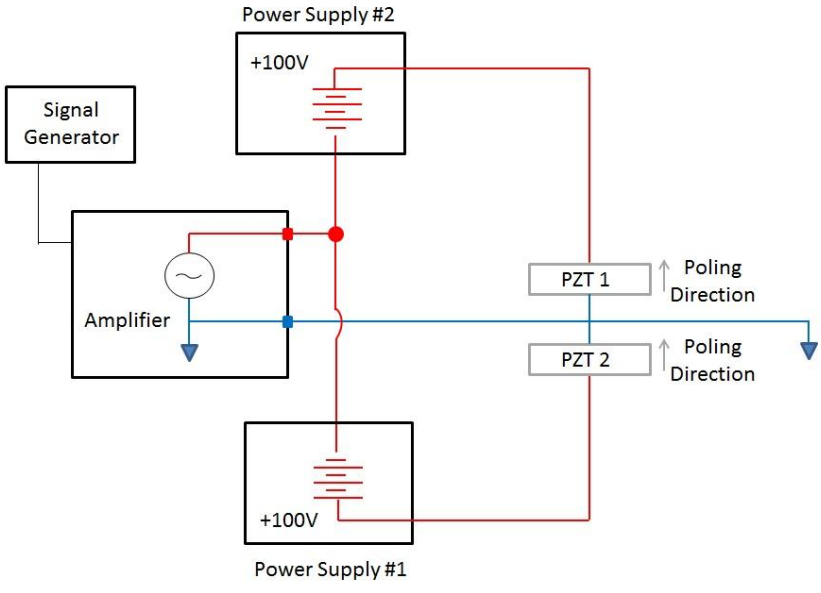

Figure 5.1 - Flutter Vane Wiring Diagram

It should be noted that the DC power supplies shown in Figure 5.1 are physically located within the piezo linear amplifier, shown in Figure 5.2, and utilizes its power source. This eliminates the need for extra mounting hardware and power supply on the aircraft during flight testing. What this diagram implies is at the "maximum command voltage", CV= ±180V, the bimorph actually experiences +280 V to the positively poled sheet and +80 V to the negatively poled sheet (or -80 V to the plus and -280 V to the minus) as the maximum. This prevents depoling in the system whilst increasing the electrically induced deflections. This is illustrated in Table 5.1.

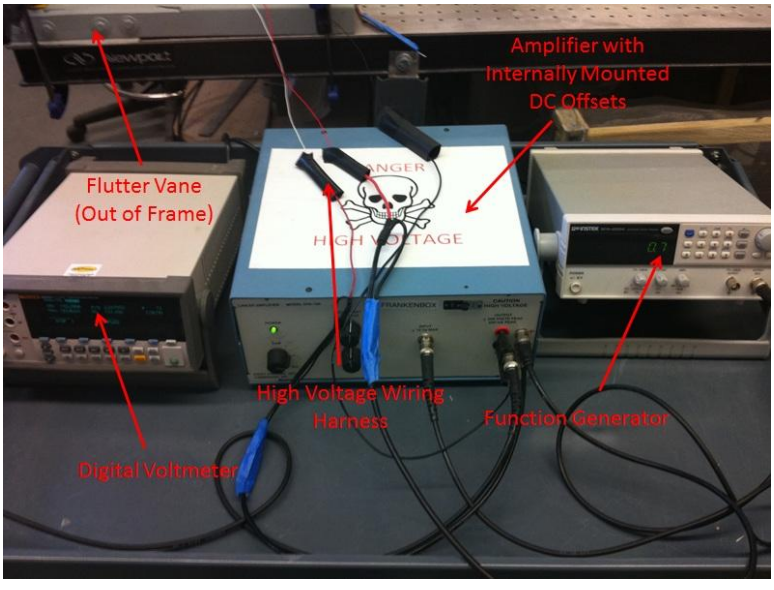

Figure 5.2 - Electronics Setup

Table 5.1 - Amplifier Input vs. Output

Input Command Voltage, CV (V)	Output to Positively Poled PZT Sheet (V)	Output to Negatively Poled PZT Sheet (V)
-180	-80	-280
-160	-60	-260
-140	-40	-240
-120	-20	-220
-100	0	-200
-80	20	-180
-60	40	-160
-40	60	-140
-20	80	-120
-0	100	-100
20	120	-80
40	140	-60
60	160	-40
80	180	-20
100	200	0
120	220	20
140	240	40
160	260	60
180	280	80

The physical limitations of the PZT bimorph were discovered quite quickly during the development phase of this device. Amplifying the deflection levels of a piezoelectric actuator

subjects the PZT sheets to strain-induced micro-cracking. These micro-cracks open and close as the actuator bends allowing the electrical signal to arc across the gap. This is not only physically dangerous due to the high command voltages, but it also reduces the effectiveness of the actuator. This phenomenon is avoided by applying a very thin layer of polyurethane paint to the surfaces of the actuator. This highly elastic coating reduces the tendency for micro-cracking and, in the event that these cracks still form, prevents arcing. Other methods to prevent complete actuator failure, such as the tapered configuration and thermally induced precompression, were discussed in Section 2.3.

5.2 Quasi-Static Testing

Quasi-static bench testing of the adaptive flight flutter test vane served to not only evaluate the performance of the actuator mechanism, but also the manufacturing techniques and design tolerances. It was quickly discovered that the performance of this system is hypersensitive to any source of friction, minimal or otherwise. Custom fittings and bearing assemblies were incorporated into the internal structure and exterior LNPS configuration to maximize the angular deflection of the vane with minimal weight penalty.

It should be noted here that the quasi-static bench testing consisted primarily of establishing the maximum deflection levels in the standard configuration (no LNPS). These values were then used as a baseline for comparison with the new mounting assembly in the wind tunnel (see Section 6.1). Sections 6.2 and 6.3 show data for V=0 ft/s, which mimic the conditions of bench testing. The reader is therefore directed to these sections for the full gamut of bench results. The

test setup is shown in Figure 5.3. It should be noted that the mirror used for angular deflection measurements via laser light reflection is mounted along the axis of rotation on the under-side of the vane to prevent inconsistencies in data collection caused by translation of the reflective surface.

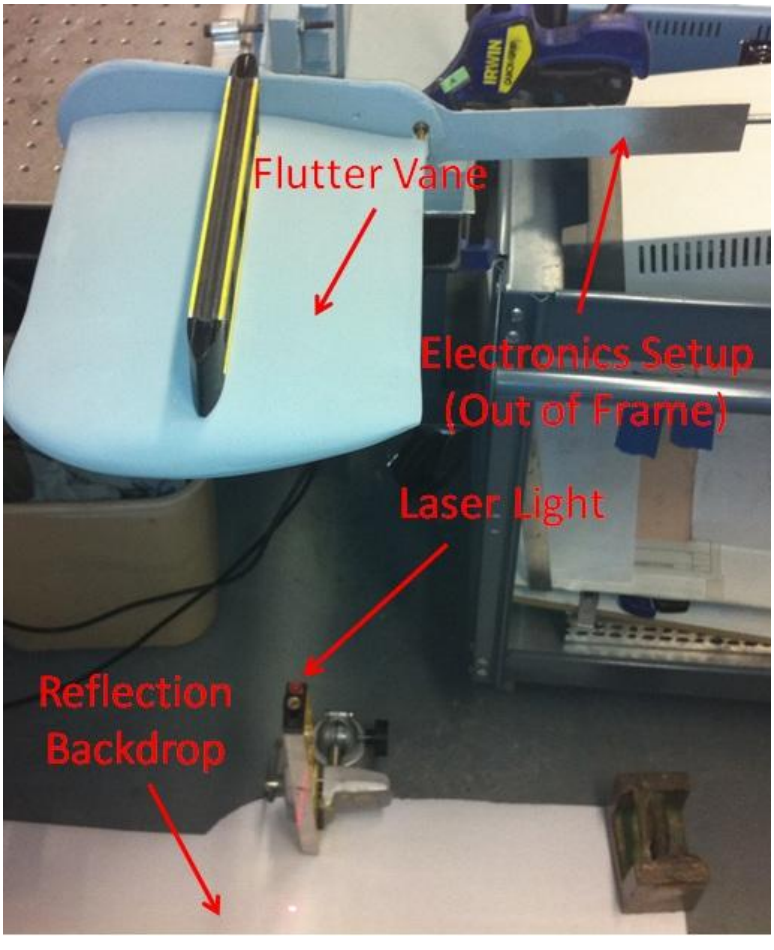

Figure 5.3 - Bench Testing Setup

Deflection measurements are taken by bouncing a laser off of the mirror and determining the relationship between linear translation and angular deflection according to:

$$Tan(2\delta) = \frac{Linear\ Translation\ of\ Laser\ Dot}{Distance\ between\ mirror\ and\ backdrop} \tag{69}$$

Quasi-static bench testing was carried out at ω=0.7 Hz and the results are shown in Table 5.2. The notation 2δ refers to the peak-to-peak (P2P) angular deflection. It should be recalled that the command voltages do not reflect the DC offset as discussed in Section 5.1.

Table 5.2 - Quasi-Static Deflections - No Spring, ω=0.7 Hz

Command Voltage, CV	Angular Deflection, 2δ (deg)
	No Spring
100	0.8
120	0.975
140	1.245
160	1.45
180	1.74

The data presented does not extend below CV=±100 V due to issues with resolution. When deflections are small, the width of the laser used for measurement has the potential to overshadow the linear deflections. More data at lower command voltages can be found in Sections 6.2 and 6.3.

Also of extreme importance here is to discuss the blocked force capability of this device. This information is invaluable when one recalls that the LNPS configuration *does not* degrade blocked force capability, but rather increases the deflections at the expense of the stiffness of the structure as discussed in Sections 3.1 and 3.2. Blocked forces and moments define the design spaces for piezoelectric actuators and are the best way to evaluate the performance improvement[9,34]. Figure 5.4 and Figure 5.5 display the blocked force capability of the adaptive flight flutter test vane. The variable δ represents ½ peak-to-peak (P2P) deflection.

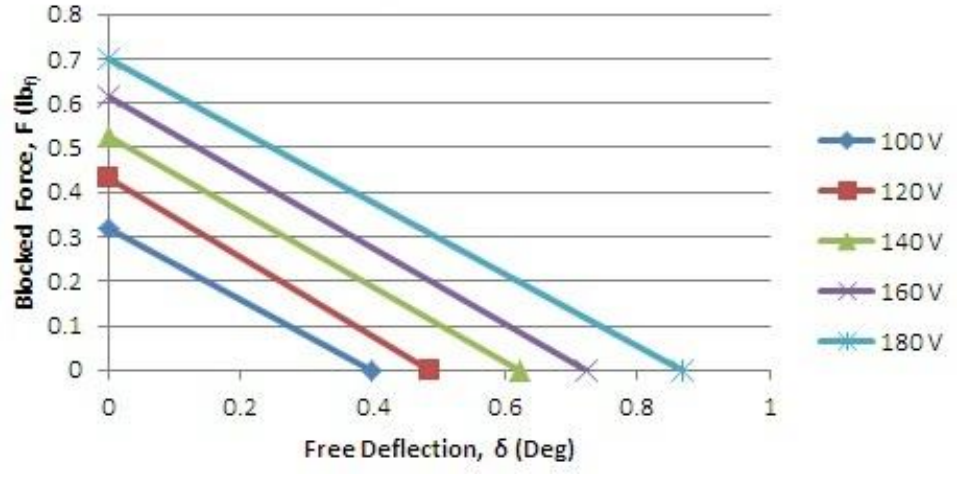

Figure 5.4 - Blocked Force - Right Wing Up

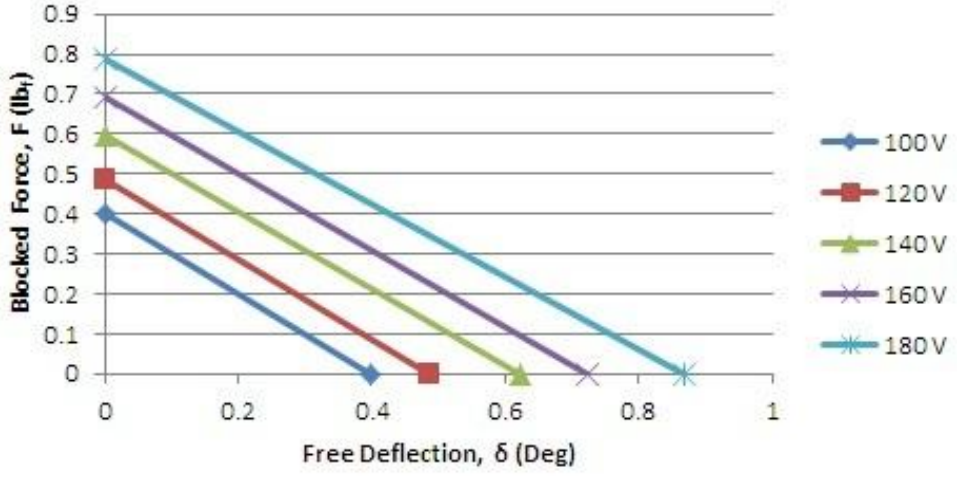

Figure 5.5 - Blocked Force - Left Wing Up

The conventions “Right/Left Wing Up” (R/LWU) are a reference to the orientation of the vane if it were to be attached to the right or left wing/tail of an aircraft. The significance of this clarification is simply that, due to potential manufacturing anomalies, the piezoelectric bimorph actuator outputs slightly more force when deflecting LWU. This is most likely due to a slight

difference in bond thickness between the piezoelectric sheets and the substrate. These two conventions are averaged together and presented in the most common form, a blocked moment diagram, in Figure 5.6.

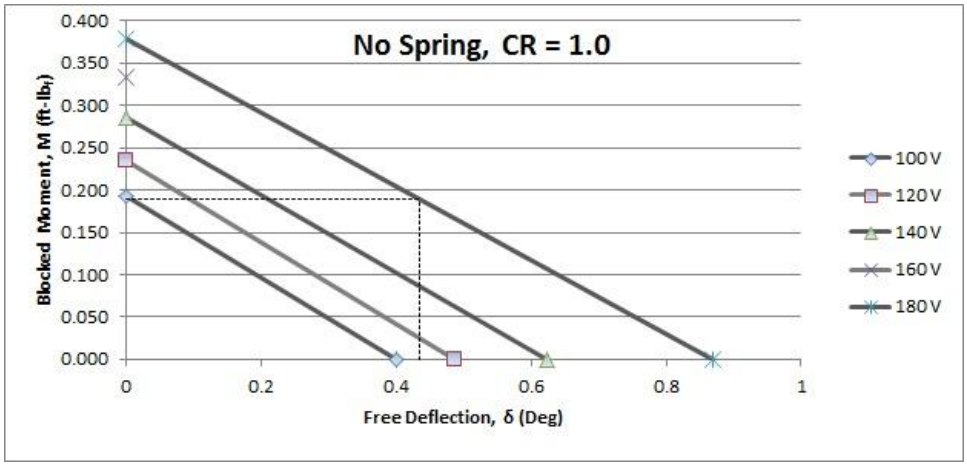

Figure 5.6 - Blocked Moment Diagram - Unamplified Configuration

The designation "CR=1.0" refers to the unamplified configuration (no LNPS) and will be discussed further in Section 5.2.1. The design space for max-voltage operation is highlighted by the 50/50 (moment/deflection) point. This data will be used for evaluation of the effectiveness of the LNPS configurations.

5.2.1 Development of LNPS Configurations

In the testing phase, the design of the reverse-bias spring was optimized for this particular device. The applications of this technique extend far beyond what is presented here so the reader is urged to take caution when analyzing the data presented. The following discussion outlines

the development of three spring configurations, each with different stiffness properties. It should be noted that the numbering of the spring systems (Spring M only) do not indicate a physical change in spring, but rather a manipulation of the spring geometry according to the diagram displayed in Figure 5.7.

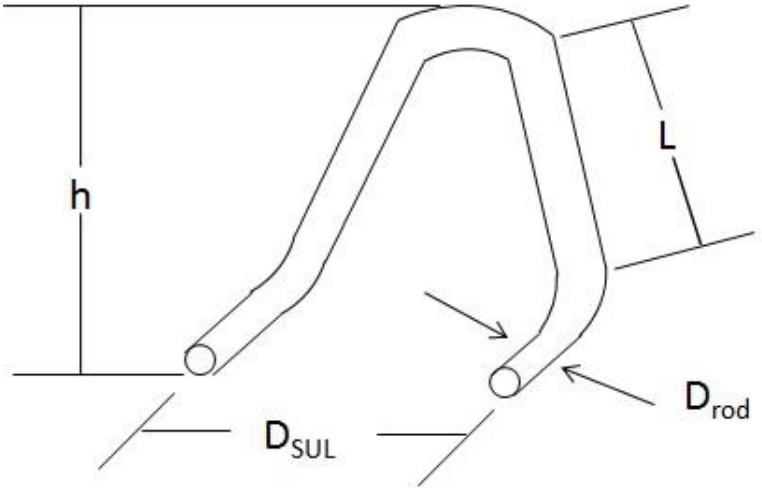

Figure 5.7 - Reverse-Bias Spring Nomenclature

D_{rod} is the diameter of the material used for the springs. Both stainless steel and carbon steel rods were used for variations in material stiffness. The variables h and L refer to the height of the spring and the length of any one side, respectively. These parameters allow for indirect control of the radius of curvature at the peak of the spring. D_{SUL}, as mentioned in Figure 3.10 of Section 3.3, is the unloaded spring length which is used for the majority of the reverse-bias control. All of these parameters have a dramatic effect on the outcome of any given LNPS configuration, and careful attention must be paid to the effect of each. In total, 13 different springs were manufactured and their *material* stiffness values were determined. This refers to the amount of compression between pegs (the compression from D_{SUL} to D_{SL} alluded to in Section 3.3) at a

given force level. Material stiffness was determined using an Instron® machine and the setup shown in Figure 5.8.

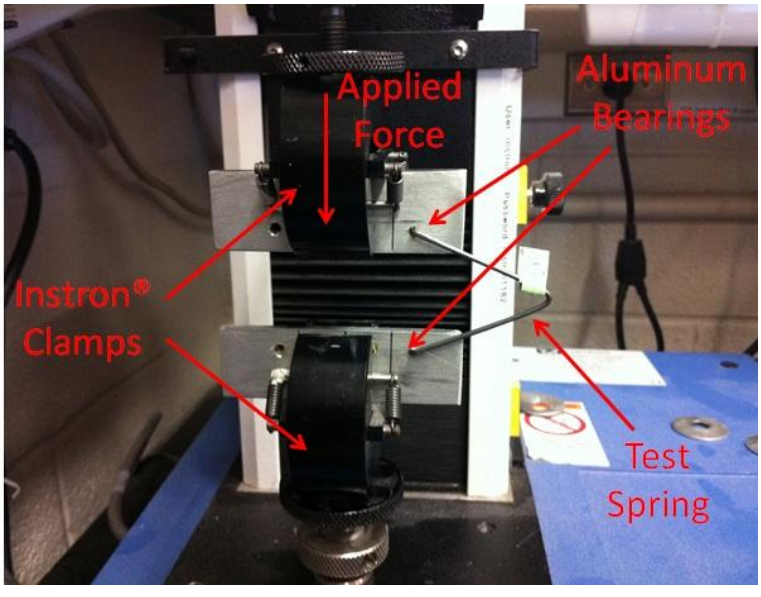

Figure 5.8 - Spring Stiffness Determination (Scale 1:2)

This setup provides a rotational degree of freedom at each peg to match the boundary conditions of the flutter vane setup. In reality, the only difference between this setup and the real component is that the force vector applied to each peg does not rotate. This is trivial, considering that in the real setup the spring rotates as the vane does, keeping the force vector normal to the base of the triangular spring. The material stiffness is calculated recalling that:

$$F = k\Delta x \tag{70}$$

Table 5.3 - Spring Stiffness Determination

Spring	Material	h_s (in)	D_s (in)	D_{SL} (in)	D_{SUL} (in)	K_S(lb/in)
A	Carbon Steel	1.213	0.0625	0.7	0.950	17.85
B	Carbon Steel	1.695	0.0930	0.7	0.950	25.99
C	Carbon Steel	1.562	0.0625	0.7	1.640	6.25
D	Carbon Steel	2.314	0.0625	0.7	1.600	3.10
E	Carbon Steel	3.137	0.0625	0.7	1.622	1.11
F	Stainless Steel	3.297	0.1250	0.7	1.605	12.98
G	Carbon Steel	4.090	0.1200	0.7	2.285	7.05
H	Stainless Steel	3.832	0.1250	0.7	2.448	7.25
I	Carbon Steel	3.950	0.0920	0.7	2.915	2.05
J	Carbon Steel	1.480	0.0625	0.7	1.355	6.95
K	Carbon Steel	1.783	0.0780	0.7	1.700	11.14
L	Carbon Steel	1.950	0.0780	0.7	1.960	8.47
M	Carbon Steel	1.992	0.0780	0.7	1.765	8.15

These springs were then each used on the flutter vane setup during bench testing to determine the most effective and reliable configuration. An interesting discovery was made, in that the spring is less effected by material stiffness than by compression ratio, which is defined by:

$$C.R. = \frac{D_{S_{UL}}}{D_{S_L}} \tag{71}$$

Compression ratio is illustrated in Figure 5.9 and Figure 5.10. The reader is asked to refer to Figure 3.10 of Section 3.3 for additional explanation of the LNPS configuration. Controlling compression ratio was done by yielding the spring at its apex to either increase or decrease D_{SUL}. It is understood that doing this numerous times would damage the integrity of the spring and introduce scatter into the data. Yielding the material into a new equilibrium state was performed the minimum necessary times to perform the required bench and wind tunnel tests.

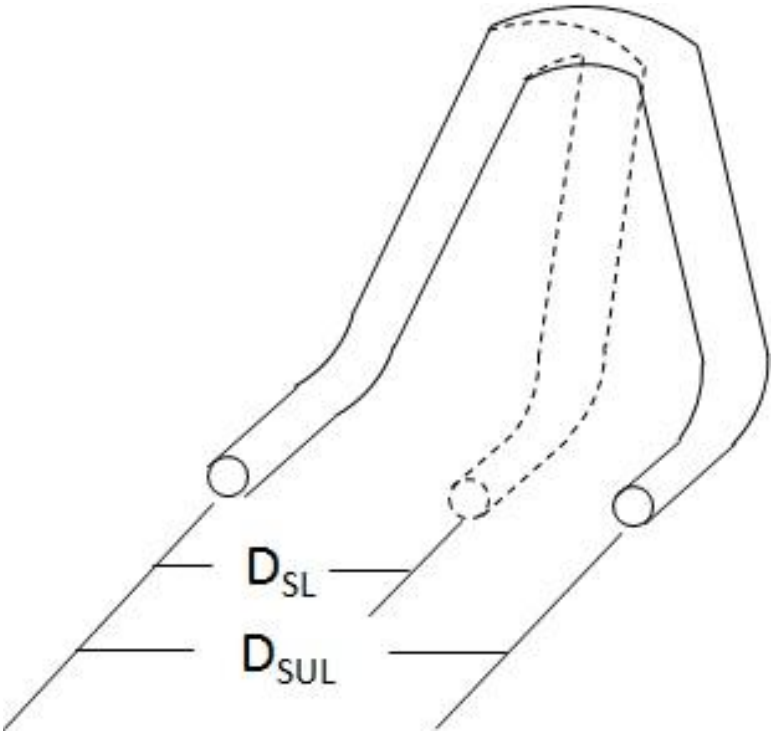

Figure 5.9 - Compression Ratio Nomenclature

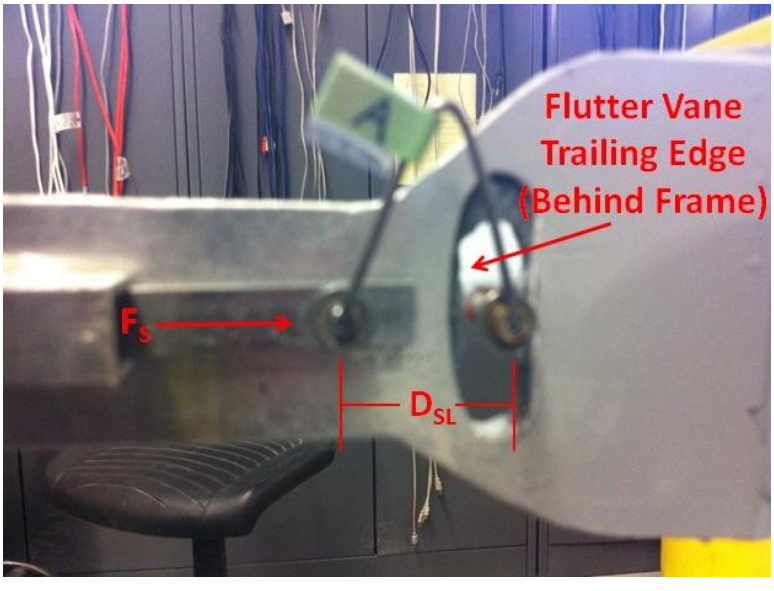

Figure 5.10 - Loaded Spring at Flutter Vane Trailing Edge

While material stiffness is the driver for controlling snap-through behavior (discussed in Section 6.3.2), it is not the driver for effective angular deflection amplification. This is illustrated in Figure 5.11, Figure 5.12 and Table 5.4.

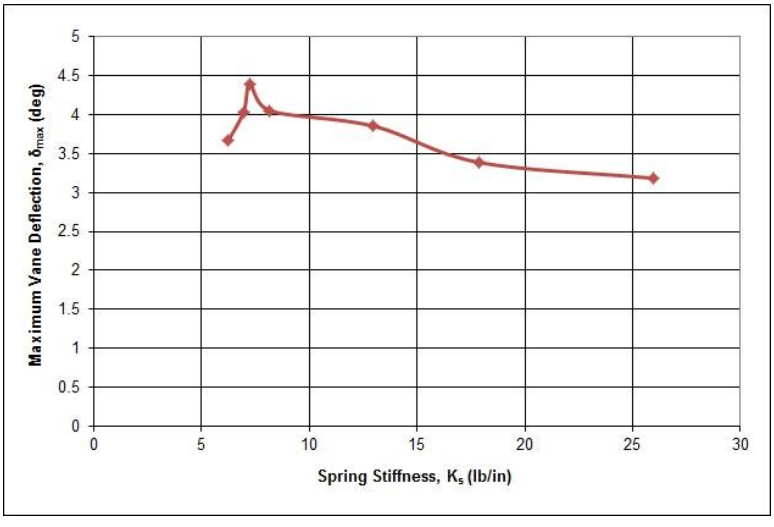

Figure 5.11 - Deflection as a Function of Material Stiffness

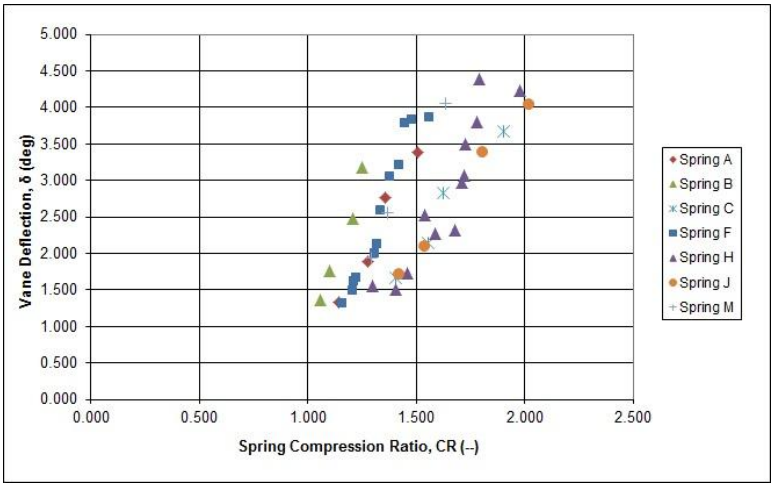

Figure 5.12 - Deflection as a Function of Compression Ratio

Table 5.4 - Spring Development Summary

Spring	δ_{max} (deg)	K_s (lb/in)	Compression Ratio, ζ
C	3.671	6.25	1.904
J	4.032	6.95	2.021
H	4.389	7.25	1.791
M1	4.05	8.15	1.637
F	3.852	12.98	1.473
A	3.387	17.85	1.506
B	3.182	25.99	1.249

Table 5.4 perhaps sheds the most light on the discoveries of bench testing. A hypercritically controlled combination of material stiffness and compression ratio was required in order to maximize angular deflection amplification while reducing the propensity for snap-through or, more detrimentally, complete inability for the vane to oscillate about the 0° angle of attack equilibrium state. This is illustrated by the fact that Spring H in Table 5.4 shows a higher deflection than Spring M1 with only marginally higher compression ratio and lower material stiffness, and yet experiments showed that Spring H had a much higher propensity for violent snap-through. Snap-through is discussed in detail in Section 6.3.2.

Returning to the blocked-moment diagram shown by Figure 5.6, the effect of LNPS configurations on angular deflection amplification can be evaluated using “Spring M” with varying compression ratios. These configurations are discussed in more detail in Section 6.2.

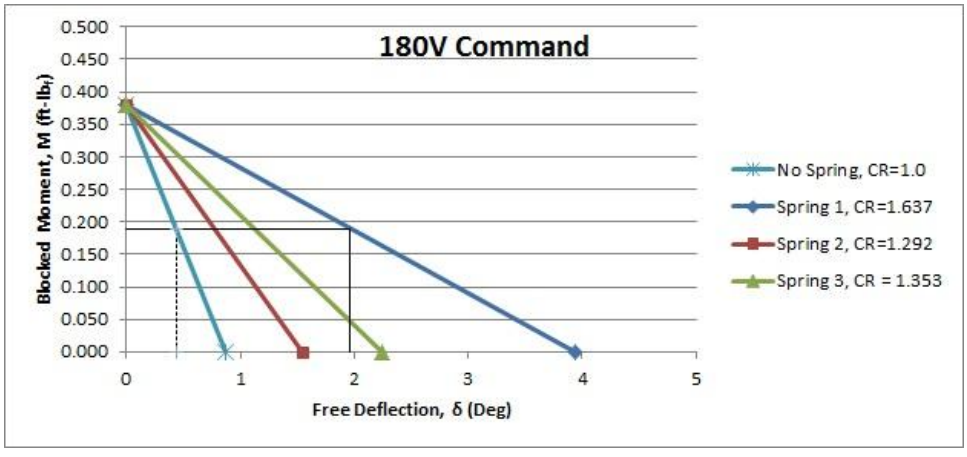

Figure 5.13 - Blocked Moment Diagram- LNPS Configurations

Notice that the design space originally defined by the unamplified configuration is increased dramatically. In fact, the difference between unamplified and "Spring 1" configurations corresponds to a 4-fold increase in total work output of the vane.

5.3 Dynamic Testing

Dynamic tests were performed both with and without LNPS configurations using two separate experimental setups. Bench testing was used primarily for determination of the quasi-static operations and effectiveness of LNPS configurations while wind tunnel testing was used for dynamic deflection at a variety of wind speeds. The correlation between the two was then performed on the basis of matching quasi-static deflection levels to ensure no anomalies in the test setup were introducing scatter into the data. Dynamic data was also compared at 0 ft/s wind speed for further verification. For this reason, only dynamic testing in the unamplified (no

LNPS) configuration will be presented here. This data is best presented in the form of a dynamic response plot as shown in Figure 5.14.

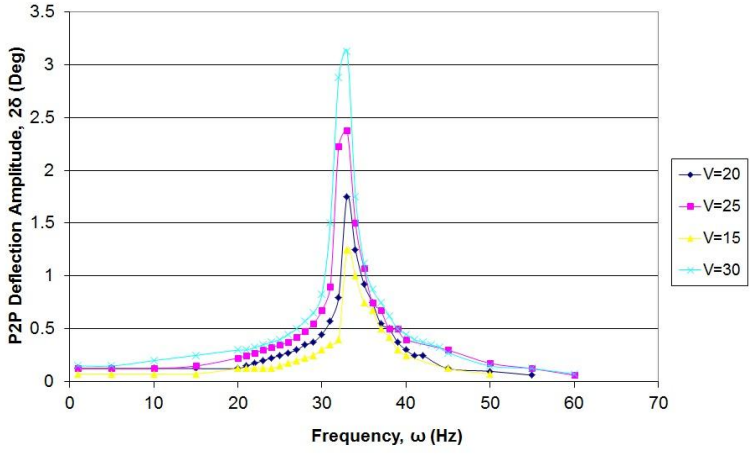

Figure 5.14 – Dynamic Response - Unamplified Configuration

The reader is asked to note the deflection level and natural frequency of the V=20 (20V activation) curve. This will be the basis for comparison in wind tunnel tests. These values are approximately 1.75° peak-to-peak and 33 Hz, respectively. It should also be recalled that 2δ from Figure 5.14 refers to the P2P angular deflection of the flutter vane.

5.4 Correlation with Theory

The results of this section agree very well with the predicted outcome as discussed in Section 3.3. It has been shown that implementation of LNPS configurations can result in nearly a 5:1 increase in total deflection output and a 4:1 increase in total work output. Section 6.3.2 discusses in more detail how these findings are applied to the equations of Section 3.3 and the results of

Section 4.3.1. Continued research has the potential to provide further insight to the marketability of this device as a flutter excitation mechanism in light aircraft classes.

6 Wind Tunnel Testing

In order to verify that the performance of the flutter vane correlates well with theory, wind tunnel testing was performed. Of particular interest to the author was the impact of aerodynamic damping on performance. It is important to determine if the flutter vane is capable of operating in a variety of flight conditions in order to accurately model the flutter characteristics of any aircraft. This section outlines the setup, procedures used and data collected during wind tunnel testing.

6.1 Experimental Setup

Wind tunnel testing of this device was carried out in the small subsonic wind tunnel at the University of Kansas in Lawrence, KS. This tunnel is capable of flow velocities up to 150 ft/s. In the interest of safety and at the request of KU faculty and support staff, flow velocities were restricted to 110 ft/s for this investigation. The dimensions of the test section are shown in Figure 6.1.

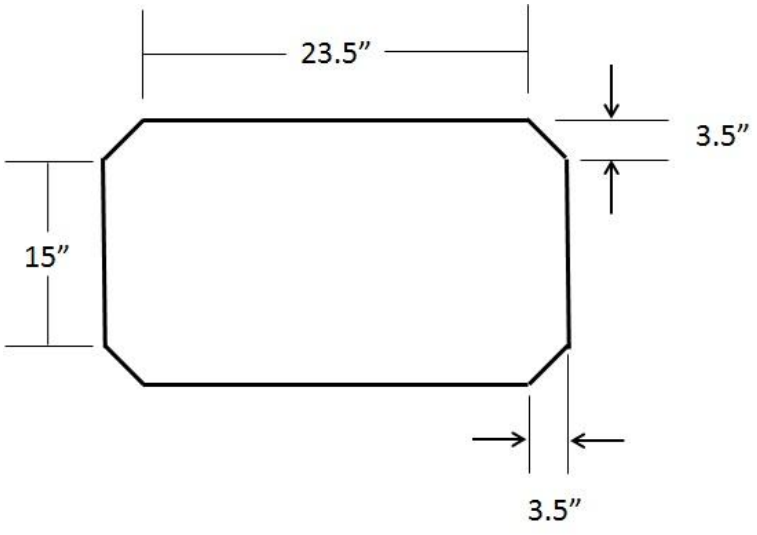

Figure 6.1 – KU Small Subsonic Wind Tunnel Test Section (Cross-Section View)

Figure 6.2 shows the test apparatus built for the small subsonic wind tunnel. The vane is cantilevered bout the pivot point shown and attached via a steel tube to the load cell. The vane extends into the wind tunnel in this manner to prevent flow disruption around the aerodynamic surface. Although this requires a custom panel (white) with a hole in it, the hole is covered with an elastic film to prevent a column of air from being sucked into the test section. Drag braces are employed to prevent force application to the load cell in a direction other than the aerodynamic lifting force on the vane.

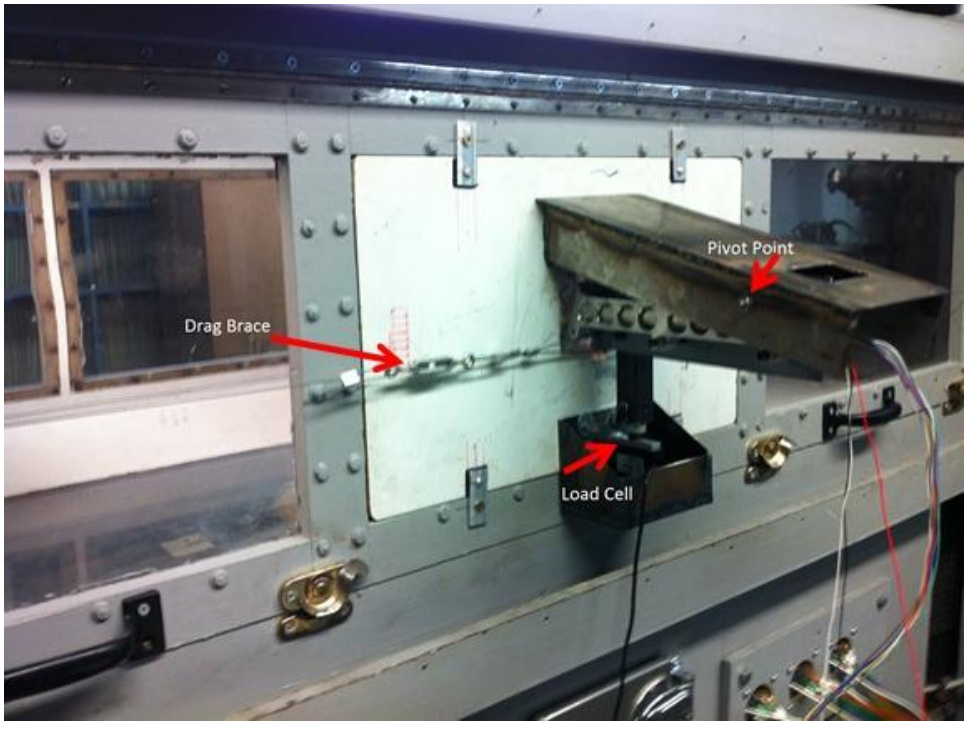

Figure 6.2 - Wind Tunnel Test Setup

Data is calibrated by placing a weight at the aerodynamic center of the vane and recording the reading on the Instron® data collection software. The calibration factor is calculated according to:

$$C.F. = \frac{Calibration\ Weight}{Instron\ Reading} \tag{72}$$

Figure 6.3 - Figure 6.4 show details of the test setup.

Figure 6.3 - Load Cell and Mount

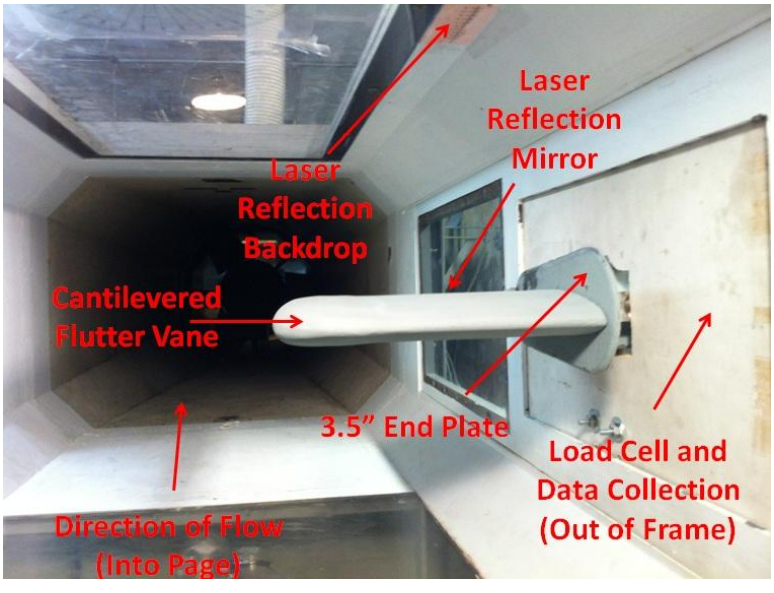

Figure 6.4 - Cantilevered Vane (Scale 1:4)

Figure 6.4 also shows the grey baseplate of the mounting hardware that will henceforth be referred to as the 3.5" end plate. The necessity for this classification will be apparent by the description of data collection outlined in Section 6.2.

6.2 Force Isolation

As is to be expected with an experimental setup involving moderately sensitive load sensing equipment, noisy data can be common. It is therefore important to carefully examine the data and extract the useful loads from the background noise.

The purpose of "force isolation" was to evaluate the changes in lift acting on the vane during quasi-static operations at various flight speeds. Quasi-static testing allows for the vane to pitch nose-up or nose-down for an extended period of time, presenting a steady load which is easily distinguishable from the background noise. Since the flutter vane is electromechanically actuated, the waveform can be tailored for many different applications. For these tests, a square waveform at 0.1 Hz actuation frequency was selected. This allows for the change in lift between peak deflection levels to be determined (see Figure 6.5).

Two sets of force isolation tests were performed on the flutter vane, using a 3.5 inch "end plate" (EP) and a 13.5 inch "end plate". This refers to the height of the root plate to which the vane is mounted. When performing wind tunnel tests, an "infinite" plate at the root of the vane causes the wing section to mimic a lift distribution as if it were mirrored across the plate. This is called a reflection plane, and it is the source of greater loads than what an elliptical lift distribution would predict for the vane with a span of 8 inches. It is important to note, however, that the fact

that this plate is not infinite and there is a slight gap between the vane and the plate will result in a less than ideal lift distribution. This is caused by root flow leakage and has been quantified by detailed wind tunnel tests[35]. Since this theoretical plate does not accurately reflect the in-flight mounting configuration of the vane, the effect of end plate height must be determined.

Before presenting the data collected for the either end plate configuration, it is necessary to discuss the parameters of investigation. The following methodology was utilized throughout the course of quasi-static wind tunnel testing:

- Determine angular deflection at various flight speeds of the flutter vane in four configurations (using method described in Section 6.1):
  - Standard (No Spring):
    - No LNPS techniques incorporated;
  - "Spring 1":
    - k_s=8.149 lb_f/in,
    - CR=1.637 (D_{SUL}=1.755");
  - "Spring 2":
    - k_s=8.149 lb_f/in,
    - CR=1.292 (D_{SUL}=1.385");
  - "Spring 3":
    - k_s=8.149 lb_f/in,
    - CR=1.353 (D_{SUL}=1.464").

- Extract change in lift load (ΔL) from Instron® data files:
  - Use MATLAB code (see APPENDIX C);
  - Determine standard deviation from noise peaks to average load.

- Compare experimental loads to theoretical prediction:
  - It should be recalled that:

$$\Delta L = \frac{1}{2}\rho V^2 S C_{L_\alpha} \Delta\alpha \tag{73}$$

Where Δα is given by the total P2P angular deflection of the flutter vane.

  - For the predicted loads, the reduced Polhamus equation established by Roskam[30] was used to determine the lift curve slope:

$$C_{L_\alpha} = \frac{C_{l_\alpha} A}{2+\sqrt{A^2+4}} \tag{74}$$

    - It should be recalled that for thin airfoils: $C_{l\alpha}=2\pi$ /rad.
    - Assuming an A=1 (no root mounted end plate) and A=2 (infinite plate), two values of lift curve slope are obtained to use when comparing the theoretical loads to experiment:
      - $C_{l\alpha}$=0.026 /deg (A=1);
      - $C_{l\alpha}$=0.043 /deg (A=2).

- Extract experimental lift curve slope ($C_{L\alpha,exp}$) from the experimental data and Equation (73).
- Interpolate to find effective aspect ratio (A_e) for this end plate configuration using Equation (74).
- Evaluate effect of increasing airspeed on flutter vane performance.

Elements of this process will be discussed in more detail in Section 6.2.1 as the data is presented.

6.2.1 Quasi-Static Testing: 3.5" End Plate

Since the majority of the data processing procedure is quite simple, this section will discuss only the extraction and interpretation of loads from the Instron®. Figure 6.5 shows a representative plot of the data extraction process. The MATLAB code first isolates a time step for evaluation which corresponds to a particular airspeed. Within that time step, smaller sections are isolated where the load is nearly constant (i.e. t=461 s to t=463 s in Figure 6.5). All of the data points in this region are then averaged to create the solid lines (green and red).

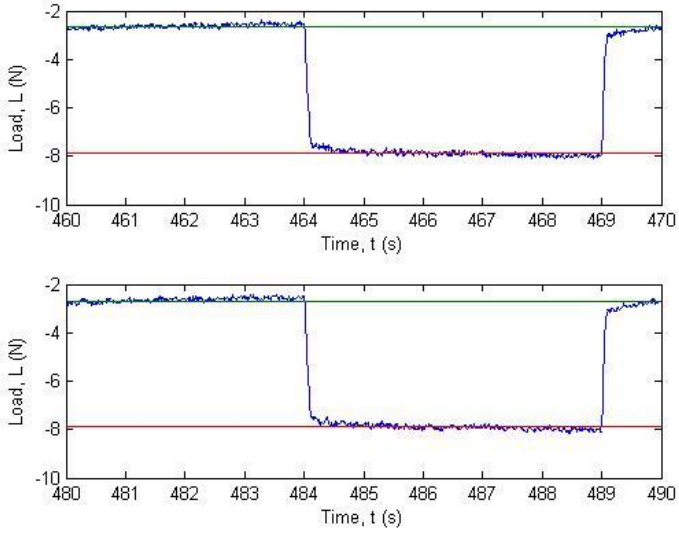

Figure 6.5 - Force Isolation Example

Once the data has been averaged and two distinct peak values can be seen, the difference between them is taken. This value corresponds to the difference between the lift force of full nose-up and nose-down attitudes (P2P deflection points). After applying the calibration factor as described in Section 6.1, a total ΔL (in lb_f) has been extracted for this configuration. The standard deviation from the solid line to the peaks of the noise is also saved. These deviations will be used to extract peak loads during dynamic testing. This is necessary as a sine waveform will be applied rather than a square wave, making data averaging much more difficult.

Having extracted a value for ΔL, Equations (73) and (74) can then be used to acquire $C_{L\alpha,exp}$ and A_e. Table 6.1 shows a representative sample of the data collected during quasi-static force isolation. APPENDIX A contains all of the data from these tests.

Table 6.1 - Quasi-Static Force Isolation Data: 3.5” End Plate

Airspeed	Freq	Force Isolation 3.5" EP: No Spring (12/8/11)											
		P2P Deflection					Predicted Load (AR=1)	Predicted Load (AR=2)	Actual Load	Peak/Average St. Dev.	Experimental Lift Curve Slope	Experimental Lift Coefficient	Reduced Frequency
		Run 1	Run 2	Run 3	Avg	St. Dev.							
ft/sec	Hz	deg	deg	deg	deg	deg	lb_f	lb_f	lb_f	lb_f	1/deg	--	--
0.0	0.1	2.0	1.8	1.8	1.87	0.12							
36.9	0.1	2.0	1.9	1.9	1.93	0.06	0.04	0.06					
52.2	0.1	2.0	1.9	1.9	1.93	0.06	0.08	0.12	0.07	0.021	0.0265	0.051	0.004
64.0	0.1	2.0	1.9	1.9	1.93	0.06	0.11	0.18	0.11	0.028	0.0263	0.051	0.003
73.9	0.1	2.0	1.9	1.9	1.93	0.06	0.15	0.24	0.16	0.037	0.0287	0.055	0.003
82.6	0.1	2.0	1.9	1.9	1.93	0.06	0.19	0.30	0.21	0.046	0.0301	0.058	0.003
90.5	0.1	2.0	2.0	1.9	1.97	0.06	0.23	0.37	0.26	0.055	0.0306	0.060	0.002
97.7	0.1	2.0	2.0	1.9	1.97	0.06	0.27	0.43	0.31	0.060	0.0313	0.062	0.002
104.5	0.1	2.0	2.0	2.0	2.00	0.00	0.31	0.50	0.36	0.068	0.0312	0.062	0.002
110.8	0.1	2.0	2.0	2.0	2.00	0.00	0.35	0.56	0.41	0.071	0.0314	0.063	0.002
									AVERAGE:	0.048	0.030		

The column entitled “Reduced Frequency” is primarily displayed for comparison with the results of dynamic testing and will be defined in Section 6.3.1. Figure 6.6 - Figure 6.8 display the information from Table 6.1 graphically. It should be recalled that 2δ refers to the P2P angular deflection of the flutter vane about the geometric quarter chord (coincident with the airfoil aerodynamic center). All quasi-static tests were performed at a frequency of 0.1 Hz as outlined in Table 6.1.

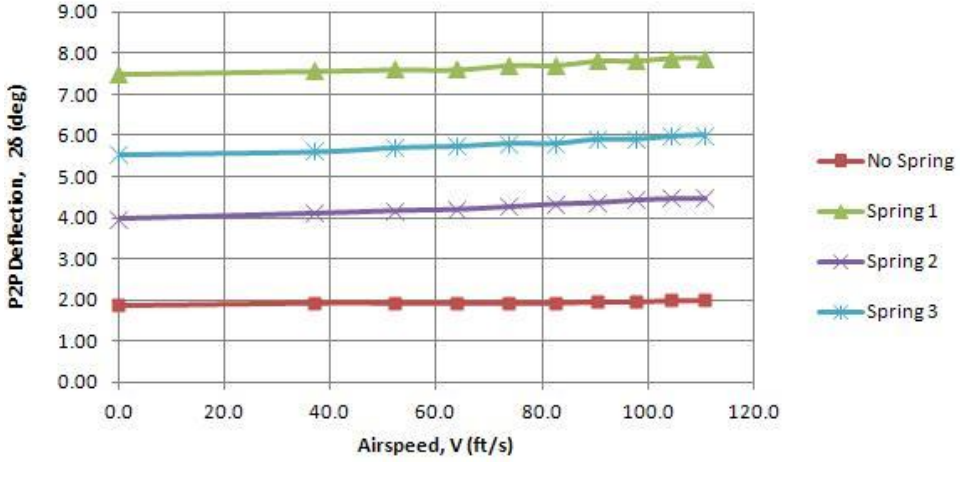

Figure 6.6 - Quasi-Static Deflections: 3.5" EP, CV= ±180V

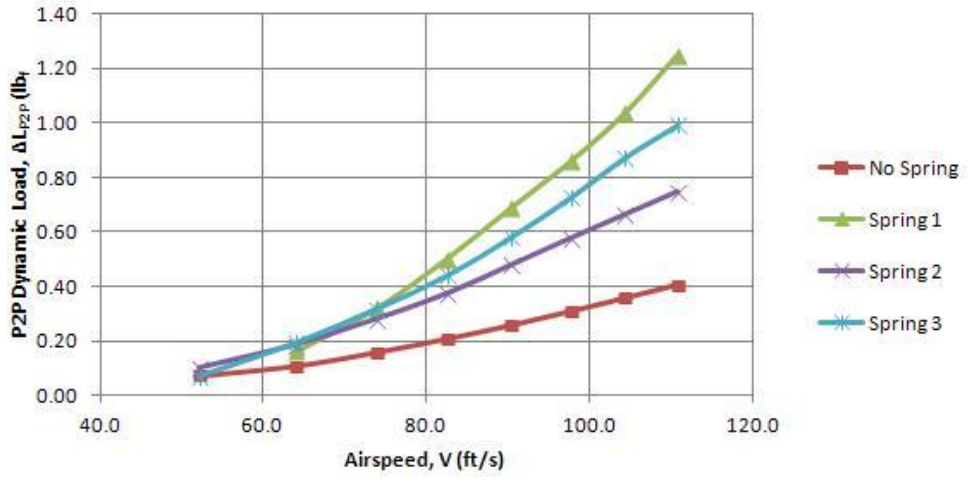

Figure 6.7 - Quasi-Static Loads: 3.5" EP, CV= ±180V

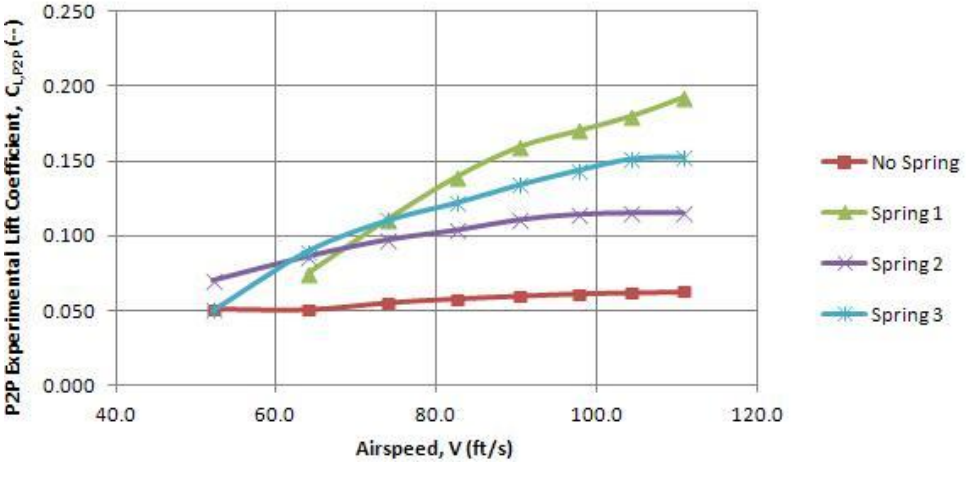

Figure 6.8 - Quasi-Static Experimental Lift Coefficient: 3.5" EP, CV= ±180V

The difference between the 3.5” end plate and the 13.5” end plate is illustrated between Figure 6.4 and Figure 6.9.

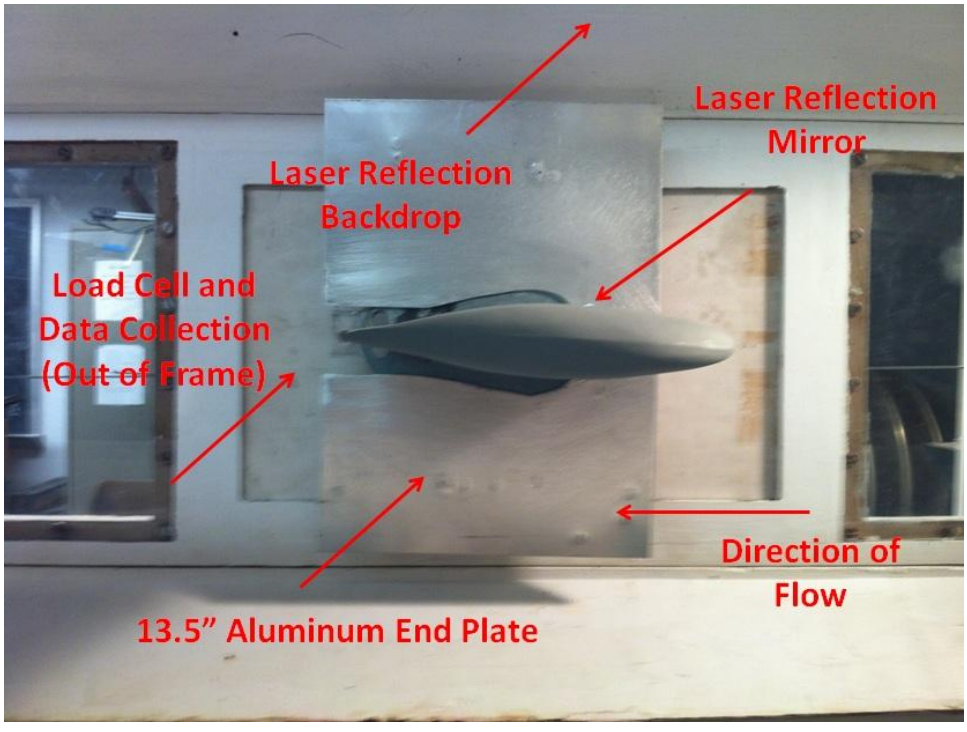

Figure 6.9 - 13.5" End Plate (Scale 1:4)

6.2.2 Quasi-Static Testing: 13.5” End Plate

As was predicted, the measured loads in quasi-static testing using the 13.5” end plate were slightly higher than that of the 3.5” end plate. This discrepancy can be attributed to the effects of root flow inhibiting the formation of a perfectly elliptical lift distribution. Table 6.2 displays the data collected for this series of tests.

Table 6.2 - Quasi-Static Force Isolation Data: 13.5" End Plate

Airspeed	Freq	Force Isolation 13.5" EP: No Spring (12/12/11)											
		P2P Deflection					Predicted Load (AR=1)	Predicted Load (AR=2)	Actual Load	Peak/Average St. Dev.	Experimental Lift Curve Slope	Experimental Lift Coefficient	Reduced Frequency
		Run 1	Run 2	Run 3	Avg	St. Dev.							
ft/sec	Hz	deg	deg	deg	deg	deg	lb_f	lb_f	lb_f	lb_f	1/deg	--	--
0.0	0.1	2.0	2.0	2.0	2.00	0.00							
36.9	0.1	2.0	2.0	2.0	2.00	0.00	0.04	0.06					
52.2	0.1	2.0	2.1	2.0	2.03	0.06	0.08	0.13	0.09	0.025	0.0301	0.061	0.004
64.0	0.1	2.0	2.1	2.0	2.03	0.06	0.12	0.19	0.14	0.025	0.0319	0.065	0.003
73.9	0.1	2.0	2.1	2.0	2.03	0.06	0.16	0.25	0.19	0.029	0.0329	0.067	0.003
82.6	0.1	2.1	2.1	2.0	2.07	0.06	0.20	0.32	0.25	0.034	0.0338	0.070	0.003
90.5	0.1	2.1	2.1	2.1	2.10	0.00	0.24	0.39	0.31	0.037	0.0345	0.072	0.002
97.7	0.1	2.1	2.1	2.1	2.10	0.00	0.29	0.46	0.37	0.046	0.0351	0.074	0.002
104.5	0.1	2.1	2.1	2.1	2.10	0.00	0.33	0.53	0.44	0.045	0.0360	0.076	0.002
110.8	0.1	2.1	2.1	2.1	2.10	0.00	0.37	0.59	0.50	0.054	0.0364	0.076	0.002
									AVERAGE:	0.037	0.034		

It should also be clear why the experimental lift coefficients have increased, as these values are derived from the actual loads acting on the flutter test vane. The complete set of data for the 13.5" end plate can also be found in APPENDIX A. The plots for this data, similar to those in Section 6.2.1, can be found in APPENDIX B.

In order to further grasp the effect of root flow on the performance of the vane, the experimental lift coefficients were inserted into Equation (74) to extract the effective aspect ratios. Figure 6.10 displays this relationship graphically.

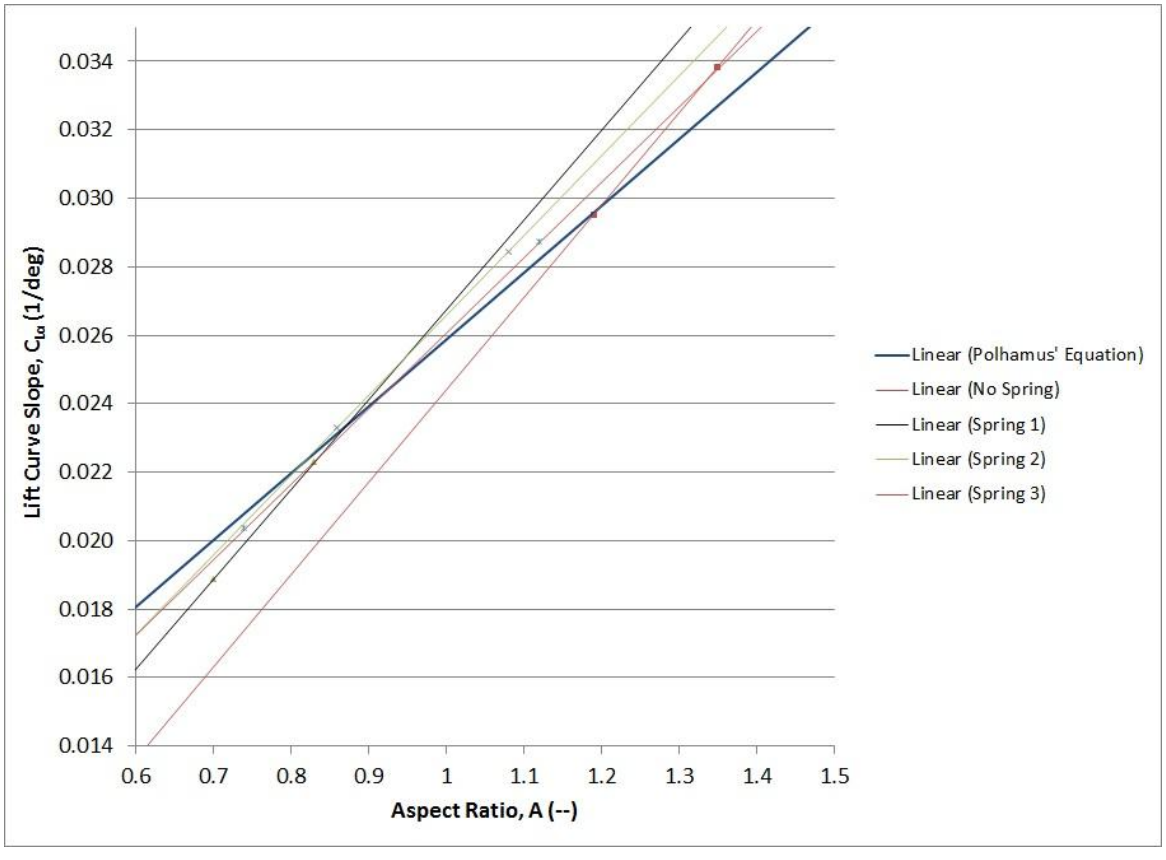

Figure 6.10 - Lift Curve Slope as a Function of Aspect Ratio

These findings indicate that the flutter test vane is operating at an effective aspect ratio of $A_e \approx 0.86$. The variations in slope of each trendline with respect to the Polhamus equation[30] are small bands (note the scaling on the y-axis of Figure 6.10).

6.3 Dynamic Testing

The dynamic tests discussed in this section will outline the performance and operating limits of the adaptive flight flutter test vane. The methods used to analyze the experimental data are identical to those presented in Section 6.2. In the interest of preserving as much undisturbed airflow over the flutter test vane as possible during the wind tunnel testing phase, all dynamic

tests were performed using the 13.5” end plate. In the interest of proving to the reader that the methods of data extraction are still valid during dynamic testing, a sample plot is presented in Figure 6.11. The MATLAB code used for processing can be found in APPENDIX C.

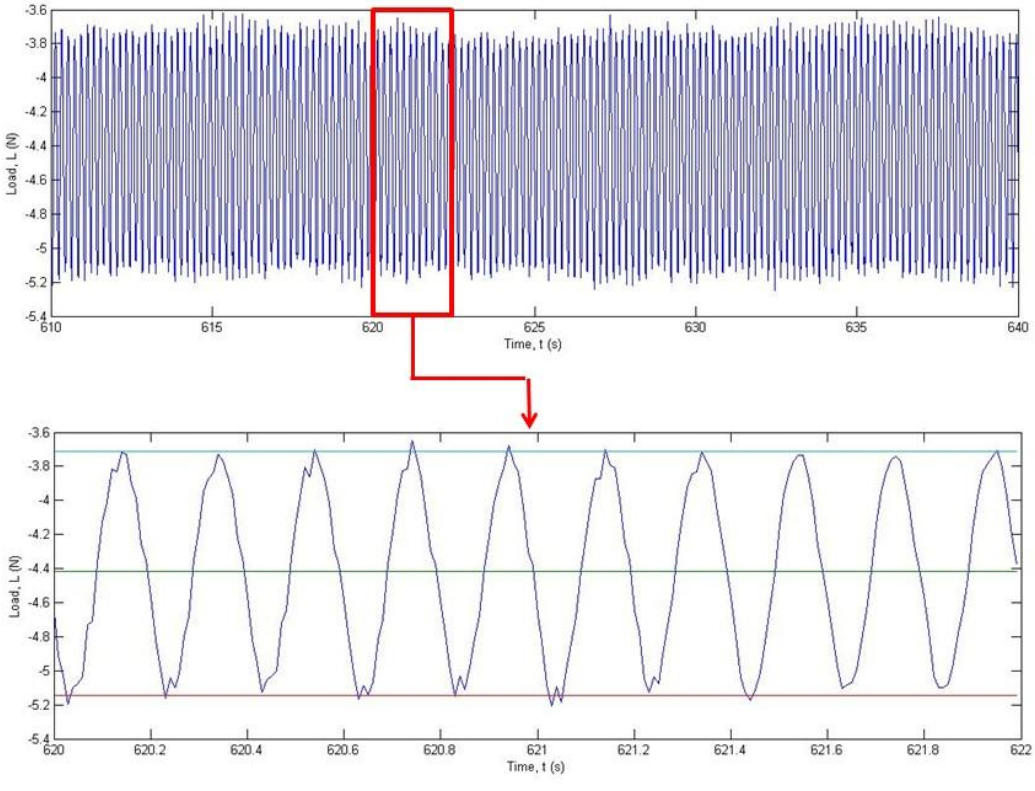

Figure 6.11 - Data Extraction Plot: ω= 5 Hz, CV= ±180V, V= 94.2 ft/s

The upper half of Figure 6.11 shows a 30 second sample of the data collected at this stage. The lower half collects 9 full cycles of oscillation and averages the peak loads to extract a total ΔL. This is then converted from N to lb_f using the calibration factor established prior to each test.

6.3.1 Optimal Operating Conditions

The purpose of this section is to outline what the author believes to be the most ideal operating conditions for the flight flutter test vane. These conditions are determined based on factors attributable mostly to the dynamics of an oscillating wing section discussed in Section 6.6. Also of extreme importance is the physical limit of the piezoelectric actuator which drives the vane. Since this device is currently the only prototype in existence, determining the fracture point of the actuator is not advisable. It is therefore highly recommended that until more in-depth testing can be performed (i.e. structural shake table tests and wind tunnel tests at greater flight velocities) this device be actuated at low command voltages during high frequency tests (>10 Hz). This section presents data at the maximum actuation voltage (CV= ±180 V) in the range of 0.7-10 Hz actuation frequency. It should be recalled that the command voltage does not account for the DC offset as discussed in Section 5.1. Section 6.3.2 will address higher actuation frequencies and the recommended command voltages for operation.

Before the data is presented, a new term must be identified: reduced frequency. This variable is a common tool used mostly in helicopter aerodynamic design to quantify the effects of dynamic stall and dynamic lift overshoot. Leishman[36] defines this variable as follows:

$$k = \frac{\omega c}{2V} \tag{75}$$

Where c is defined as the chord of the wing section, V is the flight velocity and ω is given in rad/s. Section 6.6 will discuss the significance of this term in more detail.

Table 6.3 displays the ideal operating conditions for the "No Spring" configuration. It should be recalled that this configuration implies no LNPS.

Table 6.3 - No Spring Optimal Operating Conditions: Dynamic Data

Airspeed	Freq	No Spring, CV=±180V (12/13/11)							
		P2P Deflection					Actual Load	Experimental Lift Coefficient	Reduced Frequency
		Run 1	Run 2	Run 3	Avg	St. Dev.			
ft/sec	Hz	deg	deg	deg	deg	deg	lb_f	--	--
0.0	0.7	1.8	1.9	1.9	1.87	0.06			
	3.0	1.8	1.9	2.0	1.90	0.10			
	5.0	1.8	1.9	2.0	1.90	0.10			
	7.0	1.9	2.0	2.0	1.97	0.06			
	10.0	1.7	1.8	1.8	1.77	0.06			
45.2	0.7	1.8	1.9	2.0	1.90	0.10	0.08	0.074	0.03
	3.0	1.8	2.0	2.0	1.93	0.12	0.06	0.055	0.14
	5.0	1.8	2.0	2.0	1.93	0.12	0.06	0.055	0.23
	7.0	1.9	1.9	1.9	1.90	0.00	0.05	0.046	0.32
	10.0	1.7	1.8	1.8	1.77	0.06	0.13	0.120	0.46
73.9	0.7	1.9	2.0	2.0	1.97	0.06	0.20	0.069	0.02
	3.0	1.9	2.0	2.0	1.97	0.06	0.18	0.062	0.09
	5.0	2.0	2.0	2.0	2.00	0.00	0.17	0.059	0.14
	7.0	2.0	1.9	1.9	1.93	0.06	0.12	0.042	0.20
	10.0	1.9	1.8	1.8	1.83	0.06	0.15	0.052	0.28
94.2	0.7	1.9	1.9	2.0	1.93	0.06	0.33	0.070	0.02
	3.0	2.0	1.9	2.0	1.97	0.06	0.30	0.064	0.07
	5.0	2.1	2.0	2.0	2.03	0.06	0.28	0.060	0.11
	7.0	2.0	1.9	1.9	1.93	0.06	0.22	0.047	0.16
	10.0	1.9	1.8	1.8	1.83	0.06	0.20	0.043	0.22
110.8	0.7	2.0	1.9	2.0	1.97	0.06	0.47	0.072	0.01
	3.0	2.0	2.0	2.0	2.00	0.00	0.44	0.068	0.06
	5.0	1.9	2.1	2.1	2.03	0.12	0.40	0.062	0.09
	7.0	1.9	2.0	1.9	1.93	0.06	0.32	0.049	0.13
	10.0	1.9	1.9	1.8	1.87	0.06	0.22	0.034	0.19

The data presented in Table 6.3 suggests that the maximum force output (P2P ΔL) is approximately 0.47 lb_f at a flight velocity of 110.8 ft/s and 0.7 Hz actuation frequency. In order to better visualize the results of this configuration the data is also presented graphically in Figure 6.12 - Figure 6.14.

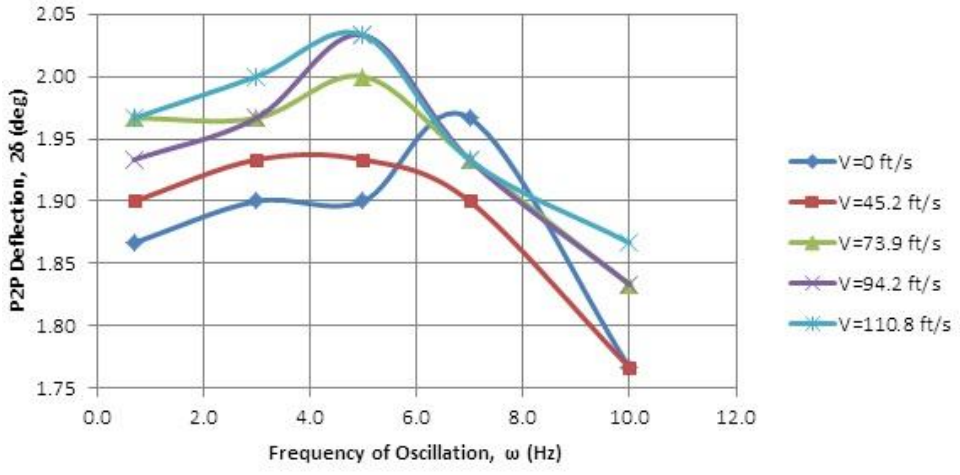

Figure 6.12 - Dynamic Response - No Spring, CV= ±180 V

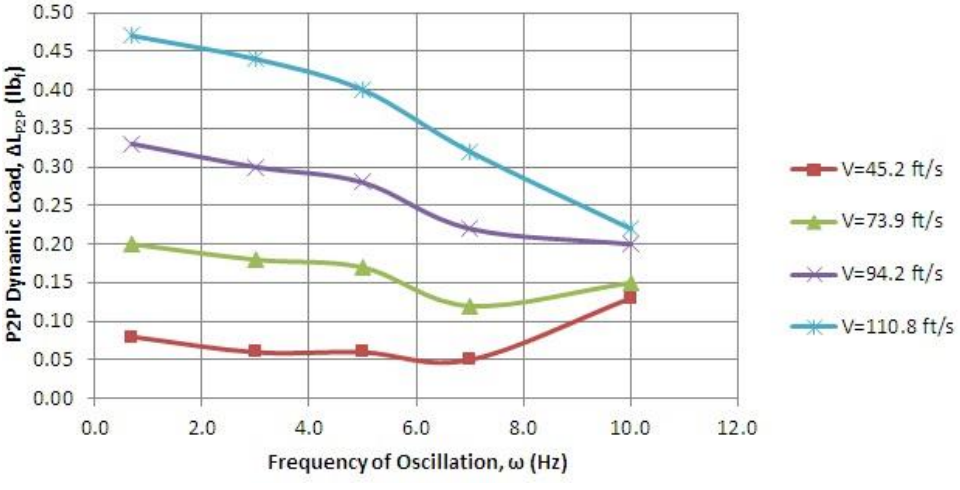

Figure 6.13 - Dynamic Loads - No Spring, CV= ±180 V

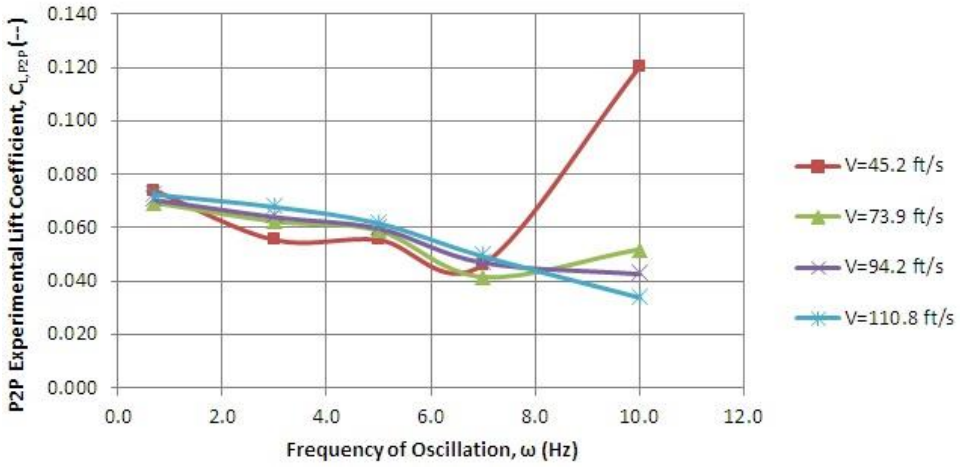

Figure 6.14 - Dynamic Lift Coefficients - No Spring, CV= ±180V

For comparison with a sample LNPS configuration the data for "Spring 2" is displayed in Table 6.4. This suggests a maximum force output of approximately 0.73 lb_f at a flight velocity of 110.8 ft/s and 0.7 Hz actuation frequency indicating a 55% increase in ΔL from baseline levels. The complete set of data tables and plots can be found in APPENDIX A and APPENDIX B, respectively.

Table 6.4 – Spring 2 Optimal Operating Conditions: Dynamic Data

Airspeed	Freq	Spring 2, CV=±180V, (CR=1.292) (12/17/11)							
		P2P Deflection					Actual Load	Experimental Lift Coefficient	Reduced Frequency
		Run 1	Run 2	Run 3	Avg	St. Dev.			
ft/sec	Hz	deg	deg	deg	deg	deg	lb_f	--	--
0.0	0.7	3.1	3.1	3.1	3.10	0.00			
	3.0	3.1	3.1	3.1	3.10	0.00			
	5.0	3.2	3.2	3.5	3.30	0.17			
	7.0	3.2	3.0	3.0	3.07	0.12			
	10.0	3.5	3.5	3.5	3.50	0.00			
45.2	0.7	3.2	3.1	3.2	3.17	0.06	0.10	0.092	0.03
	3.0	3.2	3.1	3.4	3.23	0.15	0.09	0.083	0.14
	5.0	3.3	3.2	3.6	3.37	0.21	0.08	0.074	0.23
	7.0	3.3	3.0	3.0	3.10	0.17	0.08	0.074	0.32
	10.0	3.5	3.5	3.5	3.50	0.00	0.18	0.166	0.46
73.9	0.7	3.2	3.1	3.2	3.17	0.06	0.30	0.104	0.02
	3.0	3.2	3.1	3.2	3.17	0.06	0.28	0.097	0.09
	5.0	3.3	3.2	3.5	3.33	0.15	0.24	0.083	0.14
	7.0	3.3	3.0	3.0	3.10	0.17	0.18	0.062	0.20
	10.0	3.5	3.4	3.5	3.47	0.06	0.14	0.049	0.28
94.2	0.7	3.2	3.1	3.2	3.17	0.06	0.51	0.109	0.02
	3.0	3.2	3.1	3.1	3.13	0.06	0.48	0.102	0.07
	5.0	3.4	3.3	3.5	3.40	0.10	0.45	0.096	0.11
	7.0	3.3	3.0	3.0	3.10	0.17	0.34	0.073	0.16
	10.0	3.2	3.2	3.3	3.23	0.06	0.24	0.051	0.22
110.8	0.7	3.4	3.3	3.3	3.33	0.06	0.73	0.112	0.01
	3.0	3.4	3.3	3.2	3.30	0.10	0.68	0.105	0.06
	5.0	3.5	3.4	3.5	3.47	0.06	0.64	0.099	0.09
	7.0	3.3	3.1	3.0	3.13	0.15	0.50	0.077	0.13
	10.0	3.2	3.3	3.3	3.27	0.06	0.31	0.048	0.19

6.3.2 Complete Dynamic Response Diagrams

Having identified and rigorously characterized the optimal operating conditions for the flight flutter test vane it is now necessary to present the complete operating envelope. This data is best presented in the form of dynamic response diagrams where the first natural frequency and corner frequency are clearly identifiable. Since the data presented here is in an identical format to Section 6.3.1, only a select few plots of the results are shown. The remainder of the data and plots can be found in APPENDIX A and APPENDIX B, respectively.

Figure 6.15 displays the dynamic response diagram for the "No Spring" configuration. This plot displays a natural frequency and corner frequency of $\omega_n \approx 29$ Hz and $\omega_c \approx 45$ Hz, respectively. Figure 6.16 is present for comparison and to investigate the effects of the LNPS configuration.

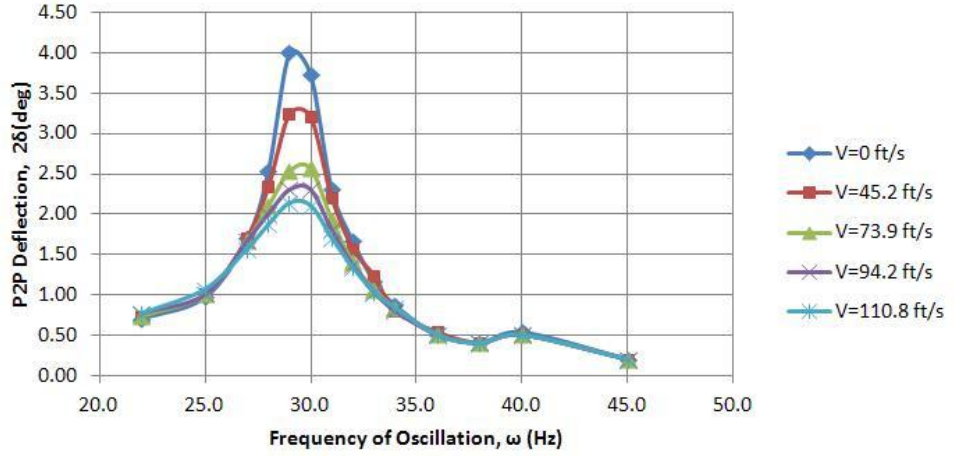

Figure 6.15 – Dynamic Response Diagram - No Spring, CV= 50V

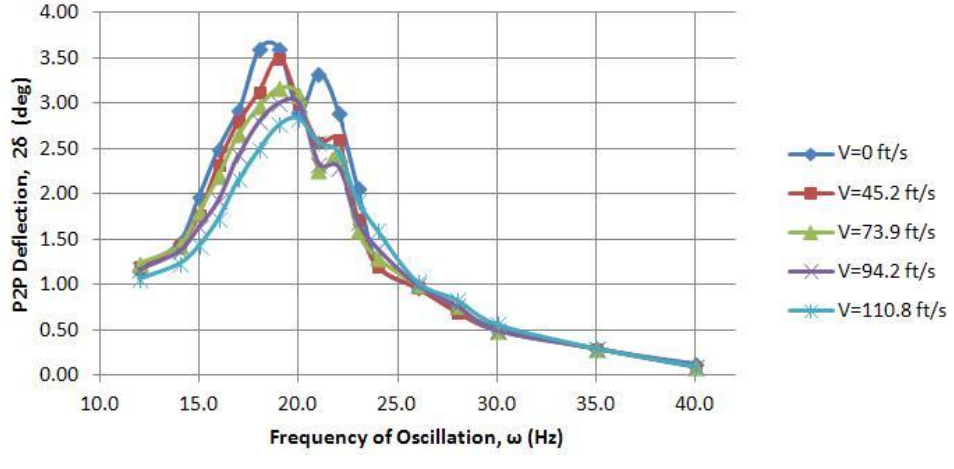

Figure 6.16 – Dynamic Response Diagram - Spring 2, CV= 50V, CR= 1.292

Since the net passive stiffness has decreased from the previous configuration, "Spring 2" reduces the natural frequency according to the following relationship:

$$\omega_n = \sqrt{\frac{k_\Theta}{I_\Theta}} \tag{76}$$

The important aspects of Figure 6.16 are the natural frequency and corner frequency, given as $\omega_n \approx 18$ Hz and $\omega_c \approx 30$ Hz. A second dynamic mode also appears at $\omega \approx 22$Hz. The nature of this mode (bending/torsion/etc.) is unknown at this point. It should be noted that these modes also appear in the "Spring 1" and "Spring 3" configurations, once again at $\omega \approx 22$Hz. The degradation in total deflection amplitude as well as the shift in natural frequency with increasing airspeed is due to aerodynamic damping due to the pitch rate of the vane. This is discussed in detail in Section 6.6.1. A summary for the dynamic testing is presented in Table 6.5.

Table 6.5 - Dynamic Summary

	Configuration			
	No Spring	Spring 1	Spring 2	Spring 3
Natural Frequency, ω_n (Hz)	30.4	15 (Stable) 24 (Unstable)	21.4	18.7
Corner Frequency, ω_c (Hz)	45	28	30	29
Maximum Load, ΔLmax (lb_f)	0.47	1.34	0.73	0.89
Ideal Operating Frequency, ω_i (Hz)	0.7	0.7	0.7	0.7
Ideal Operating Voltage, V_c (V)	±180	±180	±180	±180
Ideal Flight Velocity, V (ft/s)	110.8	110.8	110.8	110.8
Other Natural Modes, ω (Hz)	N/A	22	22	22
Net Passive Stiffness, $K_{\delta net}$ (ft lb_f/rad)	32.37	7.88 (Stable) 20.17 (Unstable)	16.05	12.25
Effective Spring Stiffness, $K_{\Theta sp}$ (ft lb_f/rad)	N/A	24.49 (Stable) 12.20 (Unstable)	16.32	20.12

Of extreme importance here is to discuss the reason that "Spring 1" has two states of operation: stable and unstable. When dealing with *very* low net passive stiffness structures, this author observed that the snap-through phenomenon[15-17] is noticeably accentuated by high frequency operations. Snap-through is illustrated using a perfect column as shown in Figure 6.17.

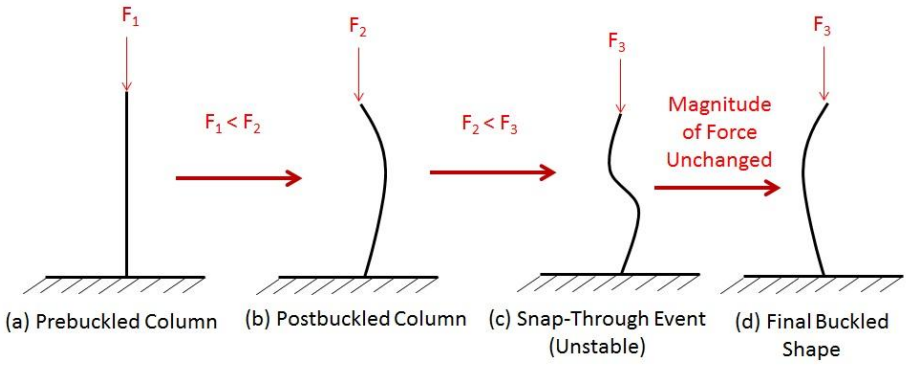

Figure 6.17 - Snap-Through of a Perfect Column

Snap-through prevents deflections through neutral, meaning that the flutter test vane oscillates permanently nose-up or nose-down at frequencies greater than 10 Hz unless the alignment of the reverse-bias spring is perfect or the command voltage is high enough to break this recovery limit. Since the "Spring 1" configuration is the highest compression ratio attainable for the vane (beyond which the command voltage can no longer be increased to overcome the recovery limit), this snap-through is nearly unavoidable as described in References 16 and 17. This is described as the "unstable" operating state. It was not advisable to push the command voltage beyond CV= ±50V in this instance. A higher voltage may have resulted in violent snap-through, risking fracture in the piezoelectric actuator. The "stable" results were achieved during bench tests in which the hypercritical alignment procedures could be performed. Adequate workspace is required for these procedures which was not available due to the size of the wind tunnel test section used for dynamic testing.

6.4 Correlation with Bench Tests

Recalling the discussion of Section 5.3, comparisons were made to determine validity of the two test setups used in this investigation. Using the bench test setup, the maximum deflection and natural frequency at 20V activation was determined to be 1.75° peak-to-peak and 33Hz, respectively. The results of wind tunnel testing, shown in Figure 6.18 at 0 ft/s wind speed and 20V activation produced 2° peak-to-peak deflection at 30.4Hz.

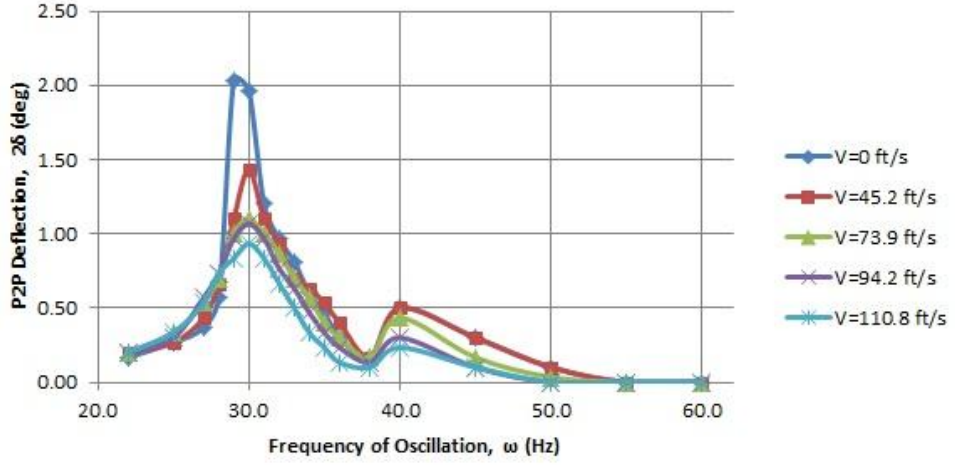

Figure 6.18 – Dynamic Response Diagram - No Spring, CV= ±20V

The discrepancy in these results is attributed to a reduction in resolution of the laser-light reflection during data collection. The closer the backdrop is placed to the reflecting mirror, the smaller the linear translations will be. Due to the constraints of the wind tunnel dimensions, this resolution issue was unavoidable. For the purpose of this investigation the data is considered reliable and repeatable.

6.5 Implications of Findings

It was determined in the course of wind tunnel testing that the flutter test vane documented here is capable of force application in a wide range of frequencies of oscillation and flight speeds. It was determined that this device, with full phase control, can be used to excite structural vibration modes in an aircraft wing or tail structure. Other current state-of-the-art excitation devices, such as the DEI vane, are fully capable of this type of excitation, albeit with far less control authority due to the lack of phase control. In combination with the findings of Section 4.3.1, it can also be shown that this device should be capable of exciting full-body modes, including "tail wag" and other fuselage modes through forces applied at the wing tips. This implies that the device is not only useful for evaluating the flutter characteristics of aircraft, but a gamut of vibrations analysis. In theory, this device could also be used for evaluating the necessity for vibration dampers in the fuselage to reduce cabin noise introduced by wing and tail oscillations. With proper integration and commercialization plans, this device could revolutionize the certification process for all classes of aircraft – not just LSAs, homebuilts, general aviation and ultralights. LNPS configurations in piezoelectric actuation also has applications in weapons technologies, UAVs, MAVs and other, smaller airborne systems.[10-12,14,29]

6.6 Dynamics of an Oscillating Wing Section

The purpose of this section is to identify the most probable causes for discrepancies between theory and experiment in the total lift force of the flight flutter test vane. There are a number of sources, most of which are well documented by Leishman[36] when discussing the aerodynamics of helicopter rotor blades.

6.6.1 Aerodynamic/Piezoelectric Damping

As was shown in Section 6.3, the effects of aerodynamic damping are anything but negligible. A parameter of importance in determining aerodynamic characteristics of aircraft is the pitch damping derivative, also referred to as the pitching moment coefficient due to pitch rate. This derivative characterizes the effect of aircraft pitching moments on the total wing lift. Rapid changes in pitch temporarily change the magnitude of the airflow relative to the wing chord, changing the net lift vector. When drawing a parallel to an oscillating wing, this term becomes increasingly important. The wing is constantly changing pitch angles, often quite rapidly. In aircraft flutter parameter prediction, the combination of pitch and plunge as shown in Figure 6.19 can dominate the dynamic characteristics of the wing. For this reason, the effects of pitch damping on the flutter test vane must be qualified.

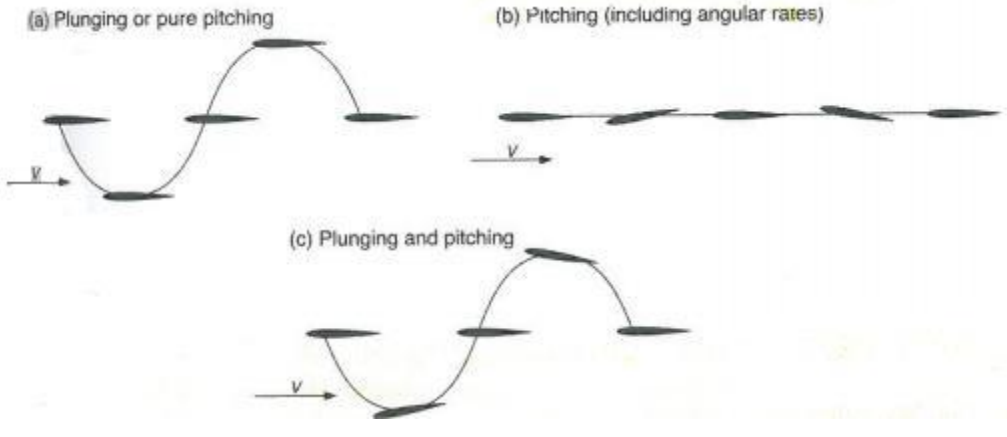

Figure 6.19 - Pitch and Plunge Motion of an Airfoil[36]

The deflections observed during dynamic testing can be normalized with quasi-static levels to extract the aerodynamic damping ratio, ζ_{aero}[31]:

$$\frac{X\omega_n^2}{f_0} = \frac{1}{\sqrt{(1-r^2)^2+(2\zeta r)^2}} \tag{77}$$

The ratio on the left hand side of Equation (77) is the normalized deflection. The frequency ratio, r, is given by:

$$r = \frac{\omega}{\omega_n} \tag{78}$$

By extracting the loads at zero airspeed, the structural damping ratio, ζ_{vane} can be obtained. Note then that the damping ratios extracted from "live airspeed" tests is, in fact, the total damping ratio, ζ_{tot}. Subtracting ζ_{vane} from ζ_{tot} will result in the aerodynamic damping ratio, ζ_{aero}. Having established a natural frequency and rotational mass moment of inertia from bench testing, the structural and aerodynamic damping coefficients, c can then be extracted[31]:

$$c = 2I_\Theta \omega_n \zeta \tag{79}$$

It should be noted here that c_{aero} is synonymous with the pitch damping derivative, C_{Mq}, as described by Roskam[30]. Table 6.6 shows a representative sample of these calculations. The complete set of tables can be found in APPENDIX A.

Table 6.6 - Aerodynamic Damping Sample

Airspeed	Freq	No Spring, CV=±20V (12/19/11)											
		P2P Deflection					Normalized Deflection	Frequency Ratio	Reduced Frequency	Total Damping Ratio	Aerodynamic Damping Ratio	Structural Damping Coefficient	Aerodynamic Damping Coefficient
		Run 1	Run 2	Run 3	Avg	St. Dev.	Avg	r		ζ_{tot}	ζ_{air}	c_{vane}	c_{aero} (C_{Mq})
ft/sec	Hz	deg	deg	deg	deg	deg	--	--	--	--	--	(ft lb_f)/(rad/s)	(ft lb_f)/(rad/s)
0.0	22.0	0.2	0.2	0.1	0.17	0.06	1.00	0.72		0.608		0.214	
	25.0	0.2	0.3	0.3	0.27	0.06	1.60	0.82		0.325		0.114	
	27.0	0.3	0.4	0.4	0.37	0.06	2.20	0.89		0.227		0.080	
	28.0	0.5	0.6	0.6	0.57	0.06	3.40	0.92		0.137		0.048	
	29.0	2.0	2.1	2.0	2.03	0.06	12.20	0.95		0.019		0.007	
	30.0	1.9	2.0	2.0	1.97	0.06	11.80	0.99		0.041		0.014	
	31.0	1.2	1.2	1.2	1.20	0.00	7.20	1.02		0.065		0.023	
	32.0	1.0	1.0	0.9	0.97	0.06	5.80	1.05		0.064		0.022	
	33.0	0.8	0.9	0.7	0.81	0.09	4.86	1.09		0.047		0.017	
	34.0	0.6	0.6	0.6	0.60	0.00	3.60	1.12		0.053		0.019	
	35.0	0.5	0.5	0.4	0.47	0.06	2.80	1.15		0.064		0.022	
	36.0	0.3	0.3	0.3	0.30	0.00	1.80	1.18		0.162		0.057	
	38.0	0.2	0.2	0.1	0.17	0.06	1.00	1.25		0.331		0.116	
45.2	22.0	0.3	0.2	0.1	0.20	0.10	1.00	0.72	1.02	0.608	0.0000	0.214	0.000
	25.0	0.3	0.3	0.2	0.27	0.06	1.33	0.82	1.16	0.411	0.0863	0.145	0.030
	27.0	0.4	0.5	0.4	0.43	0.06	2.17	0.89	1.25	0.231	0.0044	0.081	0.002
	28.0	0.7	0.7	0.6	0.67	0.06	3.33	0.92	1.30	0.141	0.0037	0.049	0.001
	29.0	1.0	1.2	1.1	1.10	0.10	5.50	0.95	1.34	0.083	0.0633	0.029	0.022
	30.0	1.3	1.5	1.5	1.43	0.12	7.17	0.99	1.39	0.069	0.0286	0.024	0.010
	31.0	1.1	1.1	1.1	1.10	0.00	5.50	1.02	1.44	0.087	0.0217	0.031	0.008
	32.0	1.0	0.9	0.9	0.93	0.06	4.67	1.05	1.48	0.088	0.0241	0.031	0.008
	33.0	0.7	0.7	0.7	0.70	0.00	3.50	1.09	1.53	0.103	0.0556	0.036	0.020
	34.0	0.7	0.6	0.6	0.63	0.06	3.17	1.12	1.57	0.086	0.0324	0.030	0.011
	35.0	0.6	0.5	0.5	0.53	0.06	2.67	1.15	1.62	0.081	0.0170	0.028	0.006
	36.0	0.4	0.4	0.4	0.40	0.00	2.00	1.18	1.67	0.125	-0.0364	0.044	-0.013
	38.0	0.2	0.2	0.1	0.17	0.06	0.83	1.25	1.76	0.424	0.0933	0.149	0.033
73.9	22.0	0.3	0.2	0.1	0.20	0.10	1.00	0.72	0.62	0.608	0.0000	0.214	0.000
	25.0	0.4	0.3	0.3	0.33	0.06	1.67	0.82	0.71	0.307	-0.0179	0.108	-0.006
	27.0	0.6	0.5	0.5	0.53	0.06	2.67	0.89	0.77	0.174	-0.0521	0.061	-0.018
	28.0	0.8	0.7	0.6	0.70	0.10	3.50	0.92	0.79	0.131	-0.0054	0.046	-0.002
	29.0	1.0	1.0	1.0	1.00	0.00	5.00	0.95	0.82	0.094	0.0742	0.033	0.026
	30.0	1.1	1.1	1.1	1.10	0.00	5.50	0.99	0.85	0.091	0.0503	0.032	0.018
	31.0	1.0	1.0	1.0	1.00	0.00	5.00	1.02	0.88	0.096	0.0309	0.034	0.011
	32.0	0.9	0.9	0.8	0.87	0.06	4.33	1.05	0.91	0.097	0.0330	0.034	0.012
	33.0	0.8	0.7	0.6	0.70	0.10	3.50	1.09	0.94	0.103	0.0556	0.036	0.020
	34.0	0.6	0.6	0.5	0.57	0.06	2.83	1.12	0.96	0.111	0.0577	0.039	0.020
	35.0	0.4	0.4	0.4	0.40	0.00	2.00	1.15	0.99	0.165	0.1010	0.058	0.036
	36.0	0.3	0.3	0.3	0.30	0.00	1.50	1.18	1.02	0.224	0.0627	0.079	0.022
	38.0	0.2	0.2	0.1	0.17	0.06	0.83	1.25	1.08	0.424	0.0933	0.149	0.033
94.2	22.0	0.2	0.2	0.2	0.20	0.00	1.00	0.72	0.49	0.608	0.0000	0.214	0.000
	25.0	0.3	0.3	0.3	0.30	0.00	1.50	0.82	0.56	0.354	0.0293	0.125	0.010
	27.0	0.7	0.5	0.5	0.57	0.12	2.83	0.89	0.60	0.159	-0.0674	0.056	-0.024
	28.0	0.8	0.8	0.6	0.73	0.12	3.67	0.92	0.62	0.123	-0.0138	0.043	-0.005
	29.0	1.0	1.0	0.9	0.97	0.06	4.83	0.95	0.64	0.098	0.0782	0.034	0.027
	30.0	1.1	1.1	1.0	1.07	0.06	5.33	0.99	0.67	0.094	0.0532	0.033	0.019
	31.0	1.0	1.0	0.9	0.97	0.06	4.83	1.02	0.69	0.100	0.0343	0.035	0.012
	32.0	0.8	0.8	0.7	0.77	0.06	3.83	1.05	0.71	0.113	0.0490	0.040	0.017
	33.0	0.7	0.6	0.6	0.63	0.06	3.17	1.09	0.73	0.120	0.0728	0.042	0.026
	34.0	0.5	0.4	0.5	0.47	0.06	2.33	1.12	0.76	0.155	0.1020	0.055	0.036
	35.0	0.4	0.3	0.3	0.33	0.06	1.67	1.15	0.78	0.219	0.1551	0.077	0.055
	36.0	0.3	0.2	0.2	0.23	0.06	1.17	1.18	0.80	0.320	0.1578	0.112	0.055
	38.0	0.2	0.1	0.1	0.13	0.06	0.67	1.25	0.85	0.556	0.2255	0.195	0.079
110.8	22.0	0.2	0.2	0.2	0.20	0.00	1.00	0.72	0.42	0.608	0.0000	0.214	0.000
	25.0	0.4	0.3	0.3	0.33	0.06	1.67	0.82	0.47	0.307	-0.0179	0.108	-0.006
	27.0	0.6	0.5	0.5	0.53	0.06	2.67	0.89	0.51	0.174	-0.0521	0.061	-0.018
	28.0	0.8	0.7	0.7	0.73	0.06	3.67	0.92	0.53	0.123	-0.0138	0.043	-0.005
	29.0	0.9	0.8	0.8	0.83	0.06	4.17	0.95	0.55	0.117	0.0972	0.041	0.034
	30.0	1.0	0.9	0.9	0.93	0.06	4.67	0.99	0.57	0.108	0.0669	0.038	0.024
	31.0	0.9	0.9	0.7	0.83	0.12	4.17	1.02	0.59	0.116	0.0508	0.041	0.018
	32.0	0.7	0.7	0.6	0.67	0.06	3.33	1.05	0.60	0.133	0.0691	0.047	0.024
	33.0	0.5	0.5	0.5	0.50	0.00	2.50	1.09	0.62	0.165	0.1177	0.058	0.041
	34.0	0.4	0.3	0.3	0.33	0.06	1.67	1.12	0.64	0.244	0.1903	0.086	0.067
	35.0	0.3	0.2	0.2	0.23	0.06	1.17	1.15	0.66	0.344	0.2806	0.121	0.099
	36.0	0.2	0.1	0.1	0.13	0.06	0.67	1.18	0.68	0.610	0.4484	0.214	0.158
	38.0	0.1	0.1	0.1	0.10	0.00	0.50	1.25	0.72	0.768	0.4370	0.270	0.154

Notice that not only are the pitch damping derivatives small, but some of them are negative! This is not implying some bizarre scenario in which the aerodynamics of the wing have changed. This is simply showing that the effects of aerodynamic damping are so small in some places that the equations used to quantify them no longer apply. These equations are perfectly valid, however, at the natural frequency of the vane where the deflections are highest and the frequency ratio is 1. The variations in aerodynamic damping ratio with respect to airspeed and reduced frequency, highlighted in Table 6.6, are displayed in Figure 6.20 and Figure 6.21.

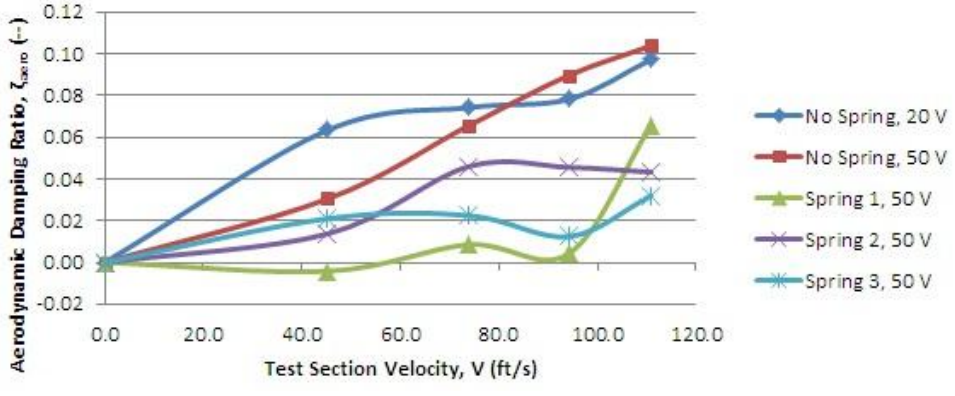

Figure 6.20 - Effect of Airspeed on Aerodynamic Damping Ratio

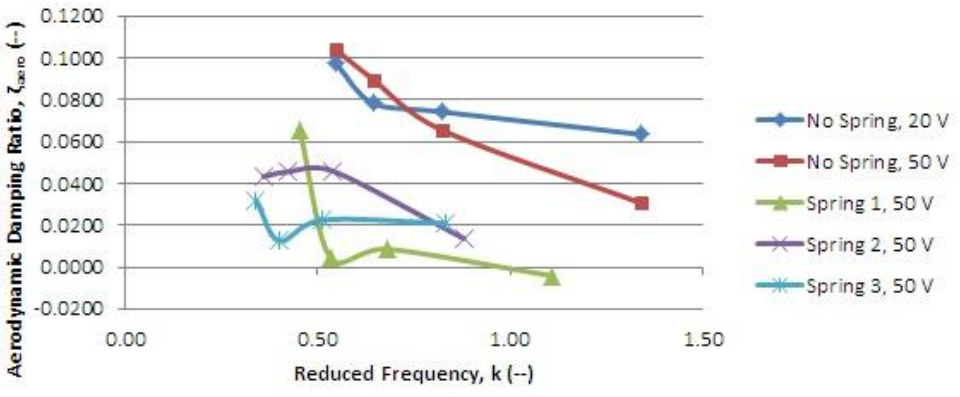

Figure 6.21 - Effect of Reduced Frequency on Aerodynamic Damping Ratio

Figure 6.20 displays an interesting phenomenon that brought about a striking revelation at this point in the evaluation stage of the adaptive flight flutter test vane. Spring 1 is shown with two different command voltages, ±20 V and ± 50 V. Both curves show the anticipated increase in aerodynamic damping with airspeed; however, these curves are of second order and actually intersect one another. Looking back on the data of Table 6.6, it can be seen that the structural damping inherent in the piezoelectric actuator not only fluctuates with actuation frequency, it dominates the dynamic response of the vane even at the natural frequency of oscillation. This phenomenon is shown once again when looking at the effects of reduced frequency in Figure 6.21. Returning to Table 6.6, this phenomenon provides another explanation for the occurrence of negative aerodynamic damping ratios. Also note the magnitude of the reduced frequencies in Figure 6.21. This vane is operating *well* beyond the realm of even helicopter rotors[31]. To the author's knowledge, there is no data for comparison here and the effects of dynamic stall and dynamic lift overshoot may be completely dominating the aerodynamic characteristics of the vane. These effects will be discussed in the coming sections.

6.6.2 Dynamic Lift Overshoot

Throughout this document the author has referred numerous times to reduced frequency, k, and its effects on the dynamics of an oscillating wing section. In order to better understand these effects, one must look into the aerodynamic characteristics of helicopter rotors as described by Leishman[36]. Reduced frequency is a common method for describing the hysteresis loop in the lift curve of aerodynamic structures, also known as dynamic lift overshoot, and is the primary cause for variations in lift forces observed in oscillating wings. The pitching motion of the wing section results in the formation of a large vortex on the upper surface which temporarily creates a favorable pressure distribution and increases the effective C_{lmax}[37]. This favorable distribution is maintained as the vortex travels along the chord of the airfoil until it reaches the trailing edge and collapses. Upon collapse, the flow over the airfoil is massively disturbed and results in a net loss in C_{lmax} until the flow reattaches. This is known as dynamic stall. This propagating vortex also induces a nontrivial increase in pitching moment. The effects of dynamic lift overshoot can sometimes result in lift overshoots between 50% and 100% higher than the static value[36]. It should be noted, however, that the effects of dynamic lift overshoot are most commonly only quantified in the range of $0 \leq k \leq 0.4$, where $k \leq 0.05$ is considered quasi-steady and $k \geq 0.2$ is highly unsteady. Figure 6.22 and Figure 6.23 show these effects graphically.

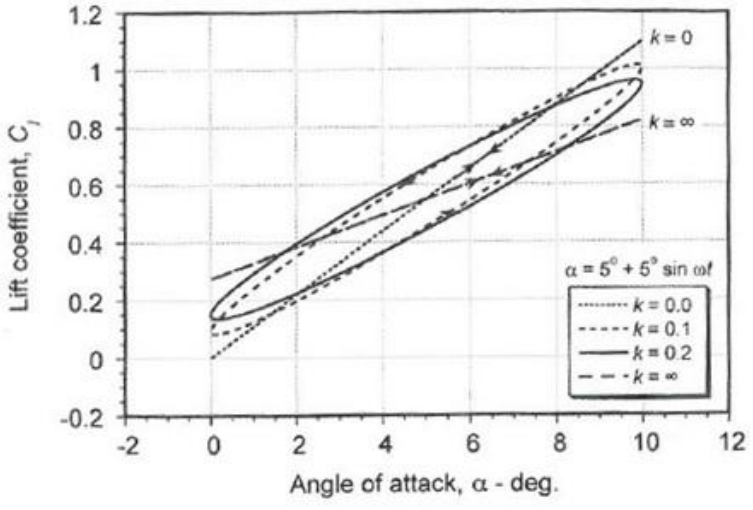

Figure 6.22 – Effect of Dynamic Lift Overshoot on Sectional Lift Coefficient[36]

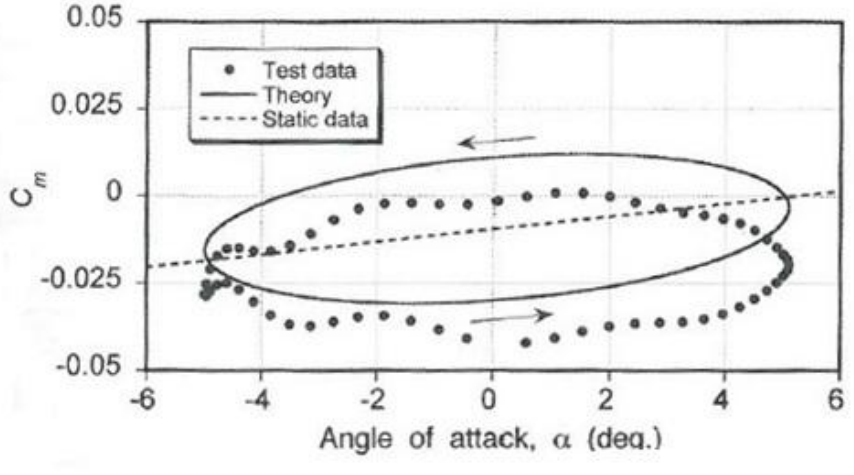

Figure 6.23 - Effect of Dynamic Lift Overshoot on Sectional Pitching Moment, k=0.125[36]

Clearly these effects cannot be ignored for the adaptive flutter test vane. Recalling that this vane operates with reduced frequencies as high as 1.85 or even 2.78 (at corner frequencies), it should

be quite clear as to why the experimental lift coefficients extracted from wind tunnel testing are quite different than those predicted by the Polhamus equation[30].

6.6.3 Dynamic Stall

Leishman also describes the dynamic stall phenomenon very well in his book[36]. Figure 6.24 and Figure 6.25 show schlieren imagery and artistic interpretations of dynamic stall.

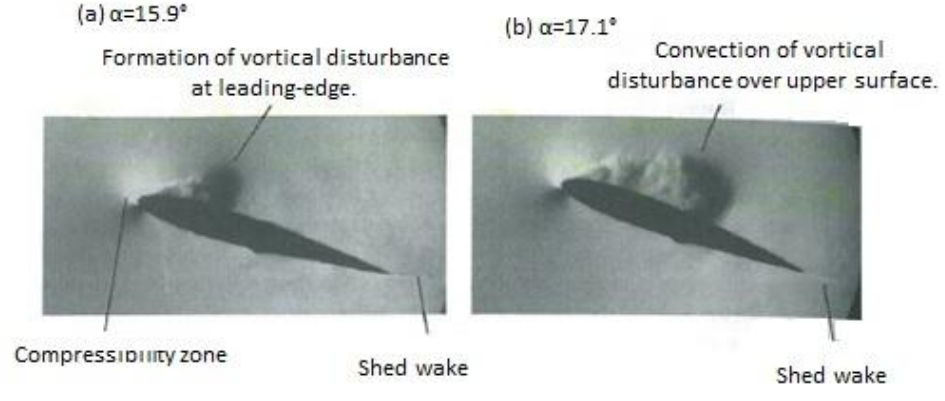

Figure 6.24 - Visualization of Dynamic Stall using Schlieren Photography[36]

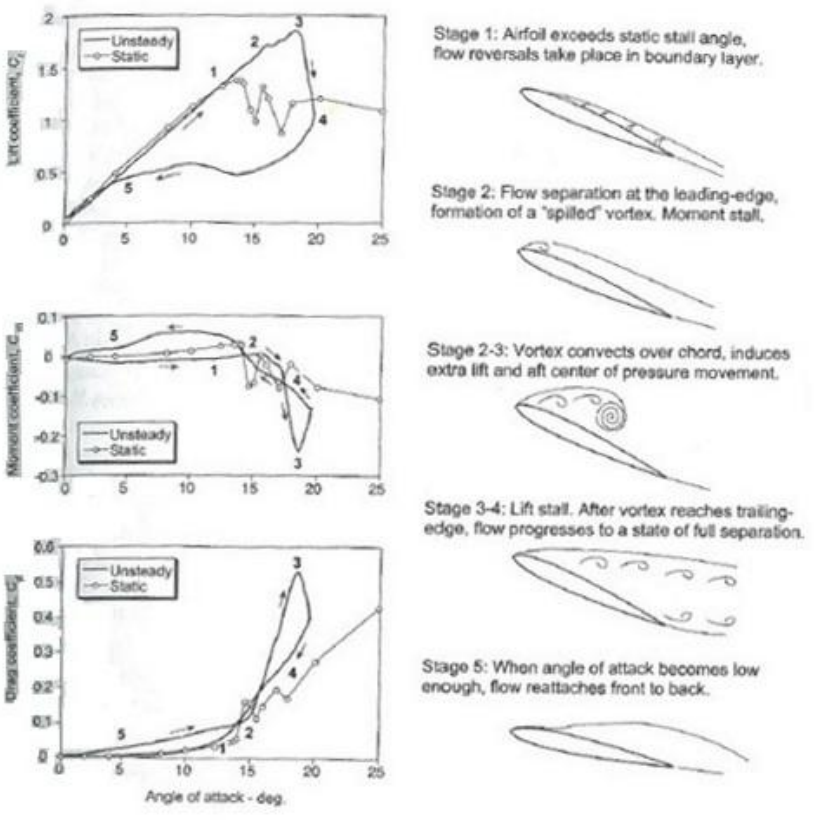

Figure 6.25 - Schematic Showing the Stages of Dynamic Stall[36]

The lag associated with flow reattachment at high reduced frequencies can sometimes result in extreme degradation of airfoil performance. In the case of the adaptive flight flutter test vane, operations near the corner frequencies almost surely do not allow sufficient time for the flow to reattach, rendering the device all but useless.

6.7 Correction Factors

In order to eliminate any uncertainty in the data that would originate from the design and or manufacturing flaws of the wind tunnel itself, a series of correction factors were established according Rae and Pope[38]. The following sections discuss the various sources of experimental error and their impact on the data presented previously.

6.7.1 Solid Blocking

Solid blocking effects originate from the introduction of a test article into the wind tunnel. The test article reduces the control volume through which the airflow can pass. According to Bernoulli, this results in an increase in local freestream velocity in the vicinity of the test article. Since the pitot-static system captures freestream velocity (typically at the entrance to the wind tunnel test section) this velocity change is not recorded and must therefore be independently evaluated. Rae and Pope[38] outline the follow procedure for establishing a solid blocking correction factor:

$$\varepsilon_{swb} = \frac{\Delta V}{V_u} = \frac{K_1 \tau_1 V_{wing}}{C^{3/2}} \tag{80}$$

From Rae and Pope[38], let K_1=1.057, τ_1=0.83. From the test article geometry V_{wing}=62.28 in^3, C=500.5 in^2 are established such that:

$$\varepsilon_{swb} = \frac{(1.057)(0.83)(62.28\ in^3)}{(500.5\ in^2)^{3/2}} = 0.00488 \tag{81}$$

This correction factor will be combined with the effect of wake blocking in the next section to evaluate the total velocity adjustment.

6.7.2 Wake Blocking

As the airflow passes over a body, the fluid is disturbed and often propagates in an unpredictable manner as it transitions back into an unobstructed volume of air. This wake aft of the solid body will therefore exhibit a lower velocity component in the direction of the freestream. According to the law of conservation of momentum, there must then be a local increase in velocity outside the wake. This velocity adjustment is calculated as follows[38]:

$$\varepsilon_{wb} = \frac{\Delta V}{V_u} = \frac{1}{4}\left(\frac{S}{C}\right) C_{D_u} \tag{82}$$

From the geometry of the test article, let: S=64 in^2, C=500.5 in^2, $C_{D,u}$=0.005 such that

$$\varepsilon_{wb} = \frac{1}{4}\left(\frac{64\ in^2}{500.5\ in^2}\right)(0.005) = 0.00016 \tag{83}$$

When combined with the effects of solid blocking, a total velocity correction can be established[38]:

$$\varepsilon = \varepsilon_{swb} + \varepsilon_{wb} = 0.00488 + 0.00016 = 0.00504 \tag{84}$$

$$\varepsilon = \frac{\Delta V}{V_u} = \frac{V_\infty - V_u}{V_u}\ ;\ V_\infty = V_u(1+\varepsilon) = 1.00504 V_u \tag{85}$$

A change in velocity of 0.504% is, for the purposes of this investigation, considered to be negligible and is therefore excluded from data post-processing.

6.7.3 3D Streamline Curvature

The effects of streamline curvature develop when the airfoil is not bounded by the walls of the tunnel or end plates at the root and tip. By not bounding the test article, the jet is free to diverge downstream of the airfoil[38]. This curvature in the airflow induces a drag increment that reduces the effective angle of attack of the airfoil. Since this investigation is based entirely on change in lift due to the oscillating vane, this is an important correction factor to evaluate. Rae and Pope[38] suggest the following method for evaluating the effects of 3D streamline curvature:

$$\Delta C_{L_{sc}} = -\Delta\alpha_{sc} C_{L_\alpha} = -\tau_2 \delta \left(\frac{S}{C}\right) C_{L_\alpha} \alpha a. \tag{86}$$

From Rae and Pope[38], let τ_2=0.177, δ=0.113, a=2π /rad. From the geometry of the test article, C=500.5 in^2, S=64 in^2 are obtained. Also related to the geometry of the test article and found according to the Polhamus equation established in Roskam[30], $C_{L,\alpha}$=0.042 /deg (allow AR=2) is obtained such that:

$$\Delta C_{L_{sc}} = -(0.117)(0.113)\left(\frac{64\ in^2}{500.5\ in^2}\right)\left(0.042\,\frac{1}{deg}\right)(2\pi)\alpha = -0.000675\alpha \tag{87}$$

If the maximum angle of attack is set at 10 deg (geometrically restricted by the internal structure of the vane), this lift coefficient correction is approximately -0.675%. For the purposes of this investigation this will be considered a negligible change and will therefore be excluded from data post-processing.

6.7.4 Downwash Corrections

The existence of a jet which is larger than the total span of the airfoil (even in the presence of end plates) creates a downwash field at the trailing edge of the test article. As is true with streamline curvature, this induces a velocity increment normal to the freestream and a change in the effective angle of attack of the airfoil. Rae and Pope[38] characterize this effect with the following correction factor:

$$\alpha = \alpha_u + \delta\left(\frac{S}{C}\right) C_L(57.3) = \alpha_u\left[1 + \delta\left(\frac{S}{C}\right) C_{L_\alpha}(57.3)\right] \tag{88}$$

Recalling that δ=0.113, S=64 in^2, C=500.5 in^2, $C_{L,\alpha}$=0.042 /deg:

$$\alpha = \alpha_u\left[1 + 0.113\left(\frac{64\ in^2}{500.5\ in^2}\right)\left(0.042\frac{1}{\text{deg}}\right)(57.3)\right] = 1.035\alpha_u \tag{89}$$

When the maximum angle of attack is input into Equation (89), a corrected AoA of 10.35 deg is established. Since the data collected during tunnel testing is sensitive to changes in AoA on the

order of 0.1 deg, the downwash correction cannot be ignored. This correction is therefore built-in to the data presented previously.

6.7.5 Other Corrections

Although no correction factors are established here, there are a few more parameters worth discussing with regards to the experimental apparatus and wind tunnel operation. In particular, one must be certain that concerns regarding 3D buoyancy are dispelled. This phenomenon is most commonly observed in an experimental apparatus where the test article is very large or placed in close proximity to the walls of the test section. In these cases, the growth of the boundary layer induces a velocity component perpendicular to the freestream. If there is insufficient spacing between this boundary layer and the test article the effects of buoyancy will be apparent in the data. Since the adaptive flutter vane was centered vertically in the test section of the wind tunnel and an end plate placed at the root (where the spacing is significantly lower), this effect can be confidently neglected.

Also of concern when establishing the experimental apparatus are: tare, interference and drag coupling[38,39]. As can be seen by the figures presented in Section 6.1, there is minimal risk of the mounting hardware interfering with the flow over the airfoil. This risk is minimized even further by the presence of the root-mounted end plate. The drag braces (also shown in Figure 6.2) negate the effects of drag coupling as seen by the load cell. Since these drag forces are neglected, there can exist no effects of tare as described by Rae and Pope[38].

Perhaps more difficult to quantify is the tendency for wind tunnel surge. Since these experiments look at forces on an oscillating aerodynamic body, it is important to dispel concerns of a regular surge creating a "beat" in the data stream. A rapid change in airspeed would create a brief divergence from the "normal" force readings during data collection. It should be clear, however, that since the flutter vane was operating in a wide range of frequencies, any indication of surge, regular or irregular, would be recognized at some point as a spike in the data. Repeated tests at consistent airspeeds and operating frequencies show no noticeable effects of tunnel surge. The author is not suggesting that this implies that tunnel surge is completely negated; these findings simply indicate that, if surge exists, it is negligible with respect to the scope of this investigation.

Finally, the effect of the turbulence sphere[38,39] on the Reynolds number must be investigated. The turbulence sphere addresses the amount of flow disruption due to unchangeable factors such as tunnel wall vibrations. This is referred to as the turbulence sphere because the methods of testing require measuring the drag on spheres of various diameters in a given wind tunnel and computing the critical Reynolds number.

The effects of the turbulence factor, TF, are quantified as an increase in effective Reynolds number, RN_e[38,39]:

$$RN_e = RN_{test} * TF \tag{90}$$

$$TF = 385{,}000/RN_{tunnel} \tag{91}$$

Where 380,000 is defined as the atmospheric free air Reynolds number. If this turbulence factor is relatively high as defined by Figure 6.26, the flow over the airfoil could prematurely transition from laminar to turbulent. This effect can be reduced, if not negated, by installing trip strips on the surfaces of the test article to help maintain laminar flow. Given that the amount of turbulence in the wind tunnel used for this investigation is unknown, the presence of vortex generators on the upper and lower surfaces of the vane is necessary to validate the assumption that a Reynolds number correction is unnecessary.

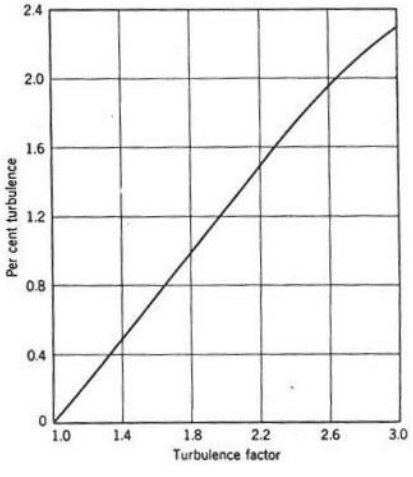

Figure 6.26 - Variation of Pressure Coefficient with Reynolds Number for a Sphere[38]

It should be noted that Rae and Pope[38] outline many other correction factors in their book. However, after reviewing the parameters for testing in which these corrections must be accounted for the author has eliminated them as possible sources of error. These parameters include, but are not limited to: wind tunnel cross section geometry, the difference between open and closed jets, as well as straight and re-circulating jets. The majority of these corrections are, in fact, built in to the equations listed in this section and should not be of concern to the reader.

7 Summary, Conclusions and Future Work

From the information presented in this document, the following can be documented:

i.) A new class of flutter test vanes has been developed for lightweight aircraft classes such as general aviation, light-sport, homebuilt and MAVs;

   a. This device weighs less than 2 pounds, having minimal effect on the modal mass of the aircraft to which it is mounted. The use of composite structures and piezoelectric actuators provide the mechanism for component weight reduction.

   b. This device maintains full force and phase control, allowing for multiple installations on a single airframe to work in harmony to achieve the desired testing parameters;

ii.) LNPS configurations are capable of amplification ratios on the order of 5:1 when compared to conventional piezoelectric bender actuator designs;

   a. Careful attention must be paid to both the stiffness of the reverse-bias spring as well as its compression ratio to avoid the snap-through phenomenon;

iii.) LNPS configurations are capable of magnification of work output in aforementioned actuators on the order of 4:1 when compared to conventional designs;

   a. This is achieved through the notion that LNPS configurations do not degrade the blocked moment of the original actuator design. The increase in work output is a direct result of a change in the slope of the moment-deflection curve and therefore an increase in the available design space;

iv.) Quasi-static and dynamic bench and wind tunnel testing provided excellent correlation between theory and experiment;

a. Wind tunnel tests were performed up to 110 ft/s;
b. Dynamic tests were performed in the range of 0.1 Hz to 60 Hz to determine the operational envelope of each configuration (LNPS and baseline);
c. A Froude scaled Cessna 210 model was mounted above acoustic puffers as a preliminary attempt at validation of a model showing the potential for dramatic increases in wingtip deflection by way of symmetric wing excitation;

v.) A comprehensive analysis of possible sources of error in dynamic and wind tunnel testing was performed, including characterization of the wind tunnel, test apparatuses and methods of data collection.

The findings presented above provide conclusive evidence that LNPS configurations can dramatically improve deflections in piezoelectric actuators. The result is such that the adaptive flutter test vane could be for flutter prediction procedures in small aircraft classes that may otherwise be difficult or unreliable. It can also be concluded that this device is capable of exciting structural modes of vibration unrelated to flutter, including fuselage bending ("tail wagging"). This phenomenon was observed during experiments carried out in the interest of determining the validity the mathematical flutter model.

The recommendations of this author include:

i.) Continuation of research in this field, including:

   a. Shake table testing for structural health analysis and component life estimation;

   b. Flight flutter testing to validate theoretical models and ground-based experimental results;

ii.) Thorough product marketing to insurance companies and original equipment manufacturers;

   a. This will provide the aviation community with a new, more reliable mechanism for determining the flutter characteristics of aircraft in an attempt to reduce accident rates and save lives.

REFERENCES

[1] Barnhart, R., and Barrett, R., "Piezoelectric Adaptive Flutter Test Vane: Low Net Passive Stiffness (LNPS) Techniques for Deflection Amplification," *Proceedings of the 53rd Structures, Structural Dynamics and Materials Conference*, Honolulu, HI, Apr. 23-26, 2012. AIAA Paper no. AIAA-2012-1906.

[2] Norton, Capt. William K., "Random Air Turbulence as a Flutter Test Excitation Source," *Proceedings*, 20th Annual Symposium, Society of Flight Test Engineers, Reno, Nevada, 1989, pp.6.4-1-6.4-11.

[3] William, C., Cooper, J.E., Wright, J.R., "Force Appropriation for Flight Flutter Testing Using Smart Devices," Proceedings of the 43rd AIAA/ASME/ASCE/AHS/ASC Structures, Structural Dynamics and Materials Conference, Denver, Colorado, Apr. 22-25, 2002.

[4] Vernon, L., "In-Flight Investigation of a Rotating Cylinder-Based Structural Excitation System for Flutter Testing," NASA TM-4512, June, 1993.

[5] Anon., "Aircraft Flutter Testing," *NASA Spinoff* [online resource], URL: http://www.sti.nasa.gov/tto/spinoff1997/t8.html [cited 16 August 2011].

[6] Barnhart, R., and Barrett, R., "Piezoelectric Adaptive Flutter Test Vane: Low Net Passive Stiffness (LNPS) Techniques for Deflection Amplification," *Proceedings of the 53rd Structures, Structural Dynamics and Materials Conference*, Honolulu, HI, Apr. 23-26, 2012. Technical Presentation Materials.

[7] Lesieutre, G., and Davis, C., "Can a coupling coefficient of a piezoelectric device be higher than those of its active material?", *Journal of Intelligent Materials Systems and Structures*, 1197, pp.859-867.

[8] Lesieutre, G. A. and Davis, C. L., "Transfer Having a Coupling Coefficient Higher than its Active Material," US Pat. 6,236,143 issued 22 May 2001.

[9] Barrett, R., Vos, R., Tiso, P., and De Breuker, R., "Post-Buckled Precompressed (PBP) Actuators: Enhancing VTOL Autonomous High Speed MAVs," *Proceedings of the 46th AIAA/ASME/ASCE/AHS/ASC Structures, Structural Dynamics and Materials Conference*, Austin, Texas, Apr. 18-21, 2005, AIAA paper no. AIAA-2005-2113.

[10] Barrett, R., McMurtry, R., Vos, R., Tiso, P., and De Breuker, R., "Post-Buckled Precompressed Piezoelectric Flight Control Actuator Design, Development and Demonstration," *Journal of Smart Materials and Structures*, Vol. 15, No. 5, October 2006, pp 1323-1331.

[11] Barrett, R., and Stutts, J. C., "Development of a Piezoceramic Flight Control Surface Actuator for Highly Compressed Munitions," *Proceedings of the 39th Structures, Structural Dynamics and Materials Conference* 20 - 23 April 1998, Long Beach, CA, AIAA, Washington, D.C. 1998, paper no. AIAA-98-203.

[12] Barrett, R., Vos, R., and De Breuker, R., "Post-Buckled Precompressed (PBP) Subsonic Micro Flight Control Actuators and Surfaces," *Proceedings of the SPIE 14th Annual International Symposium on Smart Structures and Materials*, vol. 6525, published by SPIE, Bellingham, WA, March 2007.

[13] Vos, R., Barrett, R., and Zehr, D., "Magnification of Work Output in PBP Class Actuators Using Buckling/Converse Buckling Techniques," *Proceedings of the 49th AIAA/ASME/ASCE/AHS/ASC Structures, Structural Dynamics, and Materials Conference,* Shaumburg, Illinois, Apr. 7-10, 2008, AIAA paper no. AIAA 2008-1705.

[14] Vos, R., Barrett, R., van Tooren, M., Krakers, L., "Post-Buckled Precompressed (PBP) Piezoelectric Actuators for UAV Flight Control," Proceedings of SPIE Vol. 6173, 61730E Smart Structures and Materials, 2006.

[15] Vangbo, M., "An analytical analysis of a compressed bistable buckled beam, Sensors and Actuators A," Physical Volume 69, Issue 3, pp. 212-216, 1998.

[16] Giannopoulos, G., Monreal, J., and Vantomme, J., "Snap-through buckling behavior of piezoelectric bimorph beams: I. Analytical and numerical modeling," Smart Materials and Structures, Volume 16, Number 4, pp. 1148-1157.

[17] Giannopoulos, G., Monreal, J., and Vantomme, J., "Snap-through buckling behavior of piezoelectric bimorph beams: II. Experimental verification," Smart Materials and Structures, Volume 16, Number 4, pp. 1158-1163.

[18] Schultz, M.R. and Hyer, M.W., "Snap-through of Unsymmetric Cross-ply Laminates using Piezoceramic Actuators", *Journal of Intelligent Material System and Structures*, Vol. 14, 2003, p. 795:814. 44.

[19] Schultz, M.R., "Use of Piezoelectric Actuators to Effect Snap-Through Behavior of Unsymmetric Composite Laminates", Ph.D. Dissertation, Engineering Science and Mechanics, Virginia Polytechnic Institute and State University, Blacksburg, Virginia, 2003.

[20] Schultz, M.R. and Hyer, M.W., "A Morphing Concept Based on Unsymmetric Composite Laminates and MFC Piezoceramic Actuators", *45th AIAA/ASME/ASCE/AHS/ASC Structures, Structural Dynamics and Materials Conference*, Palm Springs, California, 2004.

[21] Jones, R., "Mechanics of Composite Materials," 2nd Ed., Taylor and Francis Group, New York, New York, 1999.

[22] Barrett, R., and Barnhart, R., "Solid State Adaptive Rotor Using Postbuckled Precompressed, Bending-Twist Coupled Piezoelectric Actuator Elements," *Journal of Smart Materials Research,* Volume 2012, Article ID 832939.

[23] Moskalik, A.J., and Brei, D., "Analytical Dynamic Performance Modeling for Individual C-Block Actuators," *Journal of Vibration and Acoustics* **121** 221-30. 1998.

[24] Moskalik, A.J., and Brei, D., "Force-Deflection Behavior of Piezoelectric C-Block Actuator Arrays," *Journal of Smart Materials and Structures* **8** 531-43. 1999.

[25] Ervin, J., and Brei, D., "Recurve Piezoelectric-Strain-Amplifying Actuator Architecture," *IEEE/ASME Transactions on Mechatronics* **3** 293-301, 1998.

[26] Xu, W., and King, T., "Flexure Hinges for Piezoactuator Displacement Amplifiers: Flexibility, Accuracy, and Stress Considerations," *Journal of American Society of Precision Engineering (ASPE),* Vol 19, No. 1, July 1996, pp 4-10.

[27] Vos, R., and Barrett, R., "Dynamic Elastic Axis Shifting: An Important Enhancement of Postbuckled Precompressed (PBP) Actuators," *Proceedings of 48th AIAA/ASME/ASCE/AHS/ASC Structures, Structural Dynamics, and Materials Conference,* Honolulu, Hawaii, Apr. 23-26, 2007, paper no. AIAA-2007-1705.

[28] Vos, R. and Barrett, R., "Post-Buckled Precompressed Techniques in Adaptive Aerostructures: An Overview," *Proceedings of ASME 2008 Conference on Smart Materials, Adaptive Structures and Intelligent Systems,* Ellicot City, MD, Oct. 28-30, 2008.

[29] Barrett, R., and Vos, R., "Design, Development and Testing of a Transonic Missile Fin Employing PBP/DEAS Actuators," *Proceedings of SPIE Annual International Symposium on Smart Structures and Materials,* San Diego, CA, Mar. 10-13 2008. SPIE paper no. 6930-37.

[30] Roskam, J., "Airplane Design Part VI: Preliminary Calculation of Aerodynamic, Thrust and Power Characteristics," 5th ed., Lawrence, KS, 2008.

[31] Inman, D., "Engineering Vibrations," 3rd ed., Upper Saddle River, NJ, 2008.

[32] Anon., "Aircraft Wing Structure," Web Image, http://www.groundinstructor.com/mod/page/view.php?id=905.

[33] Faltinsen, O.M., "Hydrodynamics of High-Speed Marine Vehicles," Cambridge, NY, 2005, pp. 338.

[34] Bramlette, R. and Leurck, R., "A Method for Control Surface Deflection Utilizing Piezoceramic Bimorph Actuators," *44th AIAA Aerospace Sciences Meeting, Reno, NV, January 2006.* AIAA paper no. 2006-146.

[35] Miller, H., "Investigation of Errors Obtained with Reflection-Plane Mounted Models due to End Plate Tares," California Institute of Technology, Pasadena, CA, 1948.

[36] Leishman, J., "Principles of Helicopter Aerodynamics," 2nd ed., Cambridge, NY, 2007.

[37] Kerho, M., "Adaptive Airfoil Dynamic Stall Control," *43rd Aerospace Sciences Meeting*, Reno, NV, January 2005. AIAA paper no. 2005-1365.

[38] Rae, W., Pope, A., "Low-Speed Wind Tunnel Testing," 2nd ed., New York, NY, 1984.

[39] Lan, C.T.E, Roskam, J., "Airplane Aerodynamics and Performance," 3rd ed., Lawrence, KS, 2003.

APPENDIX A
DATA TABLES

Table of Contents

A.1 Quasi-Static Test Data: 3.5" End Plate

Note: All data collected at CV=±180V

Table A.1 - 3.5" EP Force Isolation - No Spring

Airspeed	Freq	P2P Deflection					Predicted Load (AR=1)	Predicted Load (AR=2)	Actual Load	Peak/Average St. Dev.	Experimental Lift Curve Slope	Experimental Lift Coefficient	Reduced Frequency
		Run 1	Run 2	Run 3	Avg	St. Dev.							
ft/sec	Hz	deg	deg	deg	deg	deg	lb_f	lb_f	lb_f	lb_f	1/deg	--	--
0.0	0.1	2.0	1.8	1.8	1.87	0.12							
36.9	0.1	2.0	1.9	1.9	1.93	0.06	0.04	0.06					
52.2	0.1	2.0	1.9	1.9	1.93	0.06	0.08	0.12	0.07	0.021	0.0265	0.051	0.004
64.0	0.1	2.0	1.9	1.9	1.93	0.06	0.11	0.18	0.11	0.028	0.0263	0.051	0.003
73.9	0.1	2.0	1.9	1.9	1.93	0.06	0.15	0.24	0.16	0.037	0.0287	0.055	0.003
82.6	0.1	2.0	1.9	1.9	1.93	0.06	0.19	0.30	0.21	0.046	0.0301	0.058	0.003
90.5	0.1	2.0	2.0	1.9	1.97	0.06	0.23	0.37	0.26	0.055	0.0306	0.060	0.002
97.7	0.1	2.0	2.0	1.9	1.97	0.06	0.27	0.43	0.31	0.060	0.0313	0.062	0.002
104.5	0.1	2.0	2.0	2.0	2.00	0.00	0.31	0.50	0.36	0.068	0.0312	0.062	0.002
110.8	0.1	2.0	2.0	2.0	2.00	0.00	0.35	0.56	0.41	0.071	0.0314	0.063	0.002
									AVERAGE:	0.048	0.030		

Table A.2 - 3.5" EP Force Isolation - Spring 1

Airspeed	Freq	P2P Deflection					Predicted Load (AR=1)	Predicted Load (AR=2)	Actual Load	Peak/Average St. Dev.	Experimental Lift Curve Slope	Experimental Lift Coefficient	Reduced Frequency
		Run 1	Run 2	Run 3	Avg	St. Dev.							
ft/sec	Hz	deg	deg	deg	deg	deg	lb_f	lb_f	lb_f	lb_f	1/deg	--	--
0.0	0.1	7.50	7.50	7.50	7.50	0.00							
36.9	0.1	7.60	7.60	7.50	7.57	0.06	0.15	0.24					
52.2	0.1	7.60	7.60	7.60	7.60	0.00	0.29	0.48					
64.0	0.1	7.60	7.60	7.60	7.60	0.00	0.44	0.71	0.16	0.196	0.0099	0.075	0.003
73.9	0.1	7.70	7.70	7.70	7.70	0.00	0.60	0.97	0.32	0.304	0.0144	0.111	0.003
82.6	0.1	7.70	7.70	7.70	7.70	0.00	0.75	1.21	0.50	0.436	0.0181	0.140	0.003
90.5	0.1	7.80	7.80	7.80	7.80	0.00	0.91	1.47	0.69	0.570	0.0205	0.160	0.002
97.7	0.1	7.80	7.80	7.80	7.80	0.00	1.06	1.71	0.86	0.689	0.0218	0.170	0.002
104.5	0.1	7.80	7.90	7.90	7.87	0.06	1.22	1.97	1.04	0.826	0.0229	0.180	0.002
110.8	0.1	7.80	7.90	7.90	7.87	0.06	1.37	2.22	1.25	0.956	0.0245	0.193	0.002
									AVERAGE:	0.568	0.019		

Table A.3 - 3.5" EP Force Isolation - Spring 2

Airspeed	Freq	P2P Deflection					Predicted Load (AR=1)	Predicted Load (AR=2)	Actual Load	Peak/Average St. Dev.	Experimental Lift Curve Slope	Experimental Lift Coefficient	Reduced Frequency
		Run 1	Run 2	Run 3	Avg	St. Dev.							
ft/sec	Hz	deg	deg	deg	deg	deg	lb_f	lb_f	lb_f	lb_f	1/deg	--	--
0.0	0.1	3.90	4.00	4.00	3.97	0.06							
36.9	0.1	4.00	4.20	4.10	4.10	0.10	0.08	0.13					
52.2	0.1	4.10	4.20	4.20	4.17	0.06	0.16	0.26	0.10	0.023	0.0168	0.070	0.004
64.0	0.1	4.10	4.30	4.20	4.20	0.10	0.24	0.39	0.19	0.030	0.0205	0.086	0.003
73.9	0.1	4.20	4.30	4.30	4.27	0.06	0.33	0.53	0.28	0.035	0.0228	0.097	0.003
82.6	0.1	4.20	4.40	4.40	4.33	0.12	0.42	0.68	0.37	0.044	0.0239	0.104	0.003
90.5	0.1	4.30	4.40	4.40	4.37	0.06	0.51	0.82	0.48	0.054	0.0253	0.111	0.002
97.7	0.1	4.30	4.50	4.50	4.43	0.12	0.60	0.97	0.58	0.060	0.0258	0.114	0.002
104.5	0.1	4.40	4.50	4.50	4.47	0.06	0.69	1.12	0.66	0.069	0.0258	0.115	0.002
110.8	0.1	4.40	4.50	4.50	4.47	0.06	0.78	1.26	0.75	0.078	0.0258	0.115	0.002
									AVERAGE:	0.049	0.023		

Table A.4 - 3.5" EP Force Isolation - Spring 3

Airspeed	Freq	P2P Deflection					Predicted Load (AR=1)	Predicted Load (AR=2)	Actual Load	Peak/Average St. Dev.	Experimental Lift Curve Slope	Experimental Lift Coefficient	Reduced Frequency
		Run 1	Run 2	Run 3	Avg	St. Dev.							
ft/sec	Hz	deg	deg	deg	deg	deg	lb_f	lb_f	lb_f	lb_f	1/deg	--	--
0.0	0.1	5.50	5.50	5.60	5.53	0.06							
36.9	0.1	5.50	5.70	5.60	5.60	0.10	0.11	0.18					
52.2	0.1	5.70	5.70	5.70	5.70	0.00	0.22	0.36	0.07	0.023	0.0089	0.050	0.004
64.0	0.1	5.70	5.80	5.70	5.73	0.06	0.33	0.54	0.19	0.029	0.0157	0.090	0.003
73.9	0.1	5.80	5.80	5.80	5.80	0.00	0.45	0.73	0.32	0.037	0.0190	0.110	0.003
82.6	0.1	5.80	5.80	5.80	5.80	0.00	0.56	0.91	0.44	0.044	0.0211	0.122	0.003
90.5	0.1	5.90	5.90	5.90	5.90	0.00	0.69	1.11	0.58	0.055	0.0228	0.135	0.002
97.7	0.1	5.90	5.90	5.90	5.90	0.00	0.80	1.29	0.73	0.065	0.0244	0.144	0.002
104.5	0.1	6.00	5.90	6.00	5.97	0.06	0.93	1.50	0.88	0.070	0.0254	0.152	0.002
110.8	0.1	6.00	6.00	6.00	6.00	0.00	1.05	1.69	0.99	0.072	0.0255	0.153	0.002
									AVERAGE:	0.049	0.020		

A.2 Quasi-Static Test Data 13.5" End Plate

Note: All data collected at CV=±180V

Table A.5 - 13.5" EP Force Isolation - No Spring

Airspeed	Freq	P2P Deflection					Predicted Load (AR=1)	Predicted Load (AR=2)	Actual Load	Peak/Average St. Dev.	Experimental Lift Curve Slope	Experimental Lift Coefficient	Reduced Frequency
		Run 1	Run 2	Run 3	Avg	St. Dev.							
ft/sec	Hz	deg	deg	deg	deg	deg	lb_f	lb_f	lb_f	lb_f	1/deg	--	--
0.0	0.1	2.0	2.0	2.0	2.00	0.00							
36.9	0.1	2.0	2.0	2.0	2.00	0.00	0.04	0.06					
52.2	0.1	2.0	2.1	2.0	2.03	0.06	0.08	0.13	0.09	0.025	0.0301	0.061	0.004
64.0	0.1	2.0	2.1	2.0	2.03	0.06	0.12	0.19	0.14	0.025	0.0319	0.065	0.003
73.9	0.1	2.0	2.1	2.0	2.03	0.06	0.16	0.25	0.19	0.029	0.0329	0.067	0.003
82.6	0.1	2.1	2.1	2.0	2.07	0.06	0.20	0.32	0.25	0.034	0.0338	0.070	0.003
90.5	0.1	2.1	2.1	2.1	2.10	0.00	0.24	0.39	0.31	0.037	0.0345	0.072	0.002
97.7	0.1	2.1	2.1	2.1	2.10	0.00	0.29	0.46	0.37	0.046	0.0351	0.074	0.002
104.5	0.1	2.1	2.1	2.1	2.10	0.00	0.33	0.53	0.44	0.045	0.0360	0.076	0.002
110.8	0.1	2.1	2.1	2.1	2.10	0.00	0.37	0.59	0.50	0.054	0.0364	0.076	0.002
									AVERAGE:	0.037	0.034		

Table A.6 - 13.5" EP Force Isolation - Spring 1

Airspeed	Freq	P2P Deflection					Predicted Load (AR=1)	Predicted Load (AR=2)	Actual Load	Peak/Average St. Dev.	Experimental Lift Curve Slope	Experimental Lift Coefficient	Reduced Frequency
		Run 1	Run 2	Run 3	Avg	St. Dev.							
ft/sec	Hz	deg	deg	deg	deg	deg	lb_f	lb_f	lb_f	lb_f	1/deg	--	--
0.0	0.1	8.00	8.10	8.20	8.10	0.10							
36.9	0.1	8.10	8.20	8.20	8.17	0.06	0.16	0.26					
52.2	0.1	8.20	8.30	8.30	8.27	0.06	0.32	0.52					
64.0	0.1	8.20	8.30	8.30	8.27	0.06	0.48	0.78	0.19	0.030	0.0108	0.089	0.003
73.9	0.1	8.20	8.40	8.30	8.30	0.10	0.64	1.04	0.41	0.040	0.0169	0.141	0.003
82.6	0.1	8.20	8.40	8.30	8.30	0.10	0.81	1.30	0.64	0.048	0.0212	0.176	0.003
90.5	0.1	8.20	8.40	8.40	8.33	0.12	0.97	1.57	0.87	0.054	0.0240	0.200	0.002
97.7	0.1	8.20	8.50	8.40	8.37	0.15	1.14	1.84	1.11	0.062	0.0263	0.220	0.002
104.5	0.1	8.20	8.50	8.40	8.37	0.15	1.30	2.10	1.34	0.067	0.0277	0.232	0.002
110.8	0.1	8.30	8.50	8.40	8.40	0.10	1.47	2.37	1.58	0.070	0.0290	0.244	0.002
									AVERAGE:	0.053	0.022		

Table A.7 - 13.5" EP Force Isolation - Spring 2

Airspeed	Freq	P2P Deflection					Predicted Load (AR=1)	Predicted Load (AR=2)	Actual Load	Peak/Average St. Dev.	Experimental Lift Curve Slope	Experimental Lift Coefficient	Reduced Frequency
		Run 1	Run 2	Run 3	Avg	St. Dev.							
ft/sec	Hz	deg	deg	deg	deg	deg	lb_f	lb_f	lb_f	lb_f	1/deg	--	--
0.0	0.1	3.80	3.90	3.90	3.87	0.06							
36.9	0.1	3.90	4.00	4.00	3.97	0.06	0.08	0.12					
52.2	0.1	4.00	4.00	4.00	4.00	0.00	0.16	0.25	0.12	0.027	0.0212	0.085	0.004
64.0	0.1	4.00	4.00	4.00	4.00	0.00	0.23	0.38	0.21	0.030	0.0246	0.099	0.003
73.9	0.1	4.10	4.00	4.00	4.03	0.06	0.31	0.51	0.32	0.032	0.0278	0.112	0.003
82.6	0.1	4.10	4.00	4.00	4.03	0.06	0.39	0.63	0.42	0.035	0.0292	0.118	0.003
90.5	0.1	4.10	4.00	4.00	4.03	0.06	0.47	0.76	0.53	0.042	0.0306	0.124	0.002
97.7	0.1	4.10	4.00	4.00	4.03	0.06	0.55	0.89	0.63	0.048	0.0310	0.125	0.002
104.5	0.1	4.10	4.00	4.00	4.03	0.06	0.63	1.01	0.72	0.047	0.0311	0.125	0.002
110.8	0.1	4.10	4.00	4.00	4.03	0.06	0.70	1.14	0.84	0.050	0.0320	0.129	0.002
									AVERAGE:	0.039	0.028		

Table A.8 - 13.5" EP Force Isolation Spring 3

Airspeed	Freq	P2P Deflection					Predicted Load (AR=1)	Predicted Load (AR=2)	Actual Load	Peak/Average St. Dev.	Experimental Lift Curve Slope	Experimental Lift Coefficient	Reduced Frequency
		Run 1	Run 2	Run 3	Avg	St. Dev.							
ft/sec	Hz	deg	deg	deg	deg	deg	lb_f	lb_f	lb_f	lb_f	1/deg	--	--
0.0	0.1	5.00	5.10	5.10	5.07	0.06							
36.9	0.1	5.10	5.10	5.10	5.10	0.00	0.10	0.16					
52.2	0.1	5.10	5.20	5.10	5.13	0.06	0.20	0.32	0.16	0.027	0.0218	0.112	0.004
64.0	0.1	5.20	5.20	5.20	5.20	0.00	0.30	0.49	0.28	0.029	0.0252	0.131	0.003
73.9	0.1	5.20	5.20	5.20	5.20	0.00	0.40	0.65	0.41	0.030	0.0276	0.143	0.003
82.6	0.1	5.20	5.30	5.20	5.23	0.06	0.51	0.82	0.55	0.035	0.0292	0.153	0.003
90.5	0.1	5.20	5.30	5.30	5.27	0.06	0.61	0.99	0.69	0.040	0.0303	0.160	0.002
97.7	0.1	5.30	5.30	5.30	5.30	0.00	0.72	1.16	0.83	0.045	0.0310	0.164	0.002
104.5	0.1	5.30	5.40	5.40	5.37	0.06	0.83	1.35	0.99	0.048	0.0320	0.172	0.002
110.8	0.1	5.30	5.40	5.40	5.37	0.06	0.94	1.51	1.14	0.051	0.0328	0.176	0.002
									AVERAGE:	0.038	0.029		

A.3 Dynamic Test Data

Table A. 1 - Dynamic Test Data - No Spring, CV=±180V

Airspeed	Freq	P2P Deflection					Actual Load	Experimental Lift Coefficient	Reduced Frequency
		Run 1	Run 2	Run 3	Avg	St. Dev.			
ft/sec	Hz	deg	deg	deg	deg	deg	lb_f	--	--
0.0	0.7	1.8	1.9	1.9	1.87	0.06			
	3.0	1.8	1.9	2.0	1.90	0.10			
	5.0	1.8	1.9	2.0	1.90	0.10			
	7.0	1.9	2.0	2.0	1.97	0.06			
	10.0	1.7	1.8	1.8	1.77	0.06			
45.2	0.7	1.8	1.9	2.0	1.90	0.10	0.08	0.074	0.03
	3.0	1.8	2.0	2.0	1.93	0.12	0.06	0.055	0.14
	5.0	1.8	2.0	2.0	1.93	0.12	0.06	0.055	0.23
	7.0	1.9	1.9	1.9	1.90	0.00	0.05	0.046	0.32
	10.0	1.7	1.8	1.8	1.77	0.06	0.13	0.120	0.46
73.9	0.7	1.9	2.0	2.0	1.97	0.06	0.20	0.069	0.02
	3.0	1.9	2.0	2.0	1.97	0.06	0.18	0.062	0.09
	5.0	2.0	2.0	2.0	2.00	0.00	0.17	0.059	0.14
	7.0	2.0	1.9	1.9	1.93	0.06	0.12	0.042	0.20
	10.0	1.9	1.8	1.8	1.83	0.06	0.15	0.052	0.28
94.2	0.7	1.9	1.9	2.0	1.93	0.06	0.33	0.070	0.02
	3.0	2.0	1.9	2.0	1.97	0.06	0.30	0.064	0.07
	5.0	2.1	2.0	2.0	2.03	0.06	0.28	0.060	0.11
	7.0	2.0	1.9	1.9	1.93	0.06	0.22	0.047	0.16
	10.0	1.9	1.8	1.8	1.83	0.06	0.20	0.043	0.22
110.8	0.7	2.0	1.9	2.0	1.97	0.06	0.47	0.072	0.01
	3.0	2.0	2.0	2.0	2.00	0.00	0.44	0.068	0.06
	5.0	1.9	2.1	2.1	2.03	0.12	0.40	0.062	0.09
	7.0	1.9	2.0	1.9	1.93	0.06	0.32	0.049	0.13
	10.0	1.9	1.9	1.8	1.87	0.06	0.22	0.034	0.19

Table A. 2 - Dynamic Test Data - No Spring, CV=±100V

Airspeed	Freq	P2P Deflection					Actual Load	Experimental Lift Coefficient	Reduced Frequency
		Run 1	Run 2	Run 3	Avg	St. Dev.			
ft/sec	Hz	deg	deg	deg	deg	deg	lb_f	--	--
0.0	12.0	1.0	1.0	1.0	1.00	0.00			
	14.0	1.1	1.0	1.0	1.03	0.06			
	16.0	1.3	1.3	1.2	1.27	0.06			
	18.0	1.0	1.1	1.0	1.03	0.06			
	20.0	1.0	1.0	1.1	1.03	0.06			
45.2	12.0	1.0	1.0	1.0	1.00	0.00	0.05	0.046	0.56
	14.0	1.0	1.1	1.0	1.03	0.06	0.06	0.055	0.65
	16.0	1.2	1.2	1.3	1.23	0.06	0.11	0.102	0.74
	18.0	1.0	1.1	1.0	1.03	0.06	0.09	0.083	0.83
	20.0	1.0	1.0	1.0	1.00	0.00	0.12	0.111	0.93
73.9	12.0	1.1	1.0	1.0	1.03	0.06	0.04	0.014	0.34
	14.0	1.2	1.1	1.1	1.13	0.06	0.05	0.017	0.40
	16.0	1.3	1.4	1.4	1.37	0.06	0.10	0.035	0.45
	18.0	1.0	1.1	1.1	1.07	0.06	0.09	0.031	0.51
	20.0	1.1	1.2	1.2	1.17	0.06	0.13	0.045	0.57
94.2	12.0	1.1	1.2	1.2	1.17	0.06	0.07	0.015	0.27
	14.0	1.3	1.3	1.3	1.30	0.00	0.06	0.013	0.31
	16.0	1.4	1.3	1.3	1.33	0.06	0.08	0.017	0.36
	18.0	1.1	1.1	1.2	1.13	0.06	0.09	0.019	0.40
	20.0	1.1	1.1	1.1	1.10	0.00	0.10	0.021	0.44
110.8	12.0	1.1	1.2	1.2	1.17	0.06	0.11	0.017	0.23
	14.0	1.2	1.3	1.3	1.27	0.06	0.08	0.012	0.26
	16.0	1.3	1.2	1.2	1.23	0.06	0.09	0.014	0.30
	18.0	1.1	1.1	1.1	1.10	0.00	0.08	0.012	0.34
	20.0	1.2	1.2	1.2	1.20	0.00	0.10	0.015	0.38

Table A. 3 - Dynamic Test Data - No Spring, CV=±50V

Airspeed	Freq	P2P Deflection					Actual Load	Experimental Lift Coefficient	Reduced Frequency
		Run 1	Run 2	Run 3	Avg	St. Dev.			
ft/sec	Hz	deg	deg	deg	deg	deg	lb_f	--	--
0.0	22.0	0.8	0.6	0.7	0.70	0.10			
	25.0	1.0	0.9	1.0	0.97	0.06			
	27.0	1.7	1.7	1.7	1.70	0.00			
	28.0	2.6	2.5	2.5	2.53	0.06			
	29.0	4.0	4.0	4.0	4.00	0.00			
	30.0	3.7	3.7	3.8	3.73	0.06			
	31.0	2.2	2.3	2.4	2.30	0.10			
	32.0	1.7	1.6	1.7	1.67	0.06			
	33.0	1.1	1.1	1.3	1.17	0.12			
	34.0	1.0	0.9	0.7	0.87	0.15			
	36.0	0.5	0.5	0.5	0.50	0.00			
	38.0	0.4	0.4	0.4	0.40	0.00			
	40.0	0.5	0.6	0.5	0.53	0.06			
	45.0	0.2	0.2	0.2	0.20	0.00			
45.2	22.0	0.8	0.7	0.7	0.73	0.06	0.06	0.055	1.02
	25.0	1.0	1.0	1.0	1.00	0.00	0.08	0.074	1.16
	27.0	1.7	1.7	1.7	1.70	0.00	0.15	0.139	1.25
	28.0	2.3	2.3	2.4	2.33	0.06	0.23	0.213	1.30
	29.0	3.1	3.3	3.3	3.23	0.12	0.36	0.333	1.34
	30.0	3.0	3.3	3.3	3.20	0.17	0.40	0.370	1.39
	31.0	2.1	2.2	2.3	2.20	0.10	0.29	0.268	1.44
	32.0	1.6	1.5	1.6	1.57	0.06	0.23	0.213	1.48
	33.0	1.2	1.2	1.3	1.23	0.06	0.18	0.166	1.53
	34.0	0.9	0.8	0.7	0.80	0.10	0.16	0.148	1.57
	36.0	0.6	0.5	0.5	0.53	0.06	0.19	0.176	1.67
	38.0	0.4	0.4	0.4	0.40	0.00	0.11	0.102	1.76
	40.0	0.5	0.5	0.5	0.50	0.00	0.12	0.111	1.85
	45.0	0.2	0.2	0.2	0.20	0.00	0.02	0.018	2.08
73.9	22.0	0.8	0.7	0.7	0.73	0.06	0.05	0.017	0.62
	25.0	1.0	1.0	1.0	1.00	0.00	0.08	0.028	0.71
	27.0	1.6	1.7	1.7	1.67	0.06	0.14	0.049	0.77
	28.0	2.0	2.1	2.2	2.10	0.10	0.19	0.066	0.79
	29.0	2.5	2.5	2.6	2.53	0.06	0.26	0.090	0.82
	30.0	2.5	2.6	2.6	2.57	0.06	0.29	0.101	0.85
	31.0	1.9	1.9	2.0	1.93	0.06	0.24	0.083	0.88
	32.0	1.3	1.5	1.4	1.40	0.10	0.19	0.066	0.91
	33.0	1.0	1.0	1.2	1.07	0.12	0.16	0.055	0.94
	34.0	0.9	0.9	0.7	0.83	0.12	0.15	0.052	0.96
	36.0	0.5	0.5	0.5	0.50	0.00	0.16	0.055	1.02
	38.0	0.4	0.4	0.4	0.40	0.00	0.10	0.035	1.08
	40.0	0.5	0.5	0.5	0.50	0.00	0.13	0.045	1.13
	45.0	0.2	0.2	0.2	0.20	0.00	0.02	0.007	1.28
94.2	22.0	0.8	0.8	0.7	0.77	0.06	0.05	0.011	0.49
	25.0	1.0	1.0	1.0	1.00	0.00	0.07	0.015	0.56
	27.0	1.7	1.7	1.6	1.67	0.06	0.12	0.026	0.60
	28.0	2.0	2.0	2.0	2.00	0.00	0.17	0.036	0.62
	29.0	2.2	2.2	2.5	2.30	0.17	0.21	0.045	0.64
	30.0	2.2	2.3	2.4	2.30	0.10	0.23	0.049	0.67
	31.0	1.8	1.8	1.8	1.80	0.00	0.20	0.043	0.69
	32.0	1.3	1.4	1.4	1.37	0.06	0.17	0.036	0.71
	33.0	1.0	1.0	1.1	1.03	0.06	0.14	0.030	0.73
	34.0	0.9	0.8	0.7	0.80	0.10	0.14	0.030	0.76
	36.0	0.5	0.5	0.5	0.50	0.00	0.16	0.034	0.80
	38.0	0.4	0.4	0.4	0.40	0.00	0.10	0.021	0.85
	40.0	0.5	0.5	0.5	0.50	0.00	0.15	0.032	0.89
	45.0	0.2	0.2	0.2	0.20	0.00	0.02	0.004	1.00
110.8	22.0	0.8	0.8	0.7	0.77	0.06	0.04	0.006	0.42
	25.0	1.1	1.0	1.1	1.07	0.06	0.07	0.011	0.47
	27.0	1.6	1.5	1.6	1.57	0.06	0.11	0.017	0.51
	28.0	1.9	1.9	1.8	1.87	0.06	0.14	0.022	0.53
	29.0	2.1	2.1	2.2	2.13	0.06	0.18	0.028	0.55
	30.0	2.0	2.1	2.2	2.10	0.10	0.19	0.029	0.57
	31.0	1.7	1.7	1.7	1.70	0.00	0.17	0.026	0.59
	32.0	1.3	1.4	1.3	1.33	0.06	0.14	0.022	0.60
	33.0	1.0	1.0	1.1	1.03	0.06	0.12	0.018	0.62
	34.0	0.9	0.9	0.7	0.83	0.12	0.13	0.020	0.64
	36.0	0.5	0.5	0.5	0.50	0.00	0.15	0.023	0.68
	38.0	0.4	0.4	0.4	0.40	0.00	0.10	0.015	0.72
	40.0	0.5	0.5	0.5	0.50	0.00	0.15	0.023	0.76
	45.0	0.2	0.2	0.2	0.20	0.00	0.02	0.003	0.85

Table A. 4 - Dynamic Test Data - No Spring, CV=±20V

Airspeed	Freq	P2P Deflection					Actual Load	Experimental Lift Coefficient	Reduced Frequency
		Run 1	Run 2	Run 3	Avg	St. Dev.			
ft/sec	Hz	deg	deg	deg	deg	deg	lb_f	--	--
0.0	22.0	0.2	0.2	0.1	0.17	0.06			
	25.0	0.2	0.3	0.3	0.27	0.06			
	27.0	0.3	0.4	0.4	0.37	0.06			
	28.0	0.5	0.6	0.6	0.57	0.06			
	29.0	2.0	2.1	2.0	2.03	0.06			
	30.0	1.9	2.0	2.0	1.97	0.06			
	31.0	1.2	1.2	1.2	1.20	0.00			
	32.0	1.0	1.0	0.9	0.97	0.06			
	33.0	0.8	0.9	0.7	0.81	0.09			
	34.0	0.6	0.6	0.6	0.60	0.00			
	35.0	0.5	0.5	0.4	0.47	0.06			
	36.0	0.3	0.3	0.3	0.30	0.00			
	38.0	0.2	0.2	0.1	0.17	0.06			
45.2	22.0	0.3	0.2	0.1	0.20	0.10	0.02	0.018	1.02
	25.0	0.3	0.3	0.2	0.27	0.06	0.03	0.028	1.16
	27.0	0.4	0.5	0.4	0.43	0.06	0.04	0.037	1.25
	28.0	0.7	0.7	0.6	0.67	0.06	0.06	0.055	1.30
	29.0	1.0	1.2	1.1	1.10	0.10	0.13	0.120	1.34
	30.0	1.3	1.5	1.5	1.43	0.12	0.16	0.148	1.39
	31.0	1.1	1.1	1.1	1.10	0.00	0.12	0.111	1.44
	32.0	1.0	0.9	0.9	0.93	0.06	0.11	0.102	1.48
	33.0	0.7	0.7	0.7	0.70	0.00	0.10	0.092	1.53
	34.0	0.7	0.6	0.6	0.63	0.06	0.10	0.092	1.57
	35.0	0.6	0.5	0.5	0.53	0.06	0.09	0.083	1.62
	36.0	0.4	0.4	0.4	0.40	0.00	0.07	0.065	1.67
	38.0	0.2	0.2	0.1	0.17	0.06	0.09	0.083	1.76
73.9	22.0	0.3	0.2	0.1	0.20	0.10	0.02	0.007	0.62
	25.0	0.4	0.3	0.3	0.33	0.06	0.03	0.010	0.71
	27.0	0.6	0.5	0.5	0.53	0.06	0.04	0.014	0.77
	28.0	0.8	0.7	0.6	0.70	0.10	0.05	0.017	0.79
	29.0	1.0	1.0	1.0	1.00	0.00	0.08	0.028	0.82
	30.0	1.1	1.1	1.1	1.10	0.00	0.11	0.038	0.85
	31.0	1.0	1.0	1.0	1.00	0.00	0.08	0.028	0.88
	32.0	0.9	0.9	0.8	0.87	0.06	0.09	0.031	0.91
	33.0	0.8	0.7	0.6	0.70	0.10	0.09	0.031	0.94
	34.0	0.6	0.6	0.5	0.57	0.06	0.08	0.028	0.96
	35.0	0.4	0.4	0.4	0.40	0.00	0.08	0.028	0.99
	36.0	0.3	0.3	0.3	0.30	0.00	0.06	0.021	1.02
	38.0	0.2	0.2	0.1	0.17	0.06	0.08	0.028	1.08
94.2	22.0	0.2	0.2	0.2	0.20	0.00	0.02	0.004	0.49
	25.0	0.3	0.3	0.3	0.30	0.00	0.03	0.006	0.56
	27.0	0.7	0.5	0.5	0.57	0.12	0.04	0.009	0.60
	28.0	0.8	0.8	0.6	0.73	0.12	0.06	0.013	0.62
	29.0	1.0	1.0	0.9	0.97	0.06	0.07	0.015	0.64
	30.0	1.1	1.1	1.0	1.07	0.06	0.09	0.019	0.67
	31.0	1.0	1.0	0.9	0.97	0.06	0.05	0.011	0.69
	32.0	0.8	0.8	0.7	0.77	0.06	0.09	0.019	0.71
	33.0	0.7	0.6	0.6	0.63	0.06	0.08	0.017	0.73
	34.0	0.5	0.4	0.5	0.47	0.06	0.07	0.015	0.76
	35.0	0.4	0.3	0.3	0.33	0.06	0.07	0.015	0.78
	36.0	0.3	0.2	0.2	0.23	0.06	0.07	0.015	0.80
	38.0	0.2	0.1	0.1	0.13	0.06	0.07	0.015	0.85
110.8	22.0	0.2	0.2	0.2	0.20	0.00	0.02	0.003	0.42
	25.0	0.4	0.3	0.3	0.33	0.06	0.03	0.005	0.47
	27.0	0.6	0.5	0.5	0.53	0.06	0.04	0.006	0.51
	28.0	0.8	0.7	0.7	0.73	0.06	0.05	0.008	0.53
	29.0	0.9	0.8	0.8	0.83	0.06	0.06	0.009	0.55
	30.0	1.0	0.9	0.9	0.93	0.06	0.08	0.012	0.57
	31.0	0.9	0.9	0.7	0.83	0.12	0.06	0.009	0.59
	32.0	0.7	0.7	0.6	0.67	0.06	0.08	0.012	0.60
	33.0	0.5	0.5	0.5	0.50	0.00	0.07	0.011	0.62
	34.0	0.4	0.3	0.3	0.33	0.06	0.07	0.011	0.64
	35.0	0.3	0.2	0.2	0.23	0.06	0.06	0.009	0.66
	36.0	0.2	0.1	0.1	0.13	0.06	0.07	0.011	0.68
	38.0	0.1	0.1	0.1	0.10	0.00	0.06	0.009	0.72

Table A. 5 - Dynamic Test Data - No Spring, CV=±20V (Corner Frequency Determination)

Airspeed	Freq	P2P Deflection					Actual Load	Experimental Lift Coefficient	Reduced Frequency
		Run 1	Run 2	Run 3	Avg	St. Dev.			
ft/sec	Hz	deg	deg	deg	deg	deg	lb_f	--	--
0.00	40.0	0.5	0.5	0.5	0.50	0.00			
	45.0	0.3	0.3	0.3	0.30	0.00			
	50.0	0.1	0.1	0.1	0.10	0.00			
	55.0	0.0	0.0	0.0	0.00	0.00			
	60.0	0.0	0.0	0.0	0.00	0.00			
45.2	40.0	0.5	0.5	0.5	0.50	0.00	0.09	0.083	1.85
	45.0	0.3	0.3	0.3	0.30	0.00	0.01	0.009	2.08
	50.0	0.1	0.1	0.1	0.10	0.00	0.01	0.009	2.31
	55.0	0.0	0.0	0.0	0.00	0.00	0.01	0.009	2.55
	60.0	0.0	0.0	0.0	0.00	0.00	0.01	0.005	2.78
73.9	40.0	0.4	0.5	0.4	0.43	0.06	0.09	0.031	1.13
	45.0	0.2	0.2	0.1	0.17	0.06	0.01	0.003	1.28
	50.0	0.1	0.0	0.0	0.03	0.06	0.01	0.002	1.42
	55.0	0.0	0.0	0.0	0.00	0.00	0.01	0.003	1.56
	60.0	0.0	0.0	0.0	0.00	0.00	0.01	0.002	1.70
94.2	40.0	0.3	0.3	0.3	0.30	0.00	0.11	0.023	0.89
	45.0	0.1	0.1	0.1	0.10	0.00	0.01	0.001	1.00
	50.0	0.0	0.0	0.0	0.00	0.00	0.01	0.001	1.11
	55.0	0.0	0.0	0.0	0.00	0.00	0.01	0.002	1.22
	60.0	0.0	0.0	0.0	0.00	0.00	0.01	0.001	1.33
110.8	40.0	0.3	0.2	0.2	0.23	0.06	0.11	0.017	0.76
	45.0	0.1	0.1	0.1	0.10	0.00	0.01	0.002	0.85
	50.0	0.0	0.0	0.0	0.00	0.00	0.01	0.002	0.94
	55.0	0.0	0.0	0.0	0.00	0.00	0.01	0.002	1.04
	60.0	0.0	0.0	0.0	0.00	0.00	0.01	0.001	1.13

Table A. 6 - Dynamic Test Data - Spring 1, CV=±180V

Airspeed	Freq	P2P Deflection					Actual Load	Experimental Lift Coefficient	Reduced Frequency
		Run 1	Run 2	Run 3	Avg	St. Dev.			
ft/sec	Hz	deg	deg	deg	deg	deg	lb_f	--	--
0.0	0.7	6.7	6.8	6.8	6.77	0.06			
	3.0	7.3	7.4	7.5	7.40	0.10			
	5.0	7.7	8.0	7.9	7.87	0.15			
	7.0	7.6	7.7	7.8	7.70	0.10			
	10.0	6.2	6.1	6.1	6.13	0.06			
45.2	0.7	6.7	6.9	6.8	6.80	0.10	0.13	0.120	0.03
	3.0	7.4	7.4	7.5	7.43	0.06	0.27	0.250	0.14
	5.0	7.7	8.0	8.0	7.90	0.17	0.24	0.222	0.23
	7.0	7.7	7.7	7.8	7.73	0.06	0.37	0.342	0.32
	10.0	6.6	6.0	6.1	6.23	0.32	0.33	0.305	0.46
73.9	0.7	6.8	6.9	6.9	6.87	0.06	0.49	0.170	0.02
	3.0	7.3	7.2	7.5	7.33	0.15	0.42	0.146	0.09
	5.0	7.7	7.9	7.8	7.80	0.10	0.41	0.142	0.14
	7.0	7.6	7.7	7.7	7.67	0.06	0.40	0.139	0.20
	10.0	6.4	5.6	6.3	6.10	0.44	0.32	0.111	0.28
94.2	0.7	6.8	6.9	6.9	6.87	0.06	0.92	0.196	0.02
	3.0	7.2	7.4	7.5	7.37	0.15	0.87	0.186	0.07
	5.0	7.2	7.5	7.6	7.43	0.21	0.70	0.149	0.11
	7.0	7.1	7.4	7.1	7.20	0.17	0.55	0.117	0.16
	10.0	6.4	6.7	6.5	6.53	0.15	0.35	0.075	0.22
110.8	0.7	6.7	6.9	6.9	6.83	0.12	1.34	0.206	0.01
	3.0	7.1	7.3	7.2	7.20	0.10	1.34	0.206	0.06
	5.0	7.2	7.4	7.4	7.33	0.12	1.11	0.171	0.09
	7.0	6.6	6.6	6.3	6.50	0.17	0.86	0.133	0.13
	10.0	5.8	5.9	5.7	5.80	0.10	0.50	0.077	0.19

Table A. 7 - Dynamic Test Data - Spring 1, CV=±50V

Airspeed	Freq	P2P Deflection					Actual Load	Experimental Lift Coefficient	Reduced Frequency
		Run 1	Run 2	Run 3	Avg	St. Dev.			
ft/sec	Hz	deg	deg	deg	deg	deg	lb_f	--	--
0.0	10.0	0.5	0.4	0.4	0.43	0.06			
	12.0	0.6	0.5	0.5	0.53	0.06			
	14.0	0.7	0.6	0.6	0.63	0.06			
	16.0	0.9	0.7	0.7	0.77	0.12			
	17.0	1.1	0.8	0.8	0.90	0.17			
	18.0	1.4	0.9	0.8	1.03	0.32			
	19.0	1.8	1.0	0.9	1.23	0.49			
	20.0	2.0	1.2	1.0	1.40	0.53			
	21.0	2.6	1.5	1.3	1.80	0.70			
	22.0	3.3	1.9	1.7	2.30	0.87			
	23.0	2.7	3.7	3.9	3.43	0.64			
	24.0	2.1	3.0	3.3	2.80	0.62			
	26.0	1.7	2.2	2.2	2.03	0.29			
	28.0	1.0	1.3	1.6	1.30	0.30			
	30.0	0.6	0.7	0.8	0.70	0.10			
	35.0	0.4	0.4	0.5	0.43	0.06			
	40.0	0.2	0.2	0.3	0.23	0.06			
45.2	10.0	0.4	0.4	0.4	0.40	0.00	0.03	0.028	0.46
	12.0	0.5	0.5	0.5	0.50	0.00	0.04	0.037	0.56
	14.0	0.6	0.6	0.6	0.60	0.00	0.05	0.046	0.65
	16.0	0.8	0.7	0.7	0.73	0.06	0.05	0.046	0.74
	17.0	0.9	0.7	0.8	0.80	0.10	0.05	0.046	0.79
	18.0	1.1	0.8	0.8	0.90	0.17	0.06	0.055	0.83
	19.0	1.3	0.9	0.9	1.03	0.23	0.07	0.065	0.88
	20.0	1.6	1.0	1.0	1.20	0.35	0.08	0.074	0.93
	21.0	1.9	1.3	1.3	1.50	0.35	0.10	0.092	0.97
	22.0	2.7	1.6	1.6	1.97	0.64	0.11	0.102	1.02
	23.0	2.8	2.0	1.9	2.23	0.49	0.17	0.157	1.06
	24.0	2.2	2.9	3.1	2.73	0.47	0.29	0.268	1.11
	26.0	1.7	2.0	2.0	1.90	0.17	0.25	0.231	1.20
	28.0	1.2	1.5	1.6	1.43	0.21	0.19	0.176	1.30
	30.0	0.6	0.8	1.0	0.80	0.20	0.16	0.148	1.39
	35.0	0.4	0.4	0.5	0.43	0.06	0.11	0.102	1.62
	40.0	0.2	0.2	0.2	0.20	0.00	0.16	0.148	1.85
73.9	10.0	0.4	0.4	0.3	0.37	0.06	0.03	0.010	0.28
	12.0	0.5	0.5	0.4	0.47	0.06	0.03	0.010	0.34
	14.0	0.6	0.5	0.5	0.53	0.06	0.04	0.014	0.40
	16.0	0.7	0.6	0.6	0.63	0.06	0.04	0.014	0.45
	17.0	0.7	0.6	0.6	0.63	0.06	0.04	0.014	0.48
	18.0	0.9	0.7	0.6	0.73	0.15	0.04	0.014	0.51
	19.0	1.1	0.8	0.7	0.87	0.21	0.06	0.021	0.54
	20.0	1.3	0.9	0.8	1.00	0.26	0.07	0.024	0.57
	21.0	1.5	1.3	1.1	1.30	0.20	0.07	0.024	0.60
	22.0	1.8	1.5	1.3	1.53	0.25	0.06	0.021	0.62
	23.0	2.3	1.7	1.5	1.83	0.42	0.12	0.042	0.65
	24.0	2.3	2.2	1.9	2.13	0.21	0.18	0.062	0.68
	26.0	1.8	2.1	2.2	2.03	0.21	0.25	0.087	0.74
	28.0	1.4	1.6	1.7	1.57	0.15	0.19	0.066	0.79
	30.0	0.7	1.0	1.0	0.90	0.17	0.16	0.055	0.85
	35.0	0.4	0.4	0.4	0.40	0.00	0.10	0.035	0.99
	40.0	0.2	0.2	0.2	0.20	0.00	0.17	0.059	1.13
94.2	10.0	0.2	0.3	0.3	0.27	0.06	0.06	0.013	0.22
	12.0	0.4	0.4	0.4	0.40	0.00	0.04	0.009	0.27
	14.0	0.4	0.4	0.4	0.40	0.00	0.04	0.009	0.31
	16.0	0.5	0.5	0.5	0.50	0.00	0.04	0.009	0.36
	17.0	0.6	0.5	0.5	0.53	0.06	0.04	0.009	0.38
	18.0	0.7	0.6	0.6	0.63	0.06	0.04	0.009	0.40
	19.0	0.9	0.7	0.7	0.77	0.12	0.05	0.011	0.42
	20.0	1.1	0.9	0.8	0.93	0.15	0.06	0.013	0.44
	21.0	1.2	1.0	1.0	1.07	0.12	0.06	0.013	0.47
	22.0	1.4	1.2	1.1	1.23	0.15	0.05	0.011	0.49
	23.0	1.6	1.3	1.3	1.40	0.17	0.11	0.023	0.51
	24.0	2.0	1.5	1.4	1.63	0.32	0.13	0.028	0.53
	26.0	1.9	2.0	2.2	2.03	0.15	0.21	0.045	0.58
	28.0	1.4	1.5	1.6	1.50	0.10	0.19	0.041	0.62
	30.0	0.9	1.0	1.1	1.00	0.10	0.15	0.032	0.67
	35.0	0.5	0.5	0.5	0.50	0.00	0.11	0.023	0.78
	40.0	0.2	0.2	0.3	0.23	0.06	0.18	0.038	0.89
110.8	10.0	0.4	0.3	0.3	0.33	0.06	0.07	0.011	0.19
	12.0	0.5	0.5	0.5	0.50	0.00	0.05	0.008	0.23
	14.0	0.6	0.6	0.6	0.60	0.00	0.05	0.008	0.26
	16.0	0.7	0.6	0.6	0.63	0.06	0.04	0.006	0.30
	17.0	0.7	0.7	0.7	0.70	0.00	0.04	0.006	0.32
	18.0	0.8	0.7	0.7	0.73	0.06	0.04	0.006	0.34
	19.0	0.9	0.8	0.8	0.83	0.06	0.04	0.006	0.36
	20.0	0.9	0.9	0.9	0.90	0.00	0.06	0.009	0.38
	21.0	1.0	1.0	0.9	0.97	0.06	0.04	0.006	0.40
	22.0	1.0	1.0	1.0	1.00	0.00	0.07	0.011	0.42
	23.0	1.1	1.0	1.0	1.03	0.06	0.08	0.012	0.43
	24.0	1.3	1.1	1.1	1.17	0.12	0.09	0.014	0.45
	26.0	1.9	1.7	1.8	1.80	0.10	0.16	0.025	0.49
	28.0	1.3	1.6	1.6	1.50	0.17	0.17	0.026	0.53
	30.0	1.0	1.1	1.1	1.07	0.06	0.15	0.023	0.57
	35.0	0.6	0.6	0.7	0.63	0.06	0.10	0.015	0.66
	40.0	0.4	0.4	0.3	0.37	0.06	0.18	0.028	0.76

Table A. 8 - Dynamic Test Data - Spring 2, CV=±180V

Airspeed	Freq	P2P Deflection					Actual Load	Experimental Lift Coefficient	Reduced Frequency
		Run 1	Run 2	Run 3	Avg	St. Dev.			
ft/sec	Hz	deg	deg	deg	deg	deg	lb_f	--	--
0.0	0.7	3.1	3.1	3.1	3.10	0.00			
	3.0	3.1	3.1	3.1	3.10	0.00			
	5.0	3.2	3.2	3.5	3.30	0.17			
	7.0	3.2	3.0	3.0	3.07	0.12			
	10.0	3.5	3.5	3.5	3.50	0.00			
45.2	0.7	3.2	3.1	3.2	3.17	0.06	0.10	0.092	0.03
	3.0	3.2	3.1	3.4	3.23	0.15	0.09	0.083	0.14
	5.0	3.3	3.2	3.6	3.37	0.21	0.08	0.074	0.23
	7.0	3.3	3.0	3.0	3.10	0.17	0.08	0.074	0.32
	10.0	3.5	3.5	3.5	3.50	0.00	0.18	0.166	0.46
73.9	0.7	3.2	3.1	3.2	3.17	0.06	0.30	0.104	0.02
	3.0	3.2	3.1	3.2	3.17	0.06	0.28	0.097	0.09
	5.0	3.3	3.2	3.5	3.33	0.15	0.24	0.083	0.14
	7.0	3.3	3.0	3.0	3.10	0.17	0.18	0.062	0.20
	10.0	3.5	3.4	3.5	3.47	0.06	0.14	0.049	0.28
94.2	0.7	3.2	3.1	3.2	3.17	0.06	0.51	0.109	0.02
	3.0	3.2	3.1	3.1	3.13	0.06	0.48	0.102	0.07
	5.0	3.4	3.3	3.5	3.40	0.10	0.45	0.096	0.11
	7.0	3.3	3.0	3.0	3.10	0.17	0.34	0.073	0.16
	10.0	3.2	3.2	3.3	3.23	0.06	0.24	0.051	0.22
110.8	0.7	3.4	3.3	3.3	3.33	0.06	0.73	0.112	0.01
	3.0	3.4	3.3	3.2	3.30	0.10	0.68	0.105	0.06
	5.0	3.5	3.4	3.5	3.47	0.06	0.64	0.099	0.09
	7.0	3.3	3.1	3.0	3.13	0.15	0.50	0.077	0.13
	10.0	3.2	3.3	3.3	3.27	0.06	0.31	0.048	0.19

Table A. 9 - Dynamic Test Data - Spring 2, CV=±100V

Airspeed	Freq	Spring 2, CV=±100V (CR=1.292) (12/18/11)							
		P2P Deflection					Actual Load	Experimental Lift Coefficient	Reduced Frequency
		Run 1	Run 2	Run 3	Avg	St. Dev.			
ft/sec	Hz	deg	deg	deg	deg	deg	lb_f	--	--
0.0	12.0	2.1	2.1	2.1	2.11	0.02			
	14.0	2.3	2.2	2.2	2.23	0.06			
	16.0	2.5	2.5	2.5	2.50	0.00			
	18.0	3.3	3.1	3.2	3.20	0.10			
	20.0	3.7	3.8	3.8	3.77	0.06			
45.2	12.0	2.1	2.1	2.1	2.10	0.00	0.12	0.111	0.56
	14.0	2.3	2.3	2.3	2.30	0.00	0.13	0.120	0.65
	16.0	2.5	2.5	2.6	2.53	0.06	0.16	0.148	0.74
	18.0	3.1	3.1	3.1	3.11	0.02	0.22	0.203	0.83
	20.0	3.6	3.8	3.7	3.70	0.10	0.30	0.277	0.93
73.9	12.0	2.2	2.1	2.1	2.13	0.06	0.08	0.028	0.34
	14.0	2.3	2.3	2.3	2.30	0.00	0.11	0.038	0.40
	16.0	2.6	2.5	2.5	2.53	0.06	0.12	0.042	0.45
	18.0	3.0	3.0	3.0	3.00	0.00	0.18	0.062	0.51
	20.0	3.6	3.8	3.8	3.73	0.12	0.25	0.087	0.57
94.2	12.0	2.1	2.1	2.1	2.10	0.00	0.12	0.026	0.27
	14.0	2.3	2.3	2.3	2.30	0.00	0.10	0.021	0.31
	16.0	2.6	2.5	2.5	2.53	0.06	0.11	0.023	0.36
	18.0	3.0	3.0	2.9	2.97	0.06	0.14	0.030	0.40
	20.0	3.6	3.6	3.7	3.63	0.06	0.23	0.049	0.44
110.8	12.0	2.1	2.1	2.1	2.10	0.00	0.18	0.028	0.23
	14.0	2.3	2.3	2.3	2.30	0.00	0.13	0.020	0.26
	16.0	2.5	2.5	2.4	2.47	0.06	0.12	0.018	0.30
	18.0	2.9	2.9	2.9	2.90	0.00	0.13	0.020	0.34
	20.0	3.5	3.6	3.5	3.53	0.06	0.19	0.029	0.38

Table A. 10 - Dynamic Test Data - Spring 2, CV=±50V

Airspeed	Freq	P2P Deflection					Actual Load	Experimental Lift Coefficient	Reduced Frequency
		Run 1	Run 2	Run 3	Avg	St. Dev.			
ft/sec	Hz	deg	deg	deg	deg	deg	lb_f	--	--
0	12.0	1.1	1.2	1.2	1.17	0.06			
	14.0	1.5	1.4	1.5	1.47	0.06			
	15.0	2.0	2.0	1.9	1.97	0.06			
	16.0	2.5	2.5	2.5	2.50	0.00			
	17.0	3.0	2.9	2.9	2.93	0.06			
	18.0	3.7	3.5	3.6	3.60	0.10			
	19.0	3.3	3.6	3.9	3.60	0.30			
	20.0	2.8	2.9	3.0	2.90	0.10			
	21.0	2.6	3.6	3.8	3.33	0.64			
	22.0	3.0	2.9	2.8	2.90	0.10			
	23.0	2.0	2.1	2.1	2.07	0.06			
	24.0	1.2	1.2	1.3	1.23	0.06			
	26.0	1.0	1.0	0.9	0.97	0.06			
	28.0	0.8	0.7	0.7	0.73	0.06			
	30.0	0.6	0.5	0.5	0.53	0.06			
	35.0	0.3	0.3	0.3	0.30	0.00			
	40.0	0.2	0.1	0.1	0.13	0.06			
45.2	12.0	1.2	1.2	1.2	1.20	0.00	0.06	0.055	0.56
	14.0	1.4	1.4	1.5	1.43	0.06	0.09	0.083	0.65
	15.0	1.6	1.9	1.8	1.77	0.15	0.11	0.102	0.69
	16.0	2.3	2.5	2.2	2.33	0.15	0.15	0.139	0.74
	17.0	2.8	2.8	2.8	2.80	0.00	0.19	0.176	0.79
	18.0	3.0	3.2	3.2	3.13	0.12	0.23	0.213	0.83
	19.0	3.1	3.7	3.7	3.50	0.35	0.28	0.259	0.88
	20.0	2.9	3.0	3.1	3.00	0.10	0.29	0.268	0.93
	21.0	2.6	2.7	2.4	2.57	0.15	0.20	0.185	0.97
	22.0	2.7	2.5	2.6	2.60	0.10	0.14	0.129	1.02
	23.0	1.7	1.7	1.8	1.73	0.06	0.12	0.111	1.06
	24.0	1.2	1.2	1.2	1.20	0.00	0.10	0.092	1.11
	26.0	1.0	1.0	0.9	0.97	0.06	0.09	0.083	1.20
	28.0	0.7	0.7	0.7	0.70	0.00	0.09	0.083	1.30
	30.0	0.5	0.5	0.5	0.50	0.00	0.10	0.092	1.39
	35.0	0.3	0.3	0.3	0.30	0.00	0.10	0.092	1.62
	40.0	0.1	0.1	0.1	0.10	0.00	0.12	0.111	1.85
73.9	12.0	1.3	1.2	1.2	1.23	0.06	0.06	0.021	0.34
	14.0	1.5	1.4	1.4	1.43	0.06	0.07	0.024	0.40
	15.0	1.7	1.9	1.8	1.80	0.10	0.09	0.031	0.43
	16.0	2.2	2.2	2.2	2.20	0.00	0.11	0.038	0.45
	17.0	2.7	2.7	2.6	2.67	0.06	0.15	0.052	0.48
	18.0	3.0	3.0	2.9	2.97	0.06	0.19	0.066	0.51
	19.0	3.1	3.2	3.2	3.17	0.06	0.23	0.080	0.54
	20.0	2.9	3.2	3.2	3.10	0.17	0.26	0.090	0.57
	21.0	2.2	2.3	2.3	2.27	0.06	0.19	0.066	0.60
	22.0	2.5	2.5	2.3	2.43	0.12	0.11	0.038	0.62
	23.0	1.5	1.6	1.7	1.60	0.10	0.10	0.035	0.65
	24.0	1.3	1.3	1.3	1.30	0.00	0.10	0.035	0.68
	26.0	1.0	1.0	1.0	1.00	0.00	0.09	0.031	0.74
	28.0	0.8	0.8	0.7	0.77	0.06	0.08	0.028	0.79
	30.0	0.5	0.5	0.5	0.50	0.00	0.11	0.038	0.85
	35.0	0.3	0.3	0.3	0.30	0.00	0.09	0.031	0.99
	40.0	0.1	0.1	0.1	0.10	0.00	0.13	0.045	1.13
94.2	12.0	1.3	1.1	1.1	1.17	0.12	0.07	0.015	0.27
	14.0	1.5	1.3	1.3	1.37	0.12	0.08	0.017	0.31
	15.0	1.7	1.5	1.7	1.63	0.12	0.08	0.017	0.33
	16.0	1.9	2.0	1.9	1.93	0.06	0.09	0.019	0.36
	17.0	2.5	2.4	2.4	2.43	0.06	0.12	0.026	0.38
	18.0	2.9	2.8	2.7	2.80	0.10	0.15	0.032	0.40
	19.0	3.0	3.0	3.0	3.00	0.00	0.18	0.038	0.42
	20.0	2.9	3.0	3.1	3.00	0.10	0.21	0.045	0.44
	21.0	2.2	2.4	2.4	2.33	0.12	0.15	0.032	0.47
	22.0	2.5	2.2	2.2	2.30	0.17	0.08	0.017	0.49
	23.0	1.6	1.7	1.8	1.70	0.10	0.10	0.021	0.51
	24.0	1.4	1.3	1.5	1.40	0.10	0.10	0.021	0.53
	26.0	1.0	1.0	1.0	1.00	0.00	0.09	0.019	0.58
	28.0	0.7	0.8	0.8	0.77	0.06	0.08	0.017	0.62
	30.0	0.5	0.5	0.5	0.50	0.00	0.11	0.023	0.67
	35.0	0.3	0.3	0.3	0.30	0.00	0.09	0.019	0.78
	40.0	0.1	0.1	0.1	0.10	0.00	0.14	0.030	0.89
110.8	12.0	1.1	1.1	1.0	1.07	0.06	0.10	0.015	0.23
	14.0	1.4	1.2	1.1	1.23	0.15	0.10	0.015	0.26
	15.0	1.4	1.4	1.5	1.43	0.06	0.09	0.014	0.28
	16.0	1.7	1.7	1.8	1.73	0.06	0.09	0.014	0.30
	17.0	2.2	2.2	2.1	2.17	0.06	0.11	0.017	0.32
	18.0	2.7	2.5	2.3	2.50	0.20	0.13	0.020	0.34
	19.0	2.9	2.8	2.6	2.77	0.15	0.16	0.025	0.36
	20.0	2.8	2.9	2.8	2.83	0.06	0.19	0.029	0.38
	21.0	2.5	2.7	2.5	2.57	0.12	0.15	0.023	0.40
	22.0	2.7	2.4	2.3	2.47	0.21	0.07	0.011	0.42
	23.0	1.9	2.0	1.9	1.93	0.06	0.10	0.015	0.43
	24.0	1.4	1.7	1.7	1.60	0.17	0.10	0.015	0.45
	26.0	1.1	1.0	1.0	1.03	0.06	0.08	0.012	0.49
	28.0	0.9	0.8	0.8	0.83	0.06	0.08	0.012	0.53
	30.0	0.7	0.5	0.5	0.57	0.12	0.12	0.018	0.57
	35.0	0.3	0.3	0.3	0.30	0.00	0.08	0.012	0.66
	40.0	0.1	0.1	0.1	0.10	0.00	0.14	0.022	0.76

Table A. 11 - Dynamic Test Data - Spring 3, CV=±180V

Airspeed	Freq	P2P Deflection					Actual Load	Experimental Lift Coefficient	Reduced Frequency
		Run 1	Run 2	Run 3	Avg	St. Dev.			
ft/sec	Hz	deg	deg	deg	deg	deg	lb_f	--	--
0.0	0.7	4.2	4.6	4.7	4.50	0.26			
	3.0	4.3	4.6	4.7	4.53	0.21			
	5.0	4.5	4.9	5.0	4.80	0.26			
	7.0	4.4	4.7	4.7	4.60	0.17			
	10.0	4.5	4.9	4.8	4.73	0.21			
45.2	0.7	4.5	4.8	4.8	4.70	0.17	0.11	0.102	0.03
	3.0	4.4	4.8	4.7	4.63	0.21	0.10	0.092	0.14
	5.0	4.9	5.0	5.0	4.97	0.06	0.12	0.111	0.23
	7.0	4.6	4.6	4.5	4.57	0.06	0.14	0.129	0.32
	10.0	4.6	4.7	4.7	4.67	0.06	0.28	0.259	0.46
73.9	0.7	4.4	4.7	4.7	4.60	0.17	0.35	0.121	0.02
	3.0	4.1	4.7	4.7	4.50	0.35	0.34	0.118	0.09
	5.0	4.5	5.0	5.0	4.83	0.29	0.31	0.107	0.14
	7.0	4.4	4.4	4.3	4.37	0.06	0.20	0.069	0.20
	10.0	4.4	4.6	4.6	4.53	0.12	0.22	0.076	0.28
94.2	0.7	4.1	4.6	4.7	4.47	0.32	0.65	0.139	0.02
	3.0	4.1	4.5	4.5	4.37	0.23	0.62	0.132	0.07
	5.0	4.9	5.0	5.0	4.97	0.06	0.58	0.124	0.11
	7.0	4.5	4.5	4.4	4.47	0.06	0.42	0.090	0.16
	10.0	4.1	4.4	4.2	4.23	0.15	0.34	0.073	0.22
110.8	0.7	4.1	4.6	4.2	4.30	0.26	0.89	0.137	0.01
	3.0	4.0	4.1	4.1	4.07	0.06	0.85	0.131	0.06
	5.0	4.6	4.9	4.9	4.80	0.17	0.83	0.128	0.09
	7.0	4.5	4.5	4.5	4.50	0.00	0.64	0.099	0.13
	10.0	4.0	4.1	4.0	4.03	0.06	0.46	0.071	0.19

Table A. 12 - Dynamic Test Data - Spring 3, CV=±100V

Airspeed	Freq	P2P Deflection					Actual Load	Experimental Lift Coefficient	Reduced Frequency
		Run 1	Run 2	Run 3	Avg	St. Dev.			
ft/sec	Hz	deg	deg	deg	deg	deg	lb_f	--	--
0.0	12.0	3.3	3.1	3.1	3.17	0.12			
	14.0	3.7	3.6	3.6	3.63	0.06			
	16.0	4.3	4.2	4.4	4.30	0.10			
45.2	12.0	3.2	3.1	3.1	3.13	0.06	0.18	0.166	0.56
	14.0	3.6	3.5	3.5	3.53	0.06	0.23	0.213	0.65
	16.0	4.2	4.2	4.2	4.20	0.00	0.30	0.277	0.74
73.9	12.0	3.1	3.1	3.1	3.10	0.00	0.13	0.045	0.34
	14.0	3.2	3.3	3.2	3.23	0.06	0.16	0.055	0.40
	16.0	4.0	4.1	4.1	4.07	0.06	0.23	0.080	0.45
94.2	12.0	3.1	3.1	3.0	3.07	0.06	0.14	0.030	0.27
	14.0	3.2	3.2	3.2	3.20	0.00	0.14	0.030	0.31
	16.0	3.9	3.7	3.7	3.77	0.12	0.19	0.041	0.36
110.8	12.0	2.7	2.7	2.7	2.70	0.00	0.22	0.034	0.23
	14.0	3.1	3.1	3.1	3.10	0.00	0.17	0.026	0.26
	16.0	3.6	3.5	3.5	3.53	0.06	0.18	0.028	0.30

Table A. 13- Dynamic Test Data - Spring 3, CV=±50V

Airspeed	Freq	P2P Deflection					Actual Load	Experimental Lift Coefficient	Reduced Frequency
		Run 1	Run 2	Run 3	Avg	St. Dev.			
ft/sec	Hz	deg	deg	deg	deg	deg	lb_f	--	--
0.0	8.0	1.1	1.0	1.0	1.03	0.06			
	10.0	1.2	1.3	1.2	1.23	0.06			
	12.0	1.4	1.6	1.5	1.50	0.10			
	14.0	2.0	2.3	2.2	2.17	0.15			
	15.0	2.6	2.8	2.7	2.70	0.10			
	16.0	2.9	3.1	3.1	3.03	0.12			
	17.0	3.4	3.8	3.8	3.67	0.23			
	18.0	3.7	4.1	4.2	4.00	0.26			
	19.0	3.2	3.3	3.3	3.27	0.06			
	20.0	2.5	2.7	2.9	2.70	0.20			
	21.0	1.2	1.3	1.3	1.27	0.06			
	22.0	2.0	2.2	2.1	2.10	0.10			
	23.0	1.3	1.5	1.5	1.43	0.12			
	24.0	1.0	1.2	1.1	1.10	0.10			
	26.0	0.8	0.9	0.9	0.87	0.06			
	28.0	0.7	0.7	0.7	0.70	0.00			
	30.0	0.5	0.5	0.5	0.50	0.00			
	35.0	0.3	0.3	0.3	0.30	0.00			
	40.0	0.2	0.1	0.1	0.13	0.06			
45.2	8.0	1.1	1.2	1.0	1.10	0.10	0.05	0.046	0.37
	10.0	1.3	1.4	1.3	1.33	0.06	0.07	0.065	0.46
	12.0	1.5	1.6	1.6	1.57	0.06	0.09	0.083	0.56
	14.0	2.0	2.2	2.2	2.13	0.12	0.11	0.102	0.65
	15.0	2.5	2.8	2.6	2.63	0.15	0.15	0.139	0.69
	16.0	2.9	3.0	3.0	2.97	0.06	0.20	0.185	0.74
	17.0	3.3	3.4	3.4	3.37	0.06	0.24	0.222	0.79
	18.0	3.6	3.8	3.7	3.70	0.10	0.27	0.250	0.83
	19.0	3.0	3.2	3.3	3.17	0.15	0.26	0.240	0.88
	20.0	2.2	2.6	2.5	2.43	0.21	0.21	0.194	0.93
	21.0	1.3	1.3	1.4	1.33	0.06	0.13	0.120	0.97
	22.0	2.0	2.0	2.0	2.00	0.00	0.11	0.102	1.02
	23.0	1.3	1.4	1.4	1.37	0.06	0.11	0.102	1.06
	24.0	1.1	1.1	1.2	1.13	0.06	0.10	0.092	1.11
	26.0	0.9	0.9	0.9	0.90	0.00	0.08	0.074	1.20
	28.0	0.7	0.7	0.6	0.67	0.06	0.07	0.065	1.30
	30.0	0.5	0.5	0.5	0.50	0.00	0.07	0.065	1.39
	35.0	0.3	0.3	0.3	0.30	0.00	0.06	0.055	1.62
	40.0	0.2	0.1	0.1	0.13	0.06	0.12	0.111	1.85
73.9	8.0	1.0	1.0	1.0	1.00	0.00	0.05	0.017	0.23
	10.0	1.2	1.2	1.1	1.17	0.06	0.06	0.021	0.28
	12.0	1.5	1.4	1.4	1.43	0.06	0.06	0.021	0.34
	14.0	1.9	1.8	1.8	1.83	0.06	0.09	0.031	0.40
	15.0	2.3	2.3	2.3	2.30	0.00	0.11	0.038	0.43
	16.0	2.8	2.9	2.8	2.83	0.06	0.15	0.052	0.45
	17.0	3.0	3.1	3.1	3.07	0.06	0.19	0.066	0.48
	18.0	3.2	3.5	3.3	3.33	0.15	0.22	0.076	0.51
	19.0	3.1	3.4	3.3	3.27	0.15	0.22	0.076	0.54
	20.0	2.2	2.4	2.5	2.37	0.15	0.17	0.059	0.57
	21.0	1.6	1.6	1.6	1.60	0.00	0.15	0.052	0.60
	22.0	1.9	2.0	2.0	1.97	0.06	0.10	0.035	0.62
	23.0	1.5	1.5	1.5	1.50	0.00	0.12	0.042	0.65
	24.0	1.3	1.2	1.3	1.27	0.06	0.11	0.038	0.68
	26.0	0.9	0.9	0.9	0.90	0.00	0.09	0.031	0.74
	28.0	0.7	0.7	0.7	0.70	0.00	0.08	0.028	0.79
	30.0	0.5	0.5	0.5	0.50	0.00	0.07	0.024	0.85
	35.0	0.3	0.3	0.3	0.30	0.00	0.06	0.021	0.99
	40.0	0.1	0.1	0.1	0.10	0.00	0.12	0.042	1.13
94.2	8.0	0.9	0.9	0.9	0.90	0.00	0.08	0.017	0.18
	10.0	1.0	1.0	1.0	1.00	0.00	0.07	0.015	0.22
	12.0	1.2	1.2	1.2	1.20	0.00	0.06	0.013	0.27
	14.0	1.6	1.6	1.5	1.57	0.06	0.07	0.015	0.31
	15.0	1.8	2.0	1.9	1.90	0.10	0.08	0.017	0.33
	16.0	2.3	2.5	2.5	2.43	0.12	0.10	0.021	0.36
	17.0	2.8	3.0	2.9	2.90	0.10	0.14	0.030	0.38
	18.0	3.1	3.3	3.2	3.20	0.10	0.17	0.036	0.40
	19.0	3.0	3.2	3.1	3.10	0.10	0.18	0.038	0.42
	20.0	2.5	2.7	2.6	2.60	0.10	0.19	0.041	0.44
	21.0	2.0	2.1	2.1	2.07	0.06	0.13	0.028	0.47
	22.0	2.5	2.3	2.3	2.37	0.12	0.10	0.021	0.49
	23.0	1.6	1.6	1.8	1.67	0.12	0.12	0.026	0.51
	24.0	1.3	1.3	1.3	1.30	0.00	0.11	0.023	0.53
	26.0	0.9	1.0	1.0	0.97	0.06	0.09	0.019	0.58
	28.0	0.7	0.8	0.8	0.77	0.06	0.07	0.015	0.62
	30.0	0.5	0.5	0.5	0.50	0.00	0.08	0.017	0.67
	35.0	0.3	0.3	0.3	0.30	0.00	0.06	0.013	0.78
	40.0	0.1	0.1	0.1	0.10	0.00	0.13	0.028	0.89
110.8	8.0	0.9	0.9	0.9	0.90	0.00	0.13	0.020	0.15
	10.0	1.0	1.0	1.0	1.00	0.00	0.10	0.015	0.19
	12.0	1.1	1.1	1.1	1.10	0.00	0.08	0.012	0.23
	14.0	1.3	1.2	1.2	1.23	0.06	0.07	0.011	0.26
	15.0	1.5	1.4	1.4	1.43	0.06	0.07	0.011	0.28
	16.0	1.7	1.9	1.8	1.80	0.10	0.08	0.012	0.30
	17.0	2.3	2.4	2.3	2.33	0.06	0.10	0.015	0.32
	18.0	2.8	2.9	2.8	2.83	0.06	0.14	0.022	0.34
	19.0	3.0	3.1	3.0	3.03	0.06	0.15	0.023	0.36
	20.0	2.7	2.8	2.6	2.70	0.10	0.17	0.026	0.38
	21.0	2.6	2.5	2.5	2.53	0.06	0.12	0.018	0.40
	22.0	2.3	2.5	2.4	2.40	0.10	0.11	0.017	0.42
	23.0	1.7	1.7	1.7	1.70	0.00	0.11	0.017	0.43
	24.0	1.3	1.5	1.5	1.43	0.12	0.11	0.017	0.45
	26.0	1.1	1.0	1.0	1.03	0.06	0.09	0.014	0.49
	28.0	0.9	0.8	0.8	0.83	0.06	0.07	0.011	0.53
	30.0	0.6	0.5	0.5	0.53	0.06	0.07	0.011	0.57
	35.0	0.4	0.3	0.3	0.33	0.06	0.06	0.009	0.66
	40.0	0.2	0.2	0.1	0.17	0.06	0.12	0.018	0.76

A.4 Aerodynamic Damping Data

Table A. 14 - Aerodynamic Damping - No Spring, CV=±20V

Airspeed	Freq	No Spring, CV=±20V (12/19/11)											
		P2P Deflection					Normalized Deflection	Frequency Ratio	Reduced Frequency	Total Damping Ratio	Aerodynamic Damping Ratio	Structural Damping Coefficient	Aerodynamic Damping Coefficient
		Run 1	Run 2	Run 3	Avg	St. Dev.	Avg	r		ζ_{tot}	ζ_{air}	c_{vane}	c_{aero} (C_{Mq})
ft/sec	Hz	deg	deg	deg	deg	deg	--	--	--	--	--	(ft lb$_f$)/(rad/s)	(ft lb$_f$)/(rad/s)
0.0	22.0	0.2	0.2	0.1	0.17	0.06	1.00	0.72		0.608		0.214	
	25.0	0.2	0.3	0.3	0.27	0.06	1.60	0.82		0.325		0.114	
	27.0	0.3	0.4	0.4	0.37	0.06	2.20	0.89		0.227		0.080	
	28.0	0.5	0.6	0.6	0.57	0.06	3.40	0.92		0.137		0.048	
	29.0	2.0	2.1	2.0	2.03	0.06	12.20	0.95		0.019		0.007	
	30.0	1.9	2.0	2.0	1.97	0.06	11.80	0.99		0.041		0.014	
	31.0	1.2	1.2	1.2	1.20	0.00	7.20	1.02		0.065		0.023	
	32.0	1.0	1.0	0.9	0.97	0.06	5.80	1.05		0.064		0.022	
	33.0	0.8	0.9	0.7	0.81	0.09	4.86	1.09		0.047		0.017	
	34.0	0.6	0.6	0.6	0.60	0.00	3.60	1.12		0.053		0.019	
	35.0	0.5	0.5	0.4	0.47	0.06	2.80	1.15		0.064		0.022	
	36.0	0.3	0.3	0.3	0.30	0.00	1.80	1.18		0.162		0.057	
	38.0	0.2	0.2	0.1	0.17	0.06	1.00	1.25		0.331		0.116	
45.2	22.0	0.3	0.2	0.1	0.20	0.10	1.00	0.72	1.02	0.608	0.0000	0.214	0.000
	25.0	0.3	0.3	0.2	0.27	0.06	1.33	0.82	1.16	0.411	0.0863	0.145	0.030
	27.0	0.4	0.5	0.4	0.43	0.06	2.17	0.89	1.25	0.231	0.0044	0.081	0.002
	28.0	0.7	0.7	0.6	0.67	0.06	3.33	0.92	1.30	0.141	0.0037	0.049	0.001
	29.0	1.0	1.2	1.1	1.10	0.10	5.50	0.95	1.34	0.083	0.0633	0.029	0.022
	30.0	1.3	1.5	1.5	1.43	0.12	7.17	0.99	1.39	0.069	0.0286	0.024	0.010
	31.0	1.1	1.1	1.1	1.10	0.00	5.50	1.02	1.44	0.087	0.0217	0.031	0.008
	32.0	1.0	0.9	0.9	0.93	0.06	4.67	1.05	1.48	0.088	0.0241	0.031	0.008
	33.0	0.7	0.7	0.7	0.70	0.00	3.50	1.09	1.53	0.103	0.0556	0.036	0.020
	34.0	0.7	0.6	0.6	0.63	0.06	3.17	1.12	1.57	0.086	0.0324	0.030	0.011
	35.0	0.6	0.5	0.5	0.53	0.06	2.67	1.15	1.62	0.081	0.0170	0.028	0.006
	36.0	0.4	0.4	0.4	0.40	0.00	2.00	1.18	1.67	0.125	-0.0364	0.044	-0.013
	38.0	0.2	0.2	0.1	0.17	0.06	0.83	1.25	1.76	0.424	0.0933	0.149	0.033
73.9	22.0	0.3	0.2	0.1	0.20	0.10	1.00	0.72	0.62	0.608	0.0000	0.214	0.000
	25.0	0.4	0.3	0.3	0.33	0.06	1.67	0.82	0.71	0.307	-0.0179	0.108	-0.006
	27.0	0.6	0.5	0.5	0.53	0.06	2.67	0.89	0.77	0.174	-0.0521	0.061	-0.018
	28.0	0.8	0.7	0.6	0.70	0.10	3.50	0.92	0.79	0.131	-0.0054	0.046	-0.002
	29.0	1.0	1.0	1.0	1.00	0.00	5.00	0.95	0.82	0.094	0.0742	0.033	0.026
	30.0	1.1	1.1	1.1	1.10	0.00	5.50	0.99	0.85	0.091	0.0503	0.032	0.018
	31.0	1.0	1.0	1.0	1.00	0.00	5.00	1.02	0.88	0.096	0.0309	0.034	0.011
	32.0	0.9	0.9	0.8	0.87	0.06	4.33	1.05	0.91	0.097	0.0330	0.034	0.012
	33.0	0.8	0.7	0.6	0.70	0.10	3.50	1.09	0.94	0.103	0.0556	0.036	0.020
	34.0	0.6	0.6	0.5	0.57	0.06	2.83	1.12	0.96	0.111	0.0577	0.039	0.020
	35.0	0.4	0.4	0.4	0.40	0.00	2.00	1.15	0.99	0.165	0.1010	0.058	0.036
	36.0	0.3	0.3	0.3	0.30	0.00	1.50	1.18	1.02	0.224	0.0627	0.079	0.022
	38.0	0.2	0.2	0.1	0.17	0.06	0.83	1.25	1.08	0.424	0.0933	0.149	0.033
94.2	22.0	0.2	0.2	0.2	0.20	0.00	1.00	0.72	0.49	0.608	0.0000	0.214	0.000
	25.0	0.3	0.3	0.3	0.30	0.00	1.50	0.82	0.56	0.354	0.0293	0.125	0.010
	27.0	0.7	0.5	0.5	0.57	0.12	2.83	0.89	0.60	0.159	-0.0674	0.056	-0.024
	28.0	0.8	0.8	0.6	0.73	0.12	3.67	0.92	0.62	0.123	-0.0138	0.043	-0.005
	29.0	1.0	1.0	0.9	0.97	0.06	4.83	0.95	0.64	0.098	0.0782	0.034	0.027
	30.0	1.1	1.1	1.0	1.07	0.06	5.33	0.99	0.67	0.094	0.0532	0.033	0.019
	31.0	1.0	1.0	0.9	0.97	0.06	4.83	1.02	0.69	0.100	0.0343	0.035	0.012
	32.0	0.8	0.8	0.7	0.77	0.06	3.83	1.05	0.71	0.113	0.0490	0.040	0.017
	33.0	0.7	0.6	0.6	0.63	0.06	3.17	1.09	0.73	0.120	0.0728	0.042	0.026
	34.0	0.5	0.4	0.5	0.47	0.06	2.33	1.12	0.76	0.155	0.1020	0.055	0.036
	35.0	0.4	0.3	0.3	0.33	0.06	1.67	1.15	0.78	0.219	0.1551	0.077	0.055
	36.0	0.3	0.2	0.2	0.23	0.06	1.17	1.18	0.80	0.320	0.1578	0.112	0.055
	38.0	0.2	0.1	0.1	0.13	0.06	0.67	1.25	0.85	0.556	0.2255	0.195	0.079
110.8	22.0	0.2	0.2	0.2	0.20	0.00	1.00	0.72	0.42	0.608	0.0000	0.214	0.000
	25.0	0.4	0.3	0.3	0.33	0.06	1.67	0.82	0.47	0.307	-0.0179	0.108	-0.006
	27.0	0.6	0.5	0.5	0.53	0.06	2.67	0.89	0.51	0.174	-0.0521	0.061	-0.018
	28.0	0.8	0.7	0.7	0.73	0.06	3.67	0.92	0.53	0.123	-0.0138	0.043	-0.005
	29.0	0.9	0.8	0.8	0.83	0.06	4.17	0.95	0.55	0.117	0.0972	0.041	0.034
	30.0	1.0	0.9	0.9	0.93	0.06	4.67	0.99	0.57	0.108	0.0669	0.038	0.024
	31.0	0.9	0.9	0.7	0.83	0.12	4.17	1.02	0.59	0.116	0.0508	0.041	0.018
	32.0	0.7	0.7	0.6	0.67	0.06	3.33	1.05	0.60	0.133	0.0691	0.047	0.024
	33.0	0.5	0.5	0.5	0.50	0.00	2.50	1.09	0.62	0.165	0.1177	0.058	0.041
	34.0	0.4	0.3	0.3	0.33	0.06	1.67	1.12	0.64	0.244	0.1903	0.086	0.067
	35.0	0.3	0.2	0.2	0.23	0.06	1.17	1.15	0.66	0.344	0.2806	0.121	0.099
	36.0	0.2	0.1	0.1	0.13	0.06	0.67	1.18	0.68	0.610	0.4484	0.214	0.158
	38.0	0.1	0.1	0.1	0.10	0.00	0.50	1.25	0.72	0.768	0.4370	0.270	0.154

Table A. 15 - Aerodynamic Damping - No Spring, CV=±50V

Airspeed	Freq	No Spring, CV=±50V (12/29/11)											
		P2P Deflection					Normalized Deflection	Frequency Ratio	Reduced Frequency	Total Damping Ratio	Aerodynamic Damping Ratio	Structural Damping Coefficient	Aerodynamic Damping Coefficient
		Run 1	Run 2	Run 3	Avg	St. Dev.	Avg	r		ζ_{tot}	ζ_{air}	c_{vane}	c_{aero} (C_{Mq})
ft/sec	Hz	deg	deg	deg	deg	deg	--	--	--	--	--	(ft lb_f)/(rad/s)	(ft lb_f)/(rad/s)
0.0	22.0	0.8	0.6	0.7	0.70	0.10	1.00	0.72		0.608		0.214	
	25.0	1.0	0.9	1.0	0.97	0.06	1.38	0.82		0.394		0.138	
	27.0	1.7	1.7	1.7	1.70	0.00	2.43	0.89		0.199		0.070	
	28.0	2.6	2.5	2.5	2.53	0.06	3.62	0.92		0.125		0.044	
	29.0	4.0	4.0	4.0	4.00	0.00	5.71	0.95		0.079		0.028	
	30.0	3.7	3.7	3.8	3.73	0.06	5.33	0.99		0.094		0.033	
	31.0	2.2	2.3	2.4	2.30	0.10	3.29	1.02		0.148		0.052	
	32.0	1.7	1.6	1.7	1.67	0.06	2.38	1.05		0.193		0.068	
	33.0	1.1	1.1	1.3	1.17	0.12	1.67	1.09		0.264		0.093	
	34.0	1.0	0.9	0.7	0.87	0.15	1.24	1.12		0.343		0.121	
	36.0	0.5	0.5	0.5	0.50	0.00	0.71	1.18		0.566		0.199	
	38.0	0.4	0.4	0.4	0.40	0.00	0.57	1.25		0.663		0.233	
	40.0	0.5	0.6	0.5	0.53	0.06	0.76	1.32		0.414		0.146	
	45.0	0.2	0.2	0.2	0.20	0.00	0.29	1.48		1.112		0.391	
45.2	22.0	0.8	0.7	0.7	0.73	0.06	1.00	0.72	1.02	0.608	0.0000	0.214	0.000
	25.0	1.0	1.0	1.0	1.00	0.00	1.36	0.82	1.16	0.400	0.0062	0.141	0.002
	27.0	1.7	1.7	1.7	1.70	0.00	2.32	0.89	1.25	0.212	0.0128	0.074	0.004
	28.0	2.3	2.3	2.4	2.33	0.06	3.18	0.92	1.30	0.149	0.0240	0.053	0.008
	29.0	3.1	3.3	3.3	3.23	0.12	4.41	0.95	1.34	0.109	0.0305	0.038	0.011
	30.0	3.0	3.3	3.3	3.20	0.17	4.36	0.99	1.39	0.115	0.0213	0.041	0.007
	31.0	2.1	2.2	2.3	2.20	0.10	3.00	1.02	1.44	0.162	0.0143	0.057	0.005
	32.0	1.6	1.5	1.6	1.57	0.06	2.14	1.05	1.48	0.216	0.0236	0.076	0.008
	33.0	1.2	1.2	1.3	1.23	0.06	1.68	1.09	1.53	0.261	-0.0026	0.092	-0.001
	34.0	0.9	0.8	0.7	0.80	0.10	1.09	1.12	1.57	0.394	0.0509	0.139	0.018
	36.0	0.6	0.5	0.5	0.53	0.06	0.73	1.18	1.67	0.555	-0.0110	0.195	-0.004
	38.0	0.4	0.4	0.4	0.40	0.00	0.55	1.25	1.76	0.698	0.0351	0.245	0.012
	40.0	0.5	0.5	0.5	0.50	0.00	0.68	1.32	1.85	0.483	0.0690	0.170	0.024
	45.0	0.2	0.2	0.2	0.20	0.00	0.27	1.48	2.08	1.171	0.0597	0.412	0.021
73.9	22.0	0.8	0.7	0.7	0.73	0.06	1.00	0.72	0.62	0.608	0.0000	0.214	0.000
	25.0	1.0	1.0	1.0	1.00	0.00	1.36	0.82	0.71	0.400	0.0062	0.141	0.002
	27.0	1.6	1.7	1.7	1.67	0.06	2.27	0.89	0.77	0.217	0.0183	0.076	0.006
	28.0	2.0	2.1	2.2	2.10	0.10	2.86	0.92	0.79	0.171	0.0454	0.060	0.016
	29.0	2.5	2.5	2.6	2.53	0.06	3.45	0.95	0.82	0.144	0.0655	0.051	0.023
	30.0	2.5	2.6	2.6	2.57	0.06	3.50	0.99	0.85	0.144	0.0501	0.051	0.018
	31.0	1.9	1.9	2.0	1.93	0.06	2.64	1.02	0.88	0.185	0.0370	0.065	0.013
	32.0	1.3	1.5	1.4	1.40	0.10	1.91	1.05	0.91	0.243	0.0507	0.086	0.018
	33.0	1.0	1.0	1.2	1.07	0.12	1.45	1.09	0.94	0.306	0.0420	0.107	0.015
	34.0	0.9	0.9	0.7	0.83	0.12	1.14	1.12	0.96	0.377	0.0339	0.133	0.012
	36.0	0.5	0.5	0.5	0.50	0.00	0.68	1.18	1.02	0.596	0.0293	0.209	0.010
	38.0	0.4	0.4	0.4	0.40	0.00	0.55	1.25	1.08	0.698	0.0351	0.245	0.012
	40.0	0.5	0.5	0.5	0.50	0.00	0.68	1.32	1.13	0.483	0.0690	0.170	0.024
	45.0	0.2	0.2	0.2	0.20	0.00	0.27	1.48	1.28	1.171	0.0597	0.412	0.021
94.2	22.0	0.8	0.8	0.7	0.77	0.06	1.00	0.72	0.49	0.608	0.0000	0.214	0.000
	25.0	1.0	1.0	1.0	1.00	0.00	1.30	0.82	0.56	0.423	0.0287	0.149	0.010
	27.0	1.7	1.7	1.6	1.67	0.06	2.17	0.89	0.60	0.230	0.0311	0.081	0.011
	28.0	2.0	2.0	2.0	2.00	0.00	2.61	0.92	0.62	0.191	0.0657	0.067	0.023
	29.0	2.2	2.2	2.5	2.30	0.17	3.00	0.95	0.64	0.168	0.0896	0.059	0.031
	30.0	2.2	2.3	2.4	2.30	0.10	3.00	0.99	0.67	0.168	0.0743	0.059	0.026
	31.0	1.8	1.8	1.8	1.80	0.00	2.35	1.02	0.69	0.208	0.0600	0.073	0.021
	32.0	1.3	1.4	1.4	1.37	0.06	1.78	1.05	0.71	0.261	0.0687	0.092	0.024
	33.0	1.0	1.0	1.1	1.03	0.06	1.35	1.09	0.73	0.332	0.0678	0.117	0.024
	34.0	0.9	0.8	0.7	0.80	0.10	1.04	1.12	0.76	0.413	0.0703	0.145	0.025
	36.0	0.5	0.5	0.5	0.50	0.00	0.65	1.18	0.80	0.625	0.0585	0.220	0.021
	38.0	0.4	0.4	0.4	0.40	0.00	0.52	1.25	0.85	0.733	0.0701	0.258	0.025
	40.0	0.5	0.5	0.5	0.50	0.00	0.65	1.32	0.89	0.512	0.0980	0.180	0.034
	45.0	0.2	0.2	0.2	0.20	0.00	0.26	1.48	1.00	1.231	0.1191	0.433	0.042
110.8	22.0	0.8	0.8	0.7	0.77	0.06	1.00	0.72	0.42	0.608	0.0000	0.214	0.000
	25.0	1.1	1.0	1.1	1.07	0.06	1.39	0.82	0.47	0.390	-0.0037	0.137	-0.001
	27.0	1.6	1.5	1.6	1.57	0.06	2.04	0.89	0.51	0.249	0.0495	0.087	0.017
	28.0	1.9	1.9	1.8	1.87	0.06	2.43	0.92	0.53	0.207	0.0818	0.073	0.029
	29.0	2.1	2.1	2.2	2.13	0.06	2.78	0.95	0.55	0.182	0.1037	0.064	0.036
	30.0	2.0	2.1	2.2	2.10	0.10	2.74	0.99	0.57	0.184	0.0904	0.065	0.032
	31.0	1.7	1.7	1.7	1.70	0.00	2.22	1.02	0.59	0.220	0.0723	0.077	0.025
	32.0	1.3	1.4	1.3	1.33	0.06	1.74	1.05	0.60	0.268	0.0755	0.094	0.027
	33.0	1.0	1.0	1.1	1.03	0.06	1.35	1.09	0.62	0.332	0.0678	0.117	0.024
	34.0	0.9	0.9	0.7	0.83	0.12	1.09	1.12	0.64	0.396	0.0525	0.139	0.018
	36.0	0.5	0.5	0.5	0.50	0.00	0.65	1.18	0.68	0.625	0.0585	0.220	0.021
	38.0	0.4	0.4	0.4	0.40	0.00	0.52	1.25	0.72	0.733	0.0701	0.258	0.025
	40.0	0.5	0.5	0.5	0.50	0.00	0.65	1.32	0.76	0.512	0.0980	0.180	0.034
	45.0	0.2	0.2	0.2	0.20	0.00	0.26	1.48	0.85	1.231	0.1191	0.433	0.042

Table A. 16 - Aerodynamic Damping – Spring 1, CV=±50V

Airspeed	Freq	Spring 1, CV=±50V, (CR=1.637) (12/28/11)											
		P2P Deflection					Normalized Deflection	Frequency Ratio	Reduced Frequency	Total Damping Ratio	Aerodynamic Damping Ratio	Structural Damping Coefficient	Aerodynamic Damping Coefficient
		Run 1	Run 2	Run 3	Avg	St. Dev.	Avg	r		ζ_{tot}	ζ_{air}	c_{vane}	c_{aero} (C_{Mq})
ft/sec	Hz	deg	deg	deg	deg	deg	--	--	--	--	--	(ft lb$_f$)/(rad/s)	(ft lb$_f$)/(rad/s)
0.0	10.0	0.5	0.4	0.4	0.43	0.06	1.00	0.42		0.676		0.187	
	12.0	0.6	0.5	0.5	0.53	0.06	1.23	0.50		0.313		0.087	
	14.0	0.7	0.6	0.6	0.63	0.06	1.46	0.58		0.155		0.043	
	16.0	0.9	0.7	0.7	0.77	0.12	1.77	0.67		0.078		0.022	
	17.0	1.1	0.8	0.8	0.90	0.17	2.08	0.71		0.091		0.025	
	18.0	1.4	0.9	0.8	1.03	0.32	2.38	0.75		0.083		0.023	
	19.0	1.8	1.0	0.9	1.23	0.49	2.85	0.79		0.080		0.022	
	20.0	2.0	1.2	1.0	1.40	0.53	3.23	0.83		0.030		0.008	
	21.0	2.6	1.5	1.3	1.80	0.70	4.15	0.88		0.031		0.009	
	22.0	3.3	1.9	1.7	2.30	0.87	5.31	0.92		0.055		0.015	
	23.0	2.7	3.7	3.9	3.43	0.64	7.92	0.96		0.050		0.014	
	24.0	2.1	3.0	3.3	2.80	0.62	6.46	1.00		0.077		0.021	
	26.0	1.7	2.2	2.2	2.03	0.29	4.69	1.08		0.057		0.016	
	28.0	1.0	1.3	1.6	1.30	0.30	3.00	1.17		0.060		0.017	
	30.0	0.6	0.7	0.8	0.70	0.10	1.62	1.25		0.103		0.029	
	35.0	0.4	0.4	0.5	0.43	0.06	1.00	1.46		0.178		0.049	
	40.0	0.2	0.2	0.3	0.23	0.06	0.54	1.67		0.161		0.045	
45.2	10.0	0.4	0.4	0.4	0.40	0.00	1.00	0.42	0.46	0.676	0.0000	0.187	0.000
	12.0	0.5	0.5	0.5	0.50	0.00	1.25	0.50	0.56	0.278	-0.0341	0.077	-0.009
	14.0	0.6	0.6	0.6	0.60	0.00	1.50	0.58	0.65	0.082	-0.0732	0.023	-0.020
	16.0	0.8	0.7	0.7	0.73	0.06	1.83	0.67	0.74	0.079	0.0010	0.022	0.000
	17.0	0.9	0.7	0.8	0.80	0.10	2.00	0.71	0.79	0.029	-0.0611	0.008	-0.017
	18.0	1.1	0.8	0.8	0.90	0.17	2.25	0.75	0.83	0.052	-0.0310	0.014	-0.009
	19.0	1.3	0.9	0.9	1.03	0.23	2.58	0.79	0.88	0.065	-0.0148	0.018	-0.004
	20.0	1.6	1.0	1.0	1.20	0.35	3.00	0.83	0.93	0.080	0.0503	0.022	0.014
	21.0	1.9	1.3	1.3	1.50	0.35	3.75	0.88	0.97	0.073	0.0413	0.020	0.011
	22.0	2.7	1.6	1.6	1.97	0.64	4.92	0.92	1.02	0.069	0.0142	0.019	0.004
	23.0	2.8	2.0	1.9	2.23	0.49	5.58	0.96	1.06	0.083	0.0329	0.023	0.009
	24.0	2.2	2.9	3.1	2.73	0.47	6.83	1.00	1.11	0.073	-0.0042	0.020	-0.001
	26.0	1.7	2.0	2.0	1.90	0.17	4.75	1.08	1.20	0.055	-0.0021	0.015	-0.001
	28.0	1.2	1.5	1.6	1.43	0.21	3.58	1.17	1.30	0.098	0.0387	0.027	0.011
	30.0	0.6	0.8	1.0	0.80	0.20	2.00	1.25	1.39	0.103	-0.0003	0.029	0.000
	35.0	0.4	0.4	0.5	0.43	0.06	1.08	1.46	1.62	0.222	0.0435	0.061	0.012
	40.0	0.2	0.2	0.2	0.20	0.00	0.50	1.67	1.85	0.275	0.1137	0.076	0.032
73.9	10.0	0.4	0.4	0.3	0.37	0.06	1.00	0.42	0.28	0.676	0.0000	0.187	0.000
	12.0	0.5	0.5	0.4	0.47	0.06	1.27	0.50	0.34	0.234	-0.0783	0.065	-0.022
	14.0	0.6	0.5	0.5	0.53	0.06	1.45	0.58	0.40	0.166	0.0103	0.046	0.003
	16.0	0.7	0.6	0.6	0.63	0.06	1.73	0.67	0.45	0.122	0.0441	0.034	0.012
	17.0	0.7	0.6	0.6	0.63	0.06	1.73	0.71	0.48	0.208	0.1176	0.058	0.033
	18.0	0.9	0.7	0.6	0.73	0.15	2.00	0.75	0.51	0.161	0.0782	0.045	0.022
	19.0	1.1	0.8	0.7	0.87	0.21	2.36	0.79	0.54	0.126	0.0462	0.035	0.013
	20.0	1.3	0.9	0.8	1.00	0.26	2.73	0.83	0.57	0.122	0.0920	0.034	0.026
	21.0	1.5	1.3	1.1	1.30	0.20	3.55	0.88	0.60	0.090	0.0582	0.025	0.016
	22.0	1.8	1.5	1.3	1.53	0.25	4.18	0.92	0.62	0.097	0.0426	0.027	0.012
	23.0	2.3	1.7	1.5	1.83	0.42	5.00	0.96	0.65	0.095	0.0450	0.026	0.012
	24.0	2.3	2.2	1.9	2.13	0.21	5.82	1.00	0.68	0.086	0.0086	0.024	0.002
	26.0	1.8	2.1	2.2	2.03	0.21	5.55	1.08	0.74	0.023	-0.0345	0.006	-0.010
	28.0	1.4	1.6	1.7	1.57	0.15	4.27	1.17	0.79	0.118	0.0583	0.033	0.016
	30.0	0.7	1.0	1.0	0.90	0.17	2.45	1.25	0.85	0.155	0.0517	0.043	0.014
	35.0	0.4	0.4	0.4	0.40	0.00	1.09	1.46	0.99	0.225	0.0466	0.062	0.013
	40.0	0.2	0.2	0.2	0.20	0.00	0.55	1.67	1.13	0.134	-0.0268	0.037	-0.007
94.2	10.0	0.2	0.3	0.3	0.27	0.06	1.00	0.42	0.22	0.676	0.0000	0.187	0.000
	12.0	0.4	0.4	0.4	0.40	0.00	1.50	0.50	0.27	0.344	0.0311	0.095	0.009
	14.0	0.4	0.4	0.4	0.40	0.00	1.50	0.58	0.31	0.082	-0.0732	0.023	-0.020
	16.0	0.5	0.5	0.5	0.50	0.00	1.88	0.67	0.36	0.117	0.0386	0.032	0.011
	17.0	0.6	0.5	0.5	0.53	0.06	2.00	0.71	0.38	0.029	-0.0611	0.008	-0.017
	18.0	0.7	0.6	0.6	0.63	0.06	2.38	0.75	0.40	0.079	-0.0039	0.022	-0.001
	19.0	0.9	0.7	0.7	0.77	0.12	2.88	0.79	0.42	0.086	0.0060	0.024	0.002
	20.0	1.1	0.9	0.8	0.93	0.15	3.50	0.83	0.44	0.065	0.0353	0.018	0.010
	21.0	1.2	1.0	1.0	1.07	0.12	4.00	0.88	0.47	0.050	0.0183	0.014	0.005
	22.0	1.4	1.2	1.1	1.23	0.15	4.63	0.92	0.49	0.079	0.0250	0.022	0.007
	23.0	1.6	1.3	1.3	1.40	0.17	5.25	0.96	0.51	0.090	0.0396	0.025	0.011
	24.0	2.0	1.5	1.4	1.63	0.32	6.13	1.00	0.53	0.082	0.0043	0.023	0.001
	26.0	1.9	2.0	2.2	2.03	0.15	7.63	1.08	0.58	0.053	-0.0045	0.015	-0.001
	28.0	1.4	1.5	1.6	1.50	0.10	5.63	1.17	0.62	0.135	0.0752	0.037	0.021
	30.0	0.9	1.0	1.1	1.00	0.10	3.75	1.25	0.67	0.198	0.0947	0.055	0.026
	35.0	0.5	0.5	0.5	0.50	0.00	1.88	1.46	0.78	0.340	0.1623	0.094	0.045
	40.0	0.2	0.2	0.3	0.23	0.06	0.88	1.67	0.89	0.409	0.2474	0.113	0.069
110.8	10.0	0.4	0.3	0.3	0.33	0.06	1.00	0.42	0.19	0.676	0.0000	0.187	0.000
	12.0	0.5	0.5	0.5	0.50	0.00	1.50	0.50	0.23	0.344	0.0311	0.095	0.009
	14.0	0.6	0.6	0.6	0.60	0.00	1.80	0.58	0.26	0.305	0.1495	0.085	0.041
	16.0	0.7	0.6	0.6	0.63	0.06	1.90	0.67	0.30	0.133	0.0553	0.037	0.015
	17.0	0.7	0.7	0.7	0.70	0.00	2.10	0.71	0.32	0.104	0.0130	0.029	0.004
	18.0	0.8	0.7	0.7	0.73	0.06	2.20	0.75	0.34	0.082	-0.0009	0.023	0.000
	19.0	0.9	0.8	0.8	0.83	0.06	2.50	0.79	0.36	0.091	0.0112	0.025	0.003
	20.0	0.9	0.9	0.9	0.90	0.00	2.70	0.83	0.38	0.126	0.0959	0.035	0.027
	21.0	1.0	1.0	0.9	0.97	0.06	2.90	0.88	0.40	0.145	0.1131	0.040	0.031
	22.0	1.0	1.0	1.0	1.00	0.00	3.00	0.92	0.42	0.160	0.1051	0.044	0.029
	23.0	1.1	1.0	1.0	1.03	0.06	3.10	0.96	0.43	0.163	0.1126	0.045	0.031
	24.0	1.3	1.1	1.1	1.17	0.12	3.50	1.00	0.45	0.143	0.0655	0.040	0.018
	26.0	1.9	1.7	1.8	1.80	0.10	5.40	1.08	0.49	0.030	-0.0273	0.008	-0.008
	28.0	1.3	1.6	1.6	1.50	0.17	4.50	1.17	0.53	0.122	0.0625	0.034	0.017
	30.0	1.0	1.1	1.1	1.07	0.06	3.20	1.25	0.57	0.187	0.0837	0.052	0.023
	35.0	0.6	0.6	0.7	0.63	0.06	1.90	1.46	0.66	0.342	0.1636	0.095	0.045
	40.0	0.4	0.4	0.3	0.37	0.06	1.10	1.67	0.76	0.458	0.2972	0.127	0.082

Table A. 17 - Aerodynamic Damping – Spring 2, CV=±50V

Airspeed	Freq	Spring 2, CV=±50V (CR=1.292) (12/26/11)											
		P2P Deflection					Normalized Deflection	Frequency Ratio	Reduced Frequency	Total Damping Ratio	Aerodynamic Damping Ratio	Structural Damping Coefficient	Aerodynamic Damping Coefficient
		Run 1	Run 2	Run 3	Avg	St. Dev.	Avg	r		ζ_{tot}	ζ_{air}	c_{vane}	c_{aero} (C_{Mq})
ft/sec	Hz	deg	deg	deg	deg	deg	--	--	--	--	--	(ft lb$_f$)/(rad/s)	(ft lb$_f$)/(rad/s)
0	12.0	1.1	1.2	1.2	1.17	0.06	1.00	0.56		0.649		0.161	
	14.0	1.5	1.4	1.5	1.47	0.06	1.26	0.65		0.422		0.105	
	15.0	2.0	2.0	1.9	1.97	0.06	1.69	0.70		0.218		0.054	
	16.0	2.5	2.5	2.5	2.50	0.00	2.14	0.75		0.102		0.025	
	17.0	3.0	2.9	2.9	2.93	0.06	2.51	0.79		0.094		0.023	
	18.0	3.7	3.5	3.6	3.60	0.10	3.09	0.84		0.083		0.021	
	19.0	3.3	3.6	3.9	3.60	0.30	3.09	0.89		0.138		0.034	
	20.0	2.8	2.9	3.0	2.90	0.10	2.49	0.93		0.204		0.051	
	21.0	2.6	3.6	3.8	3.33	0.64	2.86	0.98		0.177		0.044	
	22.0	3.0	2.9	2.8	2.90	0.10	2.49	1.03		0.194		0.048	
	23.0	2.0	2.1	2.1	2.07	0.06	1.77	1.07		0.253		0.062	
	24.0	1.2	1.2	1.3	1.23	0.06	1.06	1.12		0.406		0.100	
	26.0	1.0	1.0	0.9	0.97	0.06	0.83	1.21		0.456		0.113	
	28.0	0.8	0.7	0.7	0.73	0.06	0.63	1.31		0.544		0.135	
	30.0	0.6	0.5	0.5	0.53	0.06	0.46	1.40		0.700		0.173	
	35.0	0.3	0.3	0.3	0.30	0.00	0.26	1.64		1.073		0.265	
	40.0	0.2	0.1	0.1	0.13	0.06	0.11	1.87		2.244		0.555	
45.2	12.0	1.2	1.2	1.2	1.20	0.00	1.00	0.56	0.56	0.649	0.0000	0.161	0.000
	14.0	1.4	1.4	1.5	1.43	0.06	1.19	0.65	0.65	0.467	0.0448	0.116	0.011
	15.0	1.6	1.9	1.8	1.77	0.15	1.47	0.70	0.69	0.321	0.1034	0.079	0.026
	16.0	2.3	2.5	2.2	2.33	0.15	1.94	0.75	0.74	0.177	0.0749	0.044	0.019
	17.0	2.8	2.8	2.8	2.80	0.00	2.33	0.79	0.79	0.137	0.0438	0.034	0.011
	18.0	3.0	3.2	3.2	3.13	0.12	2.61	0.84	0.83	0.147	0.0640	0.036	0.016
	19.0	3.1	3.7	3.7	3.50	0.35	2.92	0.89	0.88	0.152	0.0137	0.038	0.003
	20.0	2.9	3.0	3.1	3.00	0.10	2.50	0.93	0.93	0.203	-0.0013	0.050	0.000
	21.0	2.6	2.7	2.4	2.57	0.15	2.14	0.98	0.97	0.237	0.0601	0.059	0.015
	22.0	2.7	2.5	2.6	2.60	0.10	2.17	1.03	1.02	0.223	0.0291	0.055	0.007
	23.0	1.7	1.7	1.8	1.73	0.06	1.44	1.07	1.06	0.314	0.0614	0.078	0.015
	24.0	1.2	1.2	1.2	1.20	0.00	1.00	1.12	1.11	0.431	0.0250	0.107	0.006
	26.0	1.0	1.0	0.9	0.97	0.06	0.81	1.21	1.20	0.472	0.0154	0.117	0.004
	28.0	0.7	0.7	0.7	0.70	0.00	0.58	1.31	1.30	0.596	0.0523	0.147	0.013
	30.0	0.5	0.5	0.5	0.50	0.00	0.42	1.40	1.39	0.784	0.0836	0.194	0.021
	35.0	0.3	0.3	0.3	0.30	0.00	0.25	1.64	1.62	1.110	0.0375	0.275	0.009
	40.0	0.1	0.1	0.1	0.10	0.00	0.08	1.87	1.85	3.140	0.8964	0.777	0.222
73.9	12.0	1.3	1.2	1.2	1.23	0.06	1.00	0.56	0.34	0.649	0.0000	0.161	0.000
	14.0	1.5	1.4	1.4	1.43	0.06	1.16	0.65	0.40	0.491	0.0688	0.122	0.017
	15.0	1.7	1.9	1.8	1.80	0.10	1.46	0.70	0.43	0.327	0.1097	0.081	0.027
	16.0	2.2	2.2	2.2	2.20	0.00	1.78	0.75	0.45	0.231	0.1294	0.057	0.032
	17.0	2.7	2.7	2.6	2.67	0.06	2.16	0.79	0.48	0.176	0.0820	0.043	0.020
	18.0	3.0	3.0	2.9	2.97	0.06	2.41	0.84	0.51	0.176	0.0927	0.043	0.023
	19.0	3.1	3.2	3.2	3.17	0.06	2.57	0.89	0.54	0.184	0.0459	0.046	0.011
	20.0	2.9	3.2	3.2	3.10	0.17	2.51	0.93	0.57	0.202	-0.0025	0.050	-0.001
	21.0	2.2	2.3	2.3	2.27	0.06	1.84	0.98	0.60	0.277	0.0993	0.068	0.025
	22.0	2.5	2.5	2.3	2.43	0.12	1.97	1.03	0.62	0.245	0.0513	0.061	0.013
	23.0	1.5	1.6	1.7	1.60	0.10	1.30	1.07	0.65	0.351	0.0988	0.087	0.024
	24.0	1.3	1.3	1.3	1.30	0.00	1.05	1.12	0.68	0.407	0.0013	0.101	0.000
	26.0	1.0	1.0	1.0	1.00	0.00	0.81	1.21	0.74	0.468	0.0118	0.116	0.003
	28.0	0.8	0.8	0.7	0.77	0.06	0.62	1.31	0.79	0.551	0.0076	0.136	0.002
	30.0	0.5	0.5	0.5	0.50	0.00	0.41	1.40	0.85	0.810	0.1095	0.200	0.027
	35.0	0.3	0.3	0.3	0.30	0.00	0.24	1.64	0.99	1.148	0.0748	0.284	0.019
	40.0	0.1	0.1	0.1	0.10	0.00	0.08	1.87	1.13	3.231	0.9875	0.799	0.244
94.2	12.0	1.3	1.1	1.1	1.17	0.12	1.00	0.56	0.27	0.649	0.0000	0.161	0.000
	14.0	1.5	1.3	1.3	1.37	0.12	1.17	0.65	0.31	0.484	0.0618	0.120	0.015
	15.0	1.7	1.5	1.7	1.63	0.12	1.40	0.70	0.33	0.358	0.1400	0.088	0.035
	16.0	1.9	2.0	1.9	1.93	0.06	1.66	0.75	0.36	0.275	0.1734	0.068	0.043
	17.0	2.5	2.4	2.4	2.43	0.06	2.09	0.79	0.38	0.193	0.0992	0.048	0.025
	18.0	2.9	2.8	2.7	2.80	0.10	2.40	0.84	0.40	0.176	0.0935	0.044	0.023
	19.0	3.0	3.0	3.0	3.00	0.00	2.57	0.89	0.42	0.184	0.0455	0.045	0.011
	20.0	2.9	3.0	3.1	3.00	0.10	2.57	0.93	0.44	0.197	-0.0076	0.049	-0.002
	21.0	2.2	2.4	2.4	2.33	0.12	2.00	0.98	0.47	0.254	0.0767	0.063	0.019
	22.0	2.5	2.2	2.2	2.30	0.17	1.97	1.03	0.49	0.245	0.0515	0.061	0.013
	23.0	1.6	1.7	1.8	1.70	0.10	1.46	1.07	0.51	0.311	0.0585	0.077	0.014
	24.0	1.4	1.3	1.5	1.40	0.10	1.20	1.12	0.53	0.353	-0.0525	0.087	-0.013
	26.0	1.0	1.0	1.0	1.00	0.00	0.86	1.21	0.58	0.438	-0.0181	0.108	-0.004
	28.0	0.7	0.8	0.8	0.77	0.06	0.66	1.31	0.62	0.514	-0.0297	0.127	-0.007
	30.0	0.5	0.5	0.5	0.50	0.00	0.43	1.40	0.67	0.758	0.0575	0.187	0.014
	35.0	0.3	0.3	0.3	0.30	0.00	0.26	1.64	0.78	1.073	0.0000	0.265	0.000
	40.0	0.1	0.1	0.1	0.10	0.00	0.09	1.87	0.89	3.049	0.8052	0.754	0.199
110.8	12.0	1.1	1.1	1.0	1.07	0.06	1.00	0.56	0.23	0.649	0.0000	0.161	0.000
	14.0	1.4	1.2	1.1	1.23	0.15	1.16	0.65	0.26	0.496	0.0733	0.123	0.018
	15.0	1.4	1.4	1.5	1.43	0.06	1.34	0.70	0.28	0.387	0.1698	0.096	0.042
	16.0	1.7	1.7	1.8	1.73	0.06	1.63	0.75	0.30	0.287	0.1850	0.071	0.046
	17.0	2.2	2.2	2.1	2.17	0.06	2.03	0.79	0.32	0.205	0.1117	0.051	0.028
	18.0	2.7	2.5	2.3	2.50	0.20	2.34	0.84	0.34	0.185	0.1017	0.046	0.025
	19.0	2.9	2.8	2.6	2.77	0.15	2.59	0.89	0.36	0.181	0.0433	0.045	0.011
	20.0	2.8	2.9	2.8	2.83	0.06	2.66	0.93	0.38	0.190	-0.0146	0.047	-0.004
	21.0	2.5	2.7	2.5	2.57	0.12	2.41	0.98	0.40	0.211	0.0336	0.052	0.008
	22.0	2.7	2.4	2.3	2.47	0.21	2.31	1.03	0.42	0.208	0.0148	0.052	0.004
	23.0	1.9	2.0	1.9	1.93	0.06	1.81	1.07	0.43	0.246	-0.0062	0.061	-0.002
	24.0	1.4	1.7	1.7	1.60	0.17	1.50	1.12	0.45	0.274	-0.1317	0.068	-0.033
	26.0	1.1	1.0	1.0	1.03	0.06	0.97	1.21	0.49	0.377	-0.0795	0.093	-0.020
	28.0	0.9	0.8	0.8	0.83	0.06	0.78	1.31	0.53	0.407	-0.1372	0.101	-0.034
	30.0	0.7	0.5	0.5	0.57	0.12	0.53	1.40	0.57	0.576	-0.1238	0.143	-0.031
	35.0	0.3	0.3	0.3	0.30	0.00	0.28	1.64	0.66	0.959	-0.1141	0.237	-0.028
	40.0	0.1	0.1	0.1	0.10	0.00	0.09	1.87	0.76	2.774	0.5307	0.686	0.131

Table A. 18 - Aerodynamic Damping – Spring 3, CV=±50V

Airspeed	Freq	Spring 3, CV=±50V, (CR=1.353) (12/27/11)											
		P2P Deflection					Normalized Deflection	Frequency Ratio	Reduced Frequency	Total Damping Ratio	Aerodynamic Damping Ratio	Structural Damping Coefficient	Aerodynamic Damping Coefficient
		Run 1	Run 2	Run 3	Avg	St. Dev.	Avg	r		ζ_{tot}	ζ_{air}	c_{vane}	c_{aero} (C_{MQ})
ft/sec	Hz	deg	deg	deg	deg	deg	--	--	--	--	--	(ft lb$_f$)/(rad/s)	(ft lb$_f$)/(rad/s)
0.0	8.0	1.1	1.0	1.0	1.03	0.06	1.00	0.43		0.674		0.146	
	10.0	1.2	1.3	1.2	1.23	0.06	1.19	0.53		0.410		0.089	
	12.0	1.4	1.6	1.5	1.50	0.10	1.45	0.64		0.279		0.060	
	14.0	2.0	2.3	2.2	2.17	0.15	2.10	0.75		0.124		0.027	
	15.0	2.6	2.8	2.7	2.70	0.10	2.61	0.80		0.087		0.019	
	16.0	2.9	3.1	3.1	3.03	0.12	2.94	0.86		0.123		0.027	
	17.0	3.4	3.8	3.8	3.67	0.23	3.55	0.91		0.122		0.026	
	18.0	3.7	4.1	4.2	4.00	0.26	3.87	0.96		0.129		0.028	
	19.0	3.2	3.3	3.3	3.27	0.06	3.16	1.02		0.155		0.033	
	20.0	2.5	2.7	2.9	2.70	0.20	2.61	1.07		0.166		0.036	
	21.0	1.2	1.3	1.3	1.27	0.06	1.23	1.12		0.344		0.074	
	22.0	2.0	2.2	2.1	2.10	0.10	2.03	1.18		0.131		0.028	
	23.0	1.3	1.5	1.5	1.43	0.12	1.39	1.23		0.206		0.045	
	24.0	1.0	1.2	1.1	1.10	0.10	1.06	1.28		0.265		0.057	
	26.0	0.8	0.9	0.9	0.87	0.06	0.84	1.39		0.267		0.058	
	28.0	0.7	0.7	0.7	0.70	0.00	0.68	1.50		0.266		0.058	
	30.0	0.5	0.5	0.5	0.50	0.00	0.48	1.60		0.418		0.090	
	35.0	0.3	0.3	0.3	0.30	0.00	0.29	1.87		0.632		0.137	
	40.0	0.2	0.1	0.1	0.13	0.06	0.13	2.14		1.607		0.347	
45.2	8.0	1.1	1.2	1.0	1.10	0.10	1.00	0.43	0.37	0.674	0.0000	0.146	0.000
	10.0	1.3	1.4	1.3	1.33	0.06	1.21	0.53	0.46	0.386	-0.0234	0.084	-0.005
	12.0	1.5	1.6	1.6	1.57	0.06	1.42	0.64	0.56	0.299	0.0193	0.065	0.004
	14.0	2.0	2.2	2.2	2.13	0.12	1.94	0.75	0.65	0.180	0.0564	0.039	0.012
	15.0	2.5	2.8	2.6	2.63	0.15	2.39	0.80	0.69	0.136	0.0490	0.029	0.011
	16.0	2.9	3.0	3.0	2.97	0.06	2.70	0.86	0.74	0.150	0.0268	0.032	0.006
	17.0	3.3	3.4	3.4	3.37	0.06	3.06	0.91	0.79	0.152	0.0301	0.033	0.007
	18.0	3.6	3.8	3.7	3.70	0.10	3.36	0.96	0.83	0.150	0.0210	0.032	0.005
	19.0	3.0	3.2	3.3	3.17	0.15	2.88	1.02	0.88	0.170	0.0153	0.037	0.003
	20.0	2.2	2.6	2.5	2.43	0.21	2.21	1.07	0.93	0.200	0.0346	0.043	0.007
	21.0	1.3	1.3	1.4	1.33	0.06	1.21	1.12	0.97	0.348	0.0043	0.075	0.001
	22.0	2.0	2.0	2.0	2.00	0.00	1.82	1.18	1.02	0.167	0.0366	0.036	0.008
	23.0	1.3	1.4	1.4	1.37	0.06	1.24	1.23	1.06	0.252	0.0462	0.055	0.010
	24.0	1.1	1.1	1.2	1.13	0.06	1.03	1.28	1.11	0.282	0.0165	0.061	0.004
	26.0	0.9	0.9	0.9	0.90	0.00	0.82	1.39	1.20	0.284	0.0170	0.061	0.004
	28.0	0.7	0.7	0.6	0.67	0.06	0.61	1.50	1.30	0.363	0.0963	0.078	0.021
	30.0	0.5	0.5	0.5	0.50	0.00	0.45	1.60	1.39	0.479	0.0616	0.104	0.013
	35.0	0.3	0.3	0.3	0.30	0.00	0.27	1.87	1.62	0.716	0.0837	0.155	0.018
	40.0	0.2	0.1	0.1	0.13	0.06	0.12	2.14	1.85	1.738	0.1307	0.376	0.028
73.9	8.0	1.0	1.0	1.0	1.00	0.00	1.00	0.43	0.23	0.674	0.0000	0.146	0.000
	10.0	1.2	1.2	1.1	1.17	0.06	1.17	0.53	0.28	0.443	0.0335	0.096	0.007
	12.0	1.5	1.4	1.4	1.43	0.06	1.43	0.64	0.34	0.292	0.0129	0.063	0.003
	14.0	1.9	1.8	1.8	1.83	0.06	1.83	0.75	0.40	0.216	0.0921	0.047	0.020
	15.0	2.3	2.3	2.3	2.30	0.00	2.30	0.80	0.43	0.155	0.0684	0.034	0.015
	16.0	2.8	2.9	2.8	2.83	0.06	2.83	0.86	0.45	0.134	0.0113	0.029	0.002
	17.0	3.0	3.1	3.1	3.07	0.06	3.07	0.91	0.48	0.152	0.0297	0.033	0.006
	18.0	3.2	3.5	3.3	3.33	0.15	3.33	0.96	0.51	0.151	0.0224	0.033	0.005
	19.0	3.1	3.4	3.3	3.27	0.15	3.27	1.02	0.54	0.150	-0.0050	0.032	-0.001
	20.0	2.2	2.4	2.5	2.37	0.15	2.37	1.07	0.57	0.186	0.0199	0.040	0.004
	21.0	1.6	1.6	1.6	1.60	0.00	1.60	1.12	0.60	0.253	-0.0913	0.055	-0.020
	22.0	1.9	2.0	2.0	1.97	0.06	1.97	1.18	0.62	0.142	0.0109	0.031	0.002
	23.0	1.5	1.5	1.5	1.50	0.00	1.50	1.23	0.65	0.173	-0.0328	0.037	-0.007
	24.0	1.3	1.2	1.3	1.27	0.06	1.27	1.28	0.68	0.176	-0.0891	0.038	-0.019
	26.0	0.9	0.9	0.9	0.90	0.00	0.90	1.39	0.74	0.217	-0.0500	0.047	-0.011
	28.0	0.7	0.7	0.7	0.70	0.00	0.70	1.50	0.79	0.236	-0.0307	0.051	-0.007
	30.0	0.5	0.5	0.5	0.50	0.00	0.50	1.60	0.85	0.385	-0.0328	0.083	-0.007
	35.0	0.3	0.3	0.3	0.30	0.00	0.30	1.87	0.99	0.588	-0.0440	0.127	-0.010
	40.0	0.1	0.1	0.1	0.10	0.00	0.10	2.14	1.13	2.183	0.5757	0.472	0.124
94.2	8.0	0.9	0.9	0.9	0.90	0.00	1.00	0.43	0.18	0.674	0.0000	0.146	0.000
	10.0	1.0	1.0	1.0	1.00	0.00	1.11	0.53	0.22	0.512	0.1024	0.111	0.022
	12.0	1.2	1.2	1.2	1.20	0.00	1.33	0.64	0.27	0.363	0.0832	0.078	0.018
	14.0	1.6	1.6	1.5	1.57	0.06	1.74	0.75	0.31	0.247	0.1234	0.053	0.027
	15.0	1.8	2.0	1.9	1.90	0.10	2.11	0.80	0.33	0.194	0.1077	0.042	0.023
	16.0	2.3	2.5	2.5	2.43	0.12	2.70	0.86	0.36	0.149	0.0261	0.032	0.006
	17.0	2.8	3.0	2.9	2.90	0.10	3.22	0.91	0.38	0.142	0.0194	0.031	0.004
	18.0	3.1	3.3	3.2	3.20	0.10	3.56	0.96	0.40	0.141	0.0124	0.030	0.003
	19.0	3.0	3.2	3.1	3.10	0.10	3.44	1.02	0.42	0.142	-0.0129	0.031	-0.003
	20.0	2.5	2.7	2.6	2.60	0.10	2.89	1.07	0.44	0.147	-0.0186	0.032	-0.004
	21.0	2.0	2.1	2.1	2.07	0.06	2.30	1.12	0.47	0.155	-0.1889	0.034	-0.041
	22.0	2.5	2.3	2.3	2.37	0.12	2.63	1.18	0.49	0.023	-0.1078	0.005	-0.023
	23.0	1.6	1.6	1.8	1.67	0.12	1.85	1.23	0.51	0.069	-0.1372	0.015	-0.030
	24.0	1.3	1.3	1.3	1.30	0.00	1.44	1.28	0.53	0.096	-0.1695	0.021	-0.037
	26.0	0.9	1.0	1.0	0.97	0.06	1.07	1.39	0.58	0.023	-0.2444	0.005	-0.053
	28.0	0.7	0.8	0.8	0.77	0.06	0.85	1.50	0.62	0.135	-0.1310	0.029	-0.028
	30.0	0.5	0.5	0.5	0.50	0.00	0.56	1.60	0.67	0.272	-0.1452	0.059	-0.031
	35.0	0.3	0.3	0.3	0.30	0.00	0.33	1.87	0.78	0.442	-0.1903	0.096	-0.041
	40.0	0.1	0.1	0.1	0.10	0.00	0.11	2.14	0.89	1.931	0.3234	0.417	0.070
110.8	8.0	0.9	0.9	0.9	0.90	0.00	1.00	0.43	0.15	0.674	0.0000	0.146	0.000
	10.0	1.0	1.0	1.0	1.00	0.00	1.11	0.53	0.19	0.512	0.1024	0.111	0.022
	12.0	1.1	1.1	1.1	1.10	0.00	1.22	0.64	0.23	0.443	0.1637	0.096	0.035
	14.0	1.3	1.2	1.2	1.23	0.06	1.37	0.75	0.26	0.389	0.2654	0.084	0.057
	15.0	1.5	1.4	1.4	1.43	0.06	1.59	0.80	0.28	0.322	0.2355	0.070	0.051
	16.0	1.7	1.9	1.8	1.80	0.10	2.00	0.86	0.30	0.247	0.1237	0.053	0.027
	17.0	2.3	2.4	2.3	2.33	0.06	2.59	0.91	0.32	0.189	0.0673	0.041	0.015
	18.0	2.8	2.9	2.8	2.83	0.06	3.15	0.96	0.34	0.161	0.0319	0.035	0.007
	19.0	3.0	3.1	3.0	3.03	0.06	3.37	1.02	0.36	0.145	-0.0097	0.031	-0.002
	20.0	2.7	2.8	2.6	2.70	0.10	3.00	1.07	0.38	0.141	-0.0252	0.030	-0.005
	21.0	2.6	2.5	2.5	2.53	0.06	2.81	1.12	0.40	0.107	-0.2369	0.023	-0.051
	22.0	2.3	2.5	2.4	2.40	0.10	2.67	1.18	0.42	0.035	-0.0954	0.008	-0.021
	23.0	1.7	1.7	1.7	1.70	0.00	1.89	1.23	0.43	0.054	-0.1525	0.012	-0.033
	24.0	1.3	1.5	1.5	1.43	0.12	1.59	1.28	0.45	0.061	-0.2042	0.013	-0.044
	26.0	1.1	1.0	1.0	1.03	0.06	1.15	1.39	0.49	0.120	-0.1465	0.026	-0.032
	28.0	0.9	0.8	0.8	0.83	0.06	0.93	1.50	0.53	0.205	-0.0616	0.044	-0.013
	30.0	0.6	0.5	0.5	0.53	0.06	0.59	1.60	0.57	0.190	-0.2277	0.041	-0.049
	35.0	0.4	0.3	0.3	0.33	0.06	0.37	1.87	0.66	0.270	-0.3617	0.058	-0.078
	40.0	0.2	0.2	0.1	0.17	0.06	0.19	2.14	0.76	0.946	-0.6613	0.205	-0.143

APPENDIX B
PLOTS

Table of Contents

B.1 Dynamic Response Diagrams

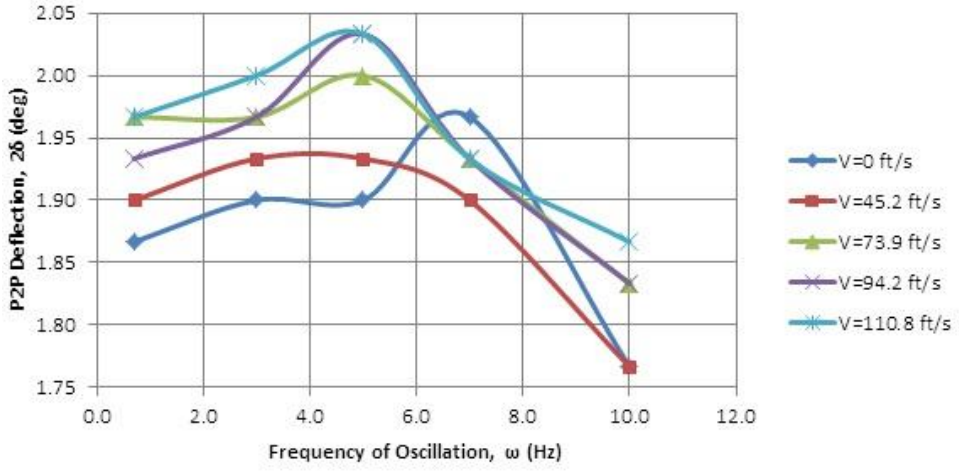

Figure B. 1 - Dynamic Response - No Spring, CV= ±180V

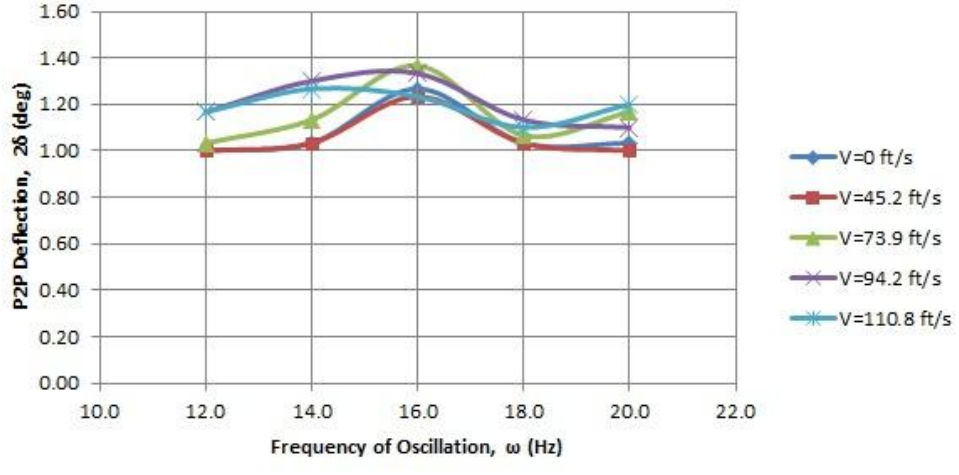

Figure B. 2 - Dynamic Response - No Spring, CV= ±100V

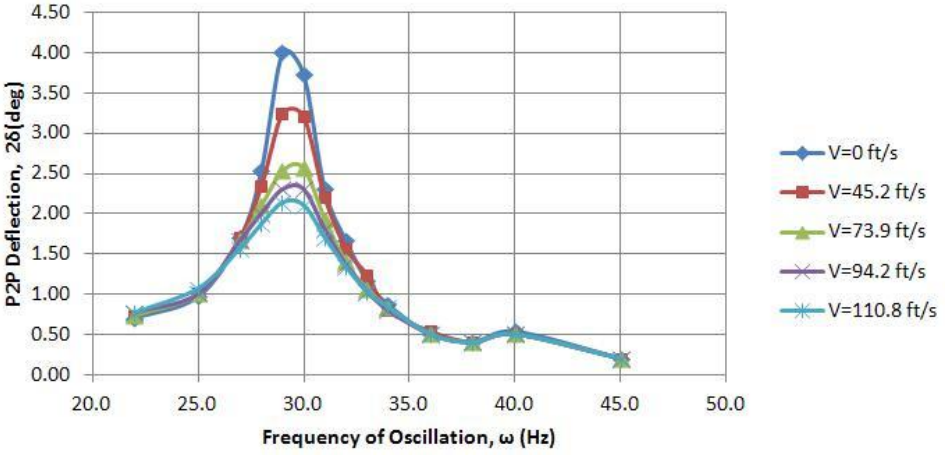

Figure B. 3 – Dynamic Response - No Spring, CV= ±50V

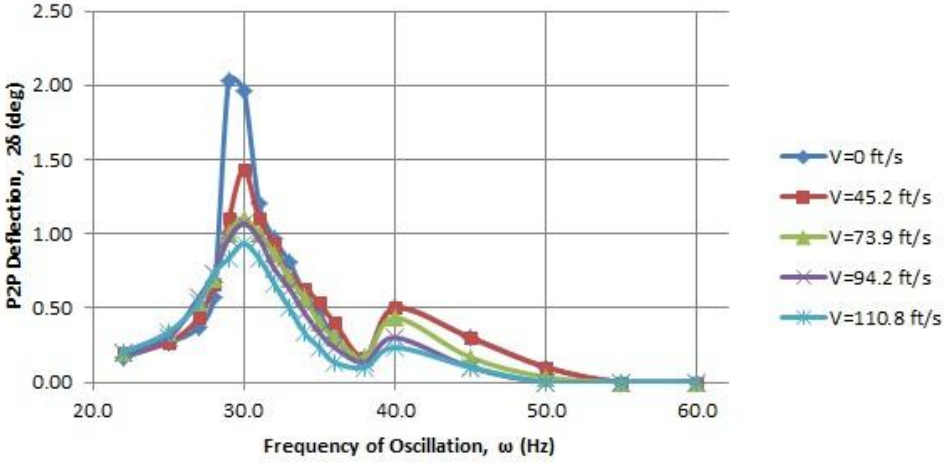

Figure B. 4 – Dynamic Response - No Spring, CV= ±20V

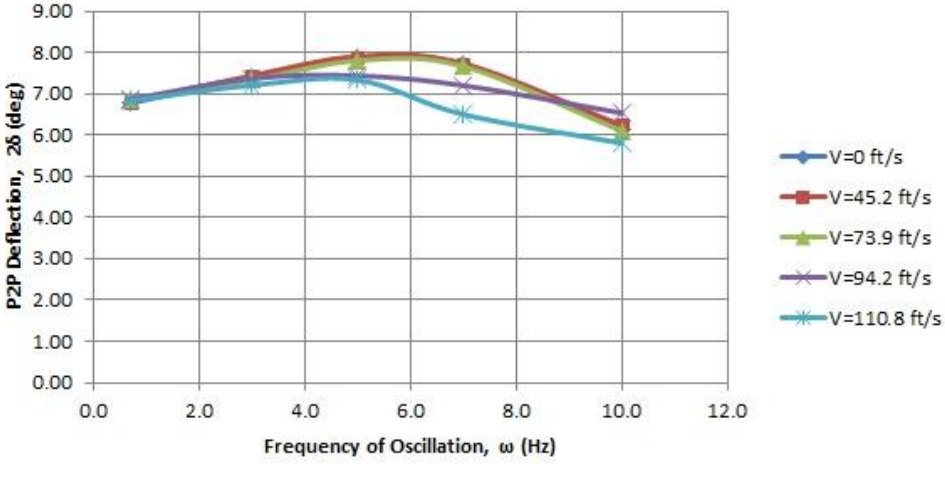

Figure B. 5 - Dynamic Response - Spring 1, CV= ±180V

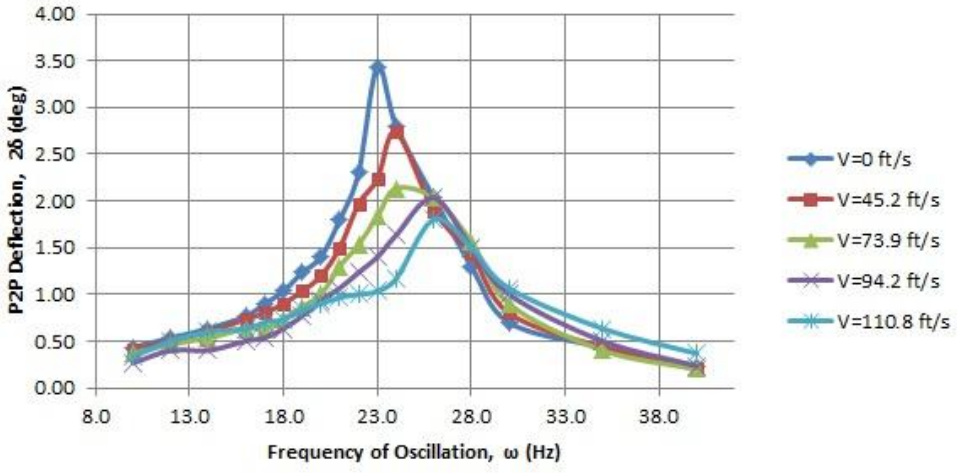

Figure B. 6 – Dynamic Response - Spring 1, CV= ±50V

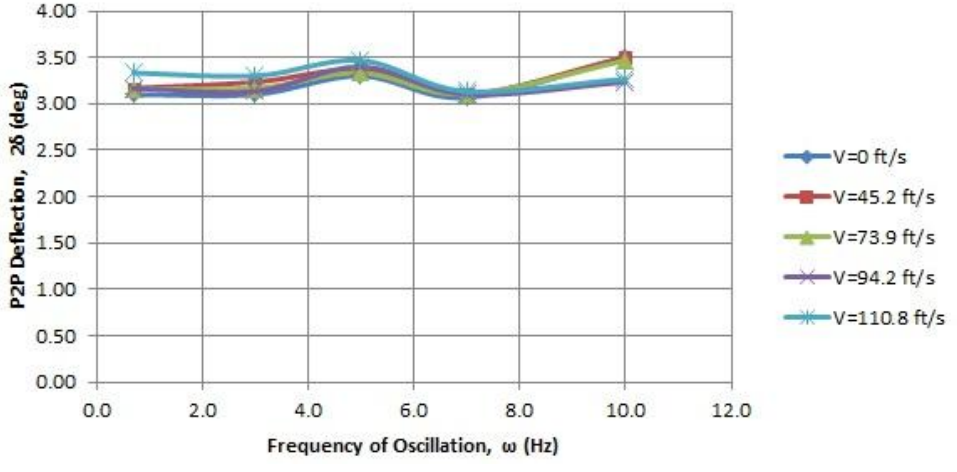

Figure B. 7 - Dynamic Response - Spring 2, CV= ±180V

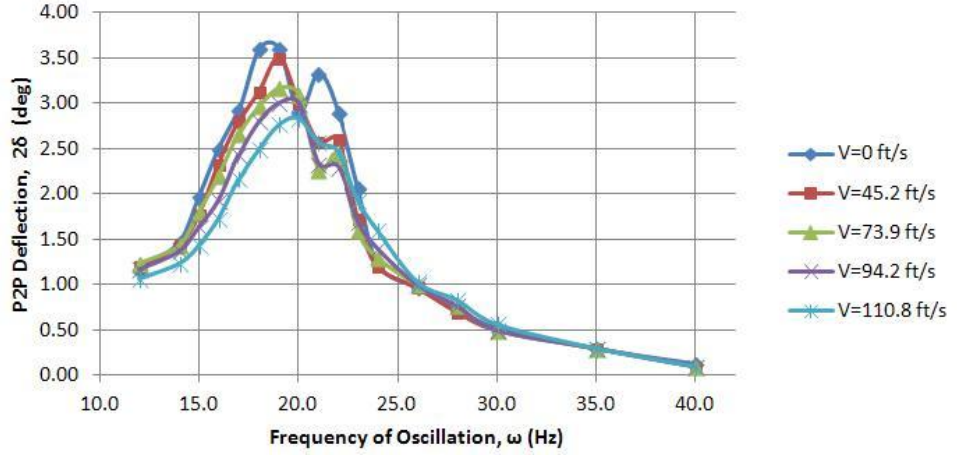

Figure B. 8 – Dynamic Response - Spring 2, CV= ±50V

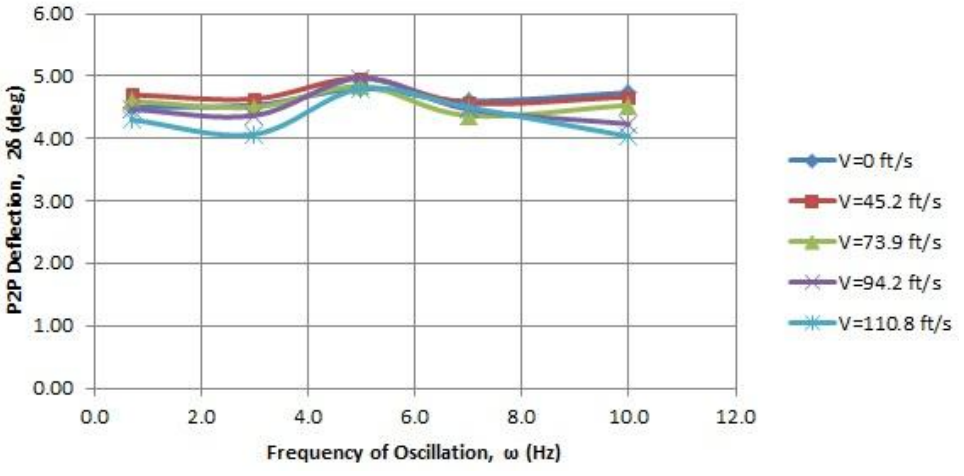

Figure B. 9 - Dynamic Response - Spring 3, CV= ±180V

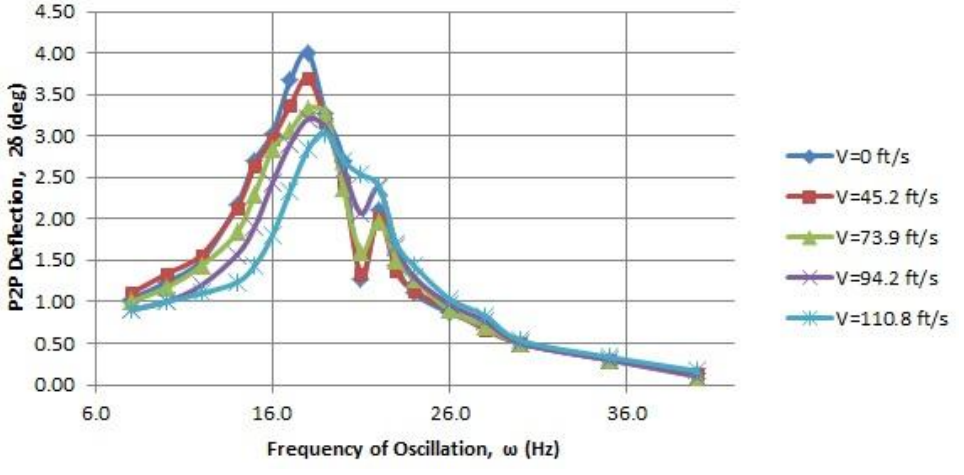

Figure B. 10 – Dynamic Response - Spring 3, CV= ±50V

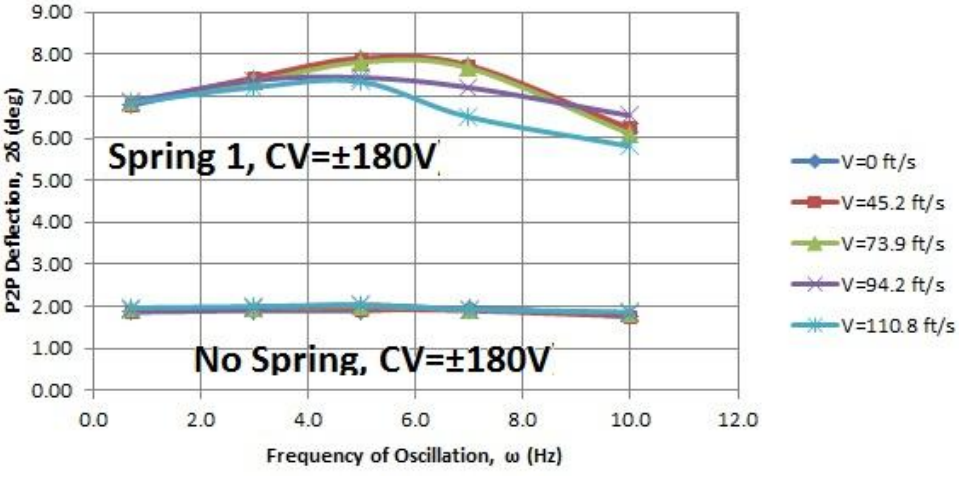

Figure B. 11 - Dynamic Response - Comparison A

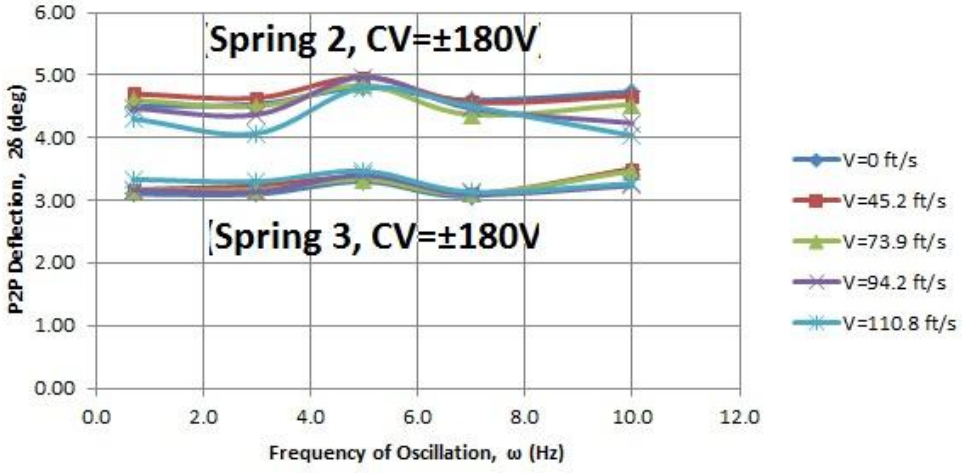

Figure B. 12 - Dynamic Response - Comparison B

B.2 Dynamic Loads

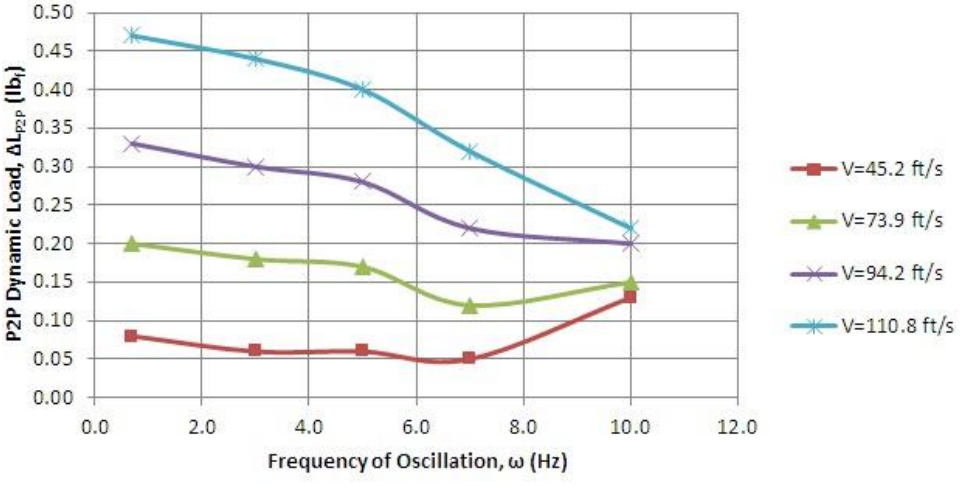

Figure B. 13 - Dynamic Loads - No Spring, CV = ±180V

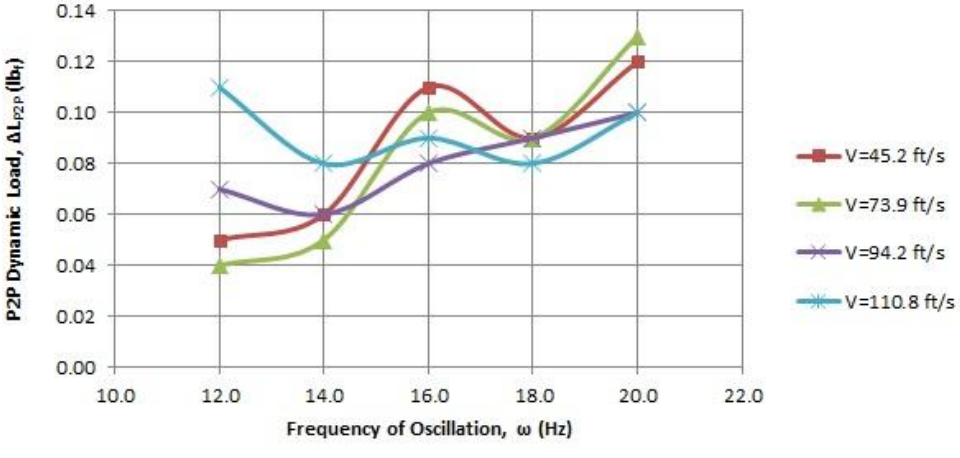

Figure B. 14 - Dynamic Loads - No Spring, CV = ±100V

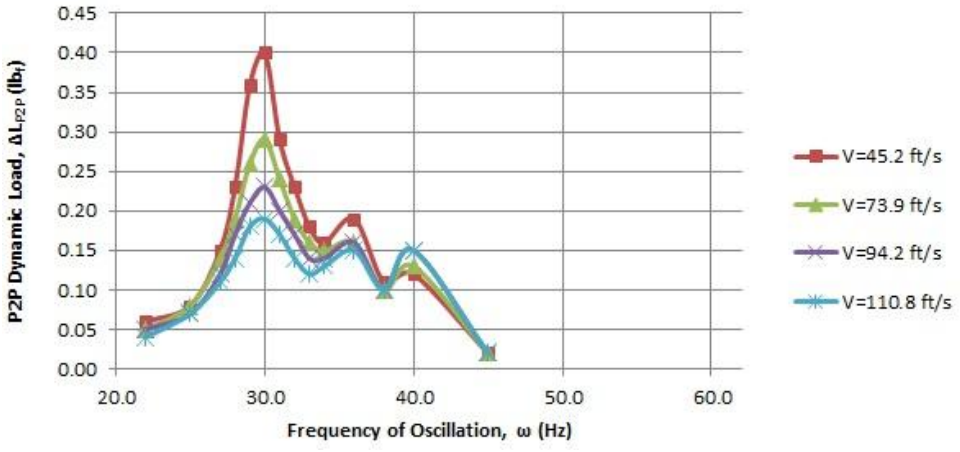

Figure B. 15 - Dynamic Loads - No Spring, CV = ±50V

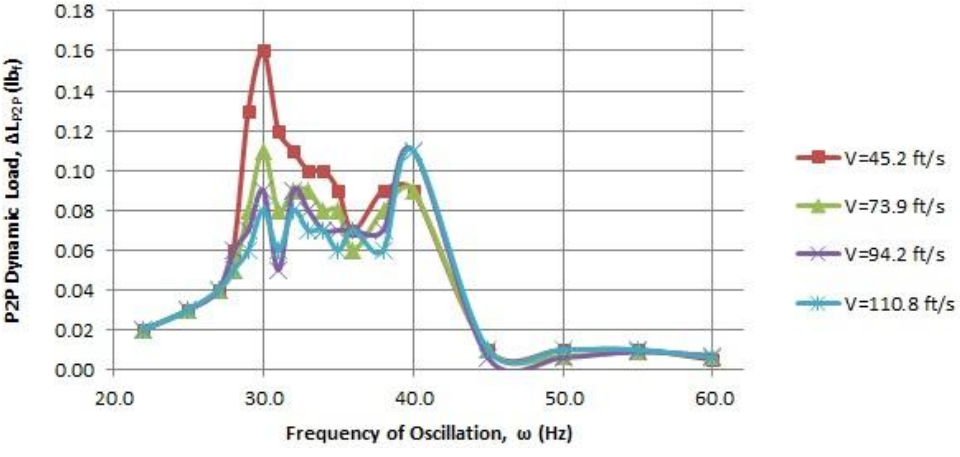

Figure B. 16 - Dynamic Loads - No Spring, CV = ±20V

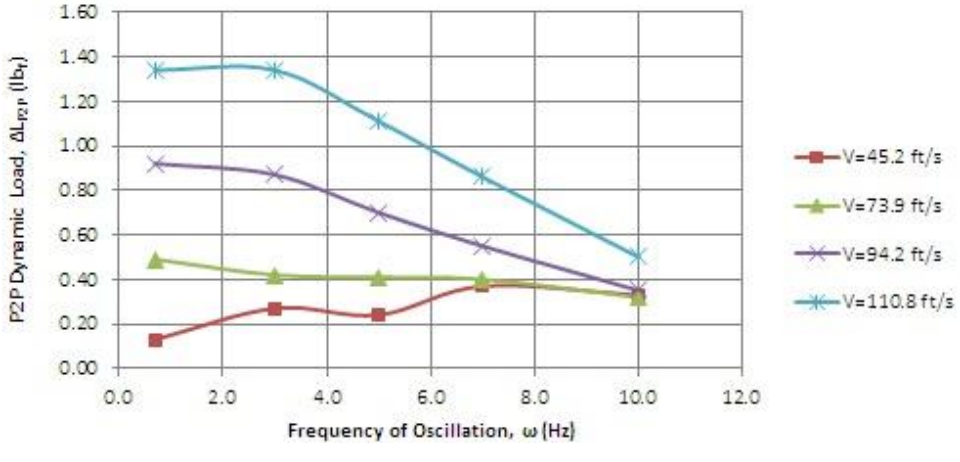

Figure B. 17 -Dynamic Loads - Spring 1, CV = ±180V

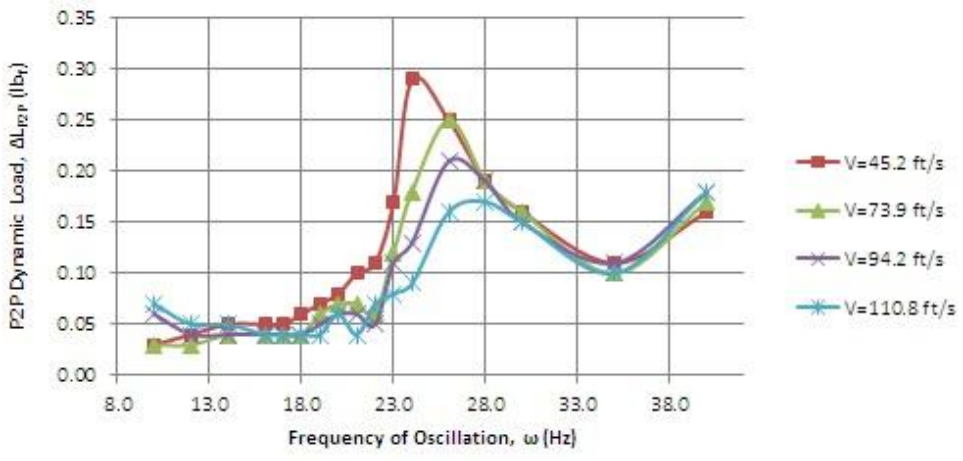

Figure B. 18 -Dynamic Loads - Spring 1, CV = ±50V

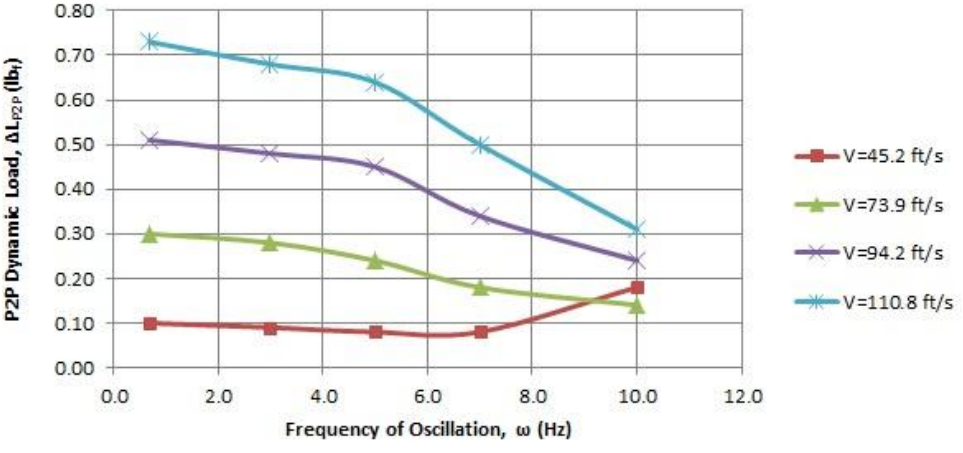

Figure B. 19 -Dynamic Loads - Spring 2, CV = ±180V

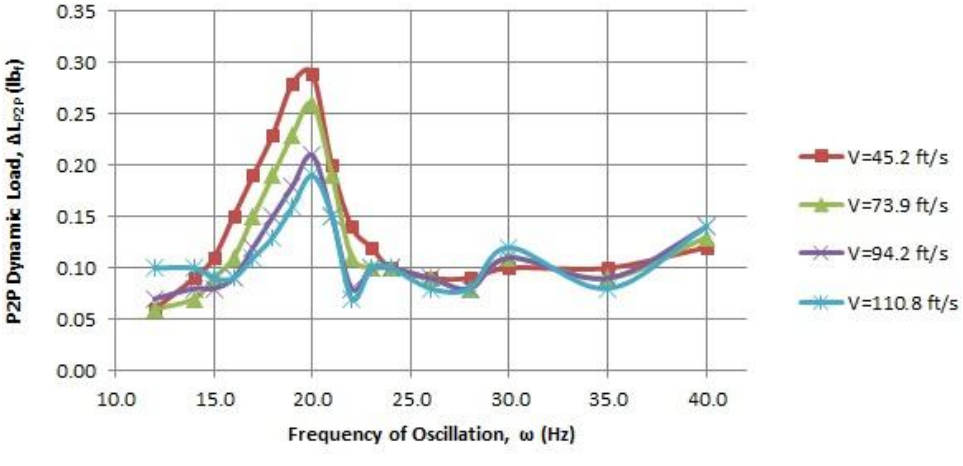

Figure B. 20 -Dynamic Loads - Spring 2, CV = ±50V

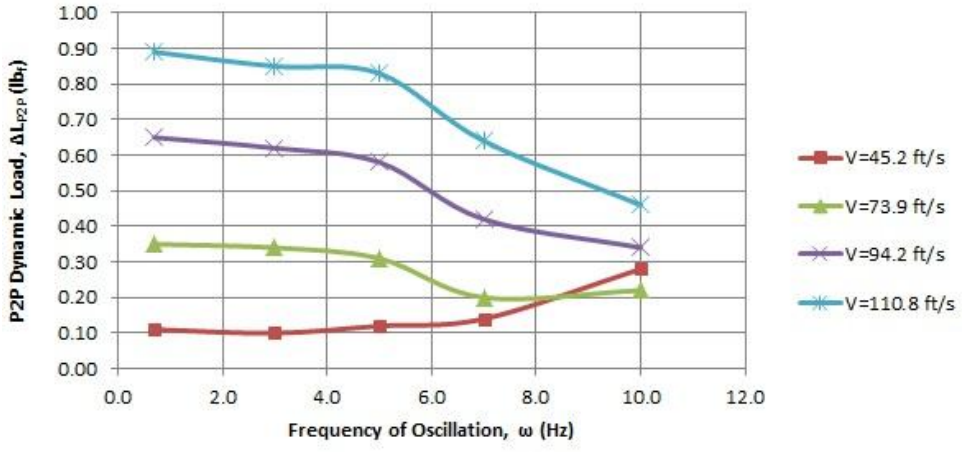

Figure B. 21 -Dynamic Loads - Spring 3, CV = ±180V

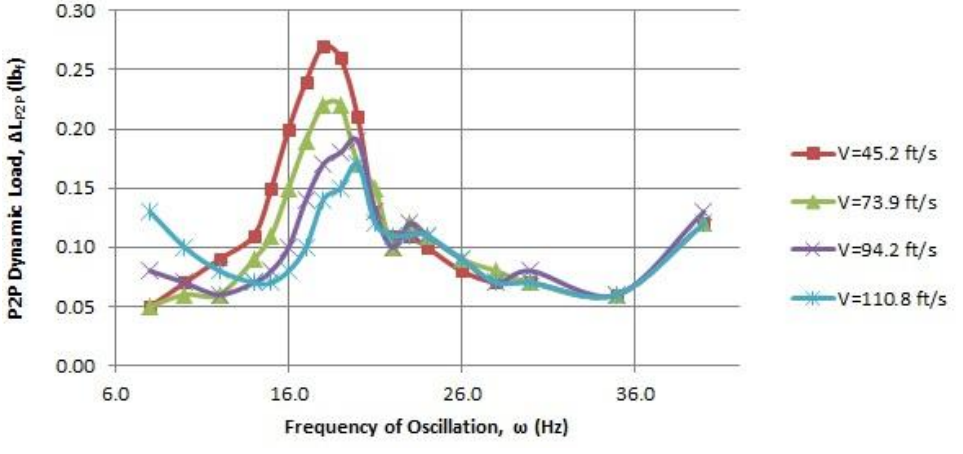

Figure B. 22 -Dynamic Loads - Spring 3, CV = ±50V

B.3 Dynamic Lift Coefficients

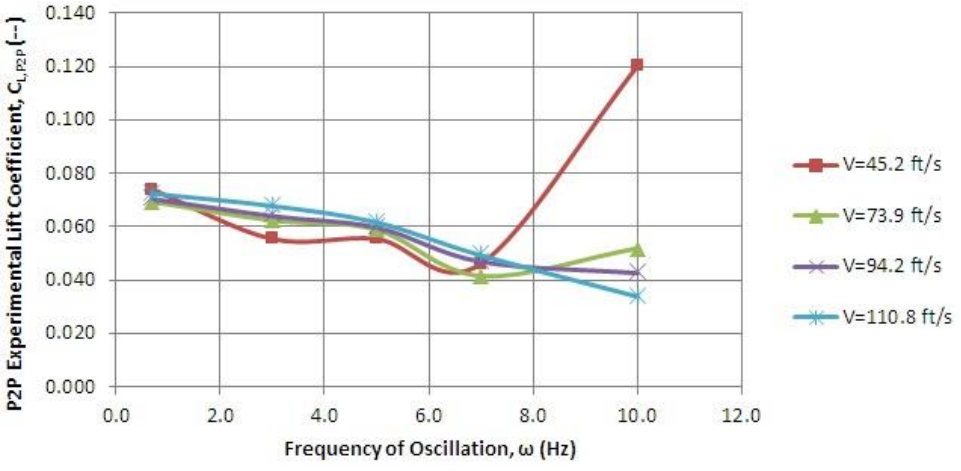

Figure B. 23 -Dynamic Lift Coefficients - No Spring, CV = ±180V

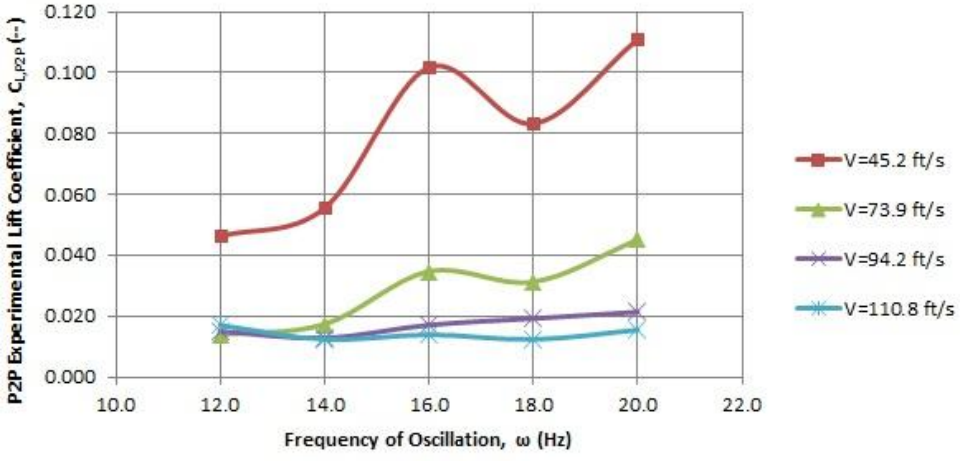

Figure B. 24 -Dynamic Lift Coefficients - No Spring, CV = ±100V

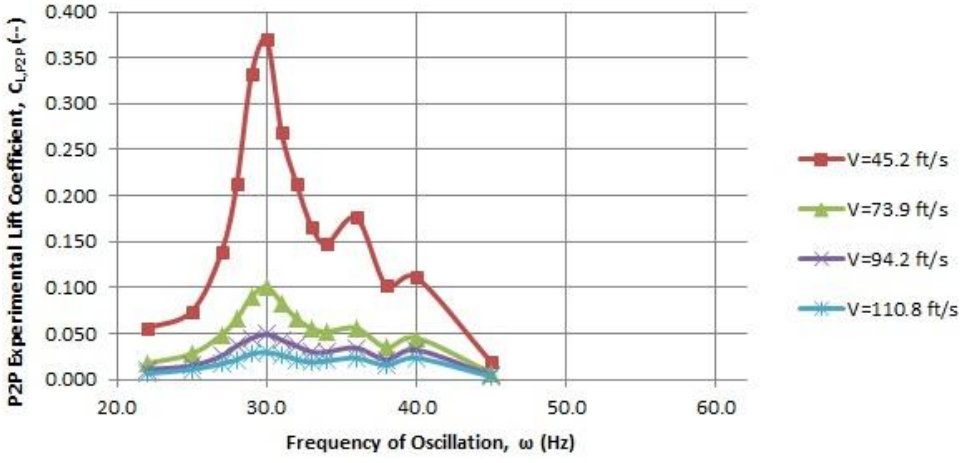

Figure B. 25 -Dynamic Lift Coefficients - No Spring, CV = ±50V

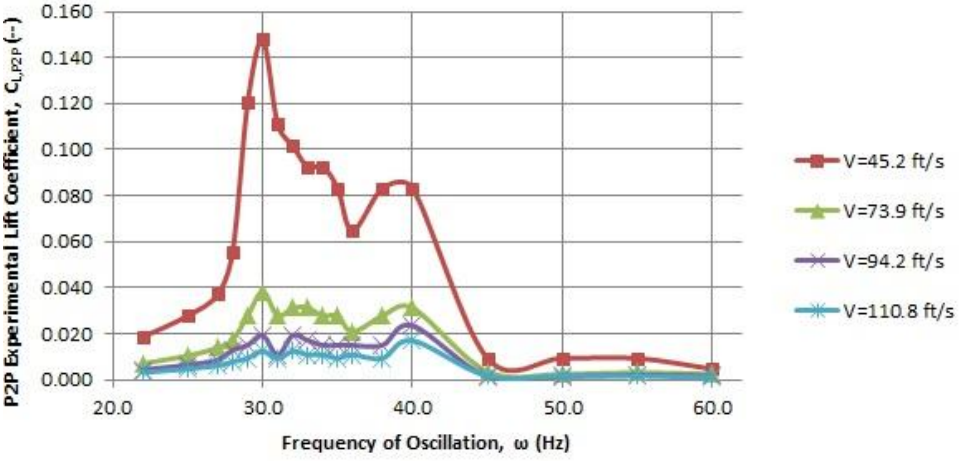

Figure B. 26 -Dynamic Lift Coefficients - No Spring, CV = ±20V

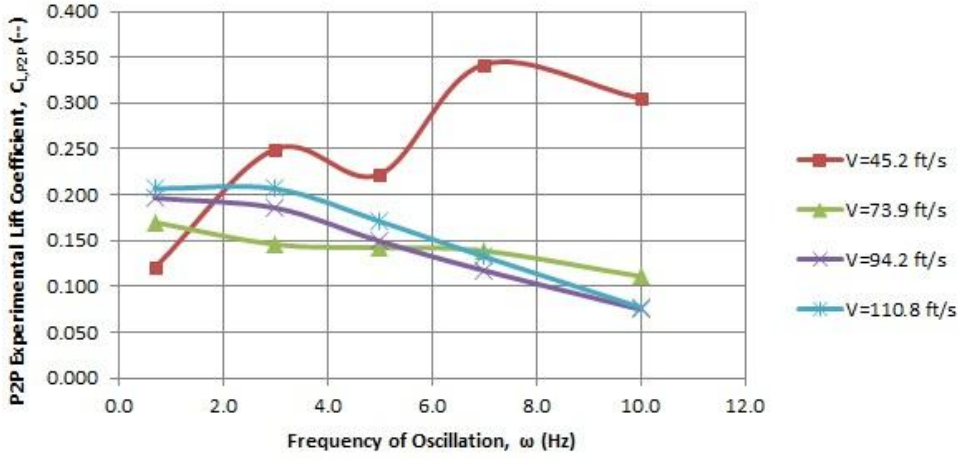

Figure B. 27 -Dynamic Lift Coefficients - Spring 1, CV = ±180V

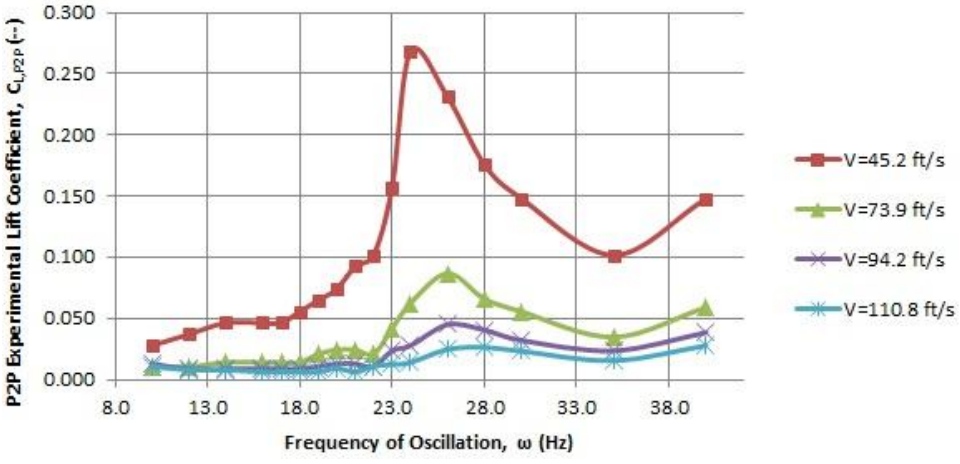

Figure B. 28 -Dynamic Lift Coefficients - Spring 1, CV = ±50V

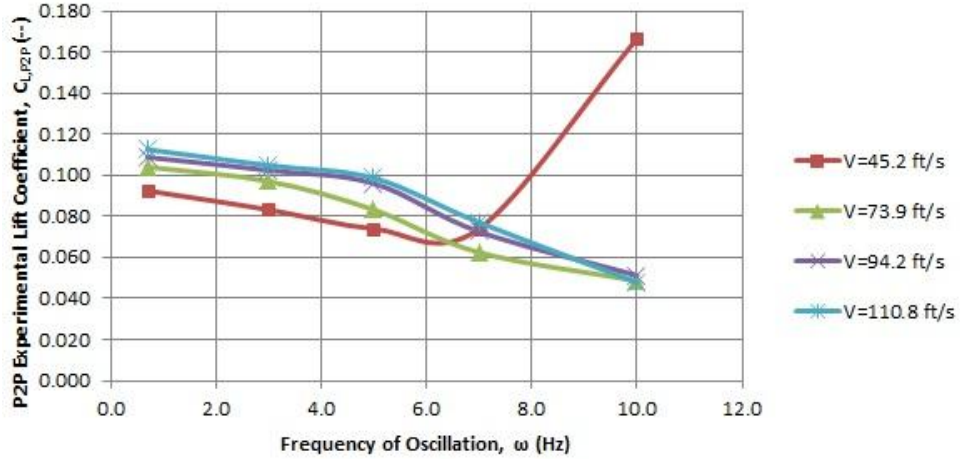

Figure B. 29 -Dynamic Lift Coefficients - Spring 2, CV = ±180V

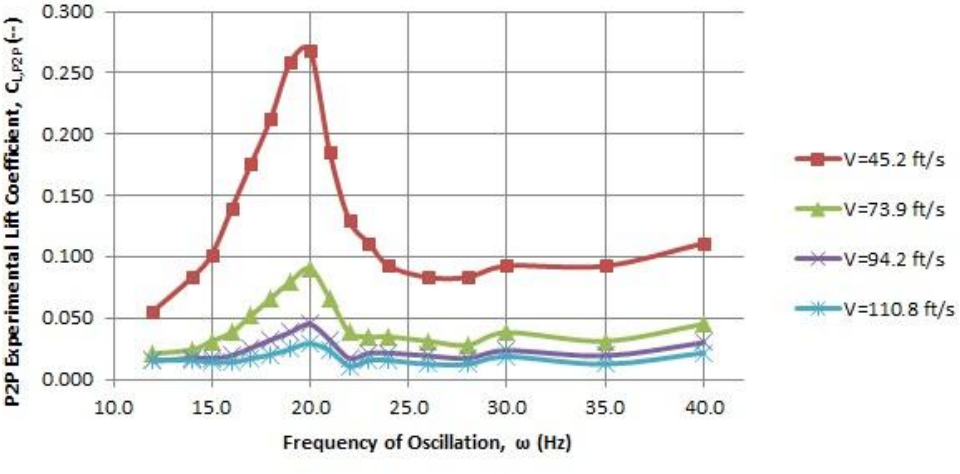

Figure B. 30 -Dynamic Lift Coefficients - Spring 2, CV = ±50V

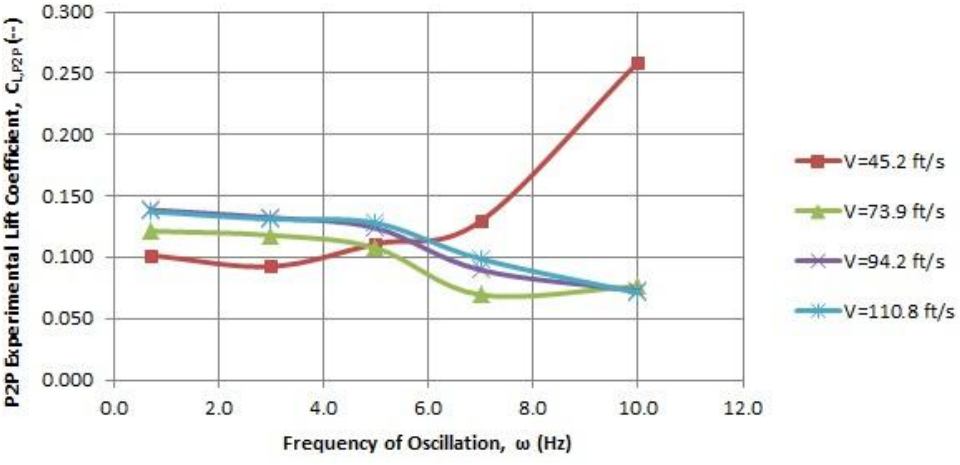

Figure B. 31 -Dynamic Lift Coefficients - Spring 3, CV = ±180V

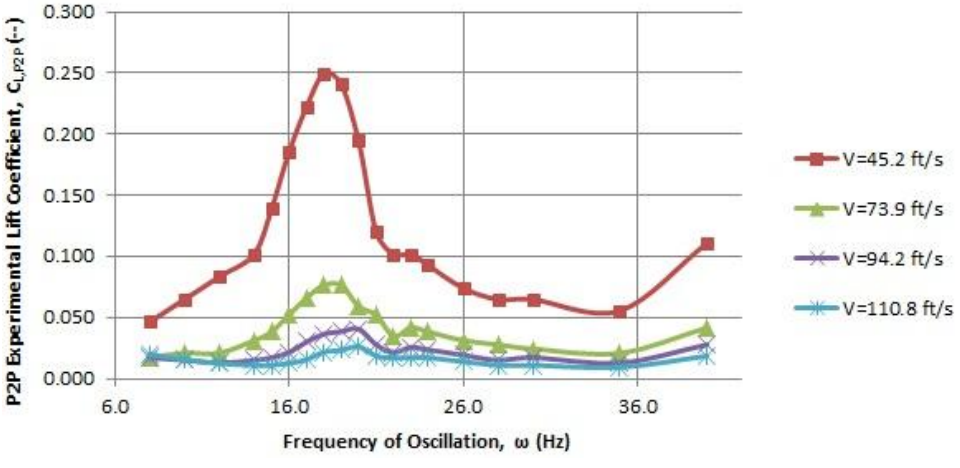

Figure B. 32 -Dynamic Lift Coefficients - Spring 3, CV = ±50V

APPENDIX C
MATLAB CODES

Table of Contents

C.1 Quasi-Static Force Isolation

```
%Ryan Barnhart - University of Kansas Graduate Research Assistant
%Fall 2011 - Adaptive Flutter Test Vane Wind Tunnel Testing
%Quasi-Static Delta Lift Calculations
%ω=0.1 Hz (Square Wave), Command Voltage: +- 180V

clear all
clc

%%%%%%%%%%%%%%%%%%Begin Analysis%%%%%%%%%%%%%%%%%%%

%Read .csv file into Matlab

data=csvread('Spring3.csv',2,0);                %Read File, Start Importing
                                                Data at Row 3, Column 1

t=data(:,1);                                    %Store Time Data

L=data(:,2);                                    %Store Load Data (N)

%Set Time Intervals, Calibration Factor

t_start=450;                                    %Beginning of data set
dt=50;                                          %Time Spent at this airspeed
t_end=t_start+dt;                               %End of data set

CF=0.191;                                       %Calibration Factor (lbf/N)

dt_2=10;                                        %Plotting Time Step

t1=t_start+dt_2;
t2=t1+10;                                       %Time Data for tplot
t3=t2+10;
t4=t3+10;

%Set Limits for Filter

dt_3=10;                                        %Time Step for Data Set
dt_4=20;                                        %Spacing Between Data Sets

a1=t_start+dt_3;
b1=a1+2;
c1=a1+5;
d1=c1+2;
a2=a1+dt_4;
b2=a2+2;
c2=a2+5;
d2=c2+2;
```

```
%Filter Data

x1=L(find(a1 <= t & t <= b1));

x2=L(find(c1 <= t & t <= d1));                    %Capture Load Data for time
                                                  interval specified
x3=L(find(a2 <= t & t <= b2));
x4=L(find(c2 <= t & t <= d2));

x5=L(find(t1 <= t & t <= t2));
x6=L(find(t3 <= t & t <= t4));

%Analyze Data

Avg1=mean(x1);
Avg2=mean(x2);                                    %Find Average Load (isolate
                                                 from peak values)
Avg3=mean(x3);
Avg4=mean(x4);

StDev1=std(x1);
StDev2=std(x2);                                   %Find standard deviation from
                                                 peak values
StDev3=std(x3);
StDev4=std(x4);

DeltaL1=abs(Avg1-Avg2);
DeltaL2=abs(Avg3-Avg4);

DeltaL=((DeltaL1+DeltaL2)/2)*CF                       %Determine Change in lift
                                                 (lbf)

StDev=(StDev1+StDev2+StDev3+StDev4)/4          %Determine Standard Deviation

%Plot Data

tplot1=t(find(t1 <= t & t <= t2));
tplot2=t(find(t3 <= t & t <= t4));

mplot1=Avg1*ones(1,length(tplot1));
mplot2=Avg2*ones(1,length(tplot1));
mplot3=Avg3*ones(1,length(tplot2));
mplot4=Avg4*ones(1,length(tplot2));

subplot(2,1,1), plot(tplot1,x5,tplot1,mplot1,tplot1,mplot2)
xlabel('Time, t (s)')
ylabel('Load, L (N)')
subplot(2,1,2), plot(tplot2,x6,tplot2,mplot3,tplot2,mplot4)
xlabel('Time, t (s)')
ylabel('Load, L (N)')
```

C.2 Dynamic Data Extraction

```
%Ryan Barnhart - University of Kansas Graduate Research Assistant
%Fall 2011 - Adaptive Flutter Test Vane Wind Tunnel Testing
%Dynamic Delta Lift Calculations
%ω=0.7-60 Hz (Sine Wave), Command Voltage: +- 20V to +- 180V

clear all
clc

%%%%%%%%%%%%%%%%%Begin Analysis%%%%%%%%%%%%%%%%%%

%Read .csv file into Matlab

data=csvread('NoSpring_10Hz.csv',2,0);            %Read File, Start Importing
Data at Row 3, Column 1

t=data(:,1);                                      %Store Time Data

L=data(:,2);                                      %Store Load Data (N)

%Set Time Intervals, Calibration Factor, Standard Deviation

fr=5;                                                %Set frequence of interest
(Hz)
cyc=10;                                           %Number of cycles to analyze
StDev=0.054;                                       %Standard Deviation Calculated
from Quasi-Static Testing
t_start=600;                                      %Beginning of data set (s)
dt=50;                                            %Time Spent at this airspeed
t_end=t_start+dt;                                 %End of data set

CF=0.195;                                         %Calibration Factor (lbf/N)

dt_2=10;                                          %Plotting Time Step

t1=t_start+dt_2;                                     %Allow data to "settle" into
rhythm
t2=t_start+(dt_2)*2;                                  %Select "random sample" for
analysis
t3=t2+(cyc/fr);                                   %Time Data for tplot
t4=t_start+(dt_2)*4;                                %Cut data short of transition
to next "stage"
```

```
%Set Limits for Filter

dt_3=.25*(1/fr);                                    %Time Step for Data Set

a=0;
b=0;
for n=0:dt_3:(cyc/fr)                                  %Capture Load Data for time
interval specified

    a=a+1;
    b=n+t2+dt_3;

    x1(a)=min(L(find(b <= t & t<= (b+(1/fr)))));
    x2(a)=max(L(find(b <= t & t<= (b+(1/fr)))));

end

x5=L(find(t2 <= t & t <= t3));
x6=L(find(t1 <= t & t <= t4));

%Analyze Data

Avg=mean(x5);
Avg2=mean(x1);                                      %Find Average Load (isolate
from peak values)
Avg3=mean(x2);


DeltaL=(abs(Avg2-Avg3))*CF                           %Determine Change in lift
(lbf)

%Plot Data

tplot1=t(find(t2 <= t & t <= t3));
tplot2=t(find(t1 <= t & t <= t4));

mplot=Avg*ones(1,length(tplot1));
mplot2=Avg2*ones(1,length(tplot1));
mplot3=Avg3*ones(1,length(tplot1));


subplot(2,1,1), plot(tplot1,x5,tplot1,mplot,tplot1,mplot2,tplot1,mplot3)
xlabel('Time, t (s)')
ylabel('Load, L (N)')
subplot(2,1,2), plot(tplot2,x6)
xlabel('Time, t (s)')
ylabel('Load, L (N)')
```